Multi-Component Transport in Next-Generation Batteries

by

Lucas D. Griffith

A dissertation submitted in partial fulfillment
of the requirements for the degree of
Doctor of Philosophy
(Chemical Engineering)
in the University of Michigan
2016

Doctoral Committee:

Professor Charles W. Monroe, Co-chair
Professor Levi T. Thompson, Co-chair
Professor Suljo Linic
Professor Donald J. Siegel

2016

I dedicate this document to my parents, who taught me the value of an education.

A C K N O W L E D G M E N T S

I'd like to thank my wife Jessica Griffith for her support and help with my doctorate work. I'd like to thank the committee members and Monroe Research Group for their collaboration. I gratefully acknowledge Alice Eleanor Silvia Sleightholme for her council on executing experimental work. I'd also like to thank John Mansfield with the University of Michigan Electron Microbeam Analysis Laboratory for his input on acquiring micrographs of pristine lithium peroxide. I'd like to thank the National Science Foundation and Bosch for providing funding.

TABLE OF CONTENTS

LIST OF FIGURES

LIST OF TABLES

LIST OF ABBREVIATIONS

RFB Redox Flow Battery

XRD X-ray diffractometry

SEM Scanning Electron Microscopy

DME 1,2-Dimethoxyethane

LiTFSI lithium bis(trifluoromethane)sulfonimide

OCP Open Circuit Potential

ABSTRACT

Multi-Component Transport in Next-Generation Batteries

by

Lucas D. Griffith

Chair: Charles Monroe, Levi Thompson

Lithium-ion batteries set a high standard of performance in many regards, however the sustainable energy generation and battery powered electric vehicles of the future will require batteries that outperform present day batteries in a number of ways. Many of the batteries being developed to meet these requirements use multiple components in their electrolytic solutions. This research focuses on parameterizing multi-component transport models for diffusion in such electrolytes and evaluating the effects of multi-component diffusion on overall battery performance.

Motivated by a need to understand active species crossover and selectivity in separators for redox flow batteries, we parameterize the simplest model capable of quantifying the impact of interactions between diffusing ions in the separator. Three diffusion experiments in a batch dialysis cell are used to measure the diffusivity of vanadyl sulfate and sulfuric acid and the interactions between the two. Interdiffusion experiments with the two species suggest that the permeability of the two membranes is similar, which is significant, since the Celgard membranes are much thinner.

We describe how interactions between oxygen and the lithium salt can affect cell potential and rate performance of a lithium/oxygen battery. The quaternary system of a typical lithium/oxygen battery electrolyte consisting

of dimethoxyethane, Li^+, $TFSI^-$, and oxygen is characterized using measurements from literature and measurements of the relaxation of the Open Circuit Potential (OCP) of lithium/oxygen cells when exposed to positive and negative oxygen gradients. High concentration of lithium salt significantly reduces the effective oxygen diffusion coefficient. This will result in limitations in the discharge rate of lithium/oxygen batteries.

The discharge rate is critical to the performance of lithium/oxygen batteries: it impacts both cell capacity and discharge-phase morphology. First-discharge data from dozens of Li/O_2 cells discharged across four rates are analyzed statistically to inform these connections. In the practically significant superficial current-density range of 0.1 to 1 $mAcm^{-2}$, capacity is found to fall as a power law, with a Peukerts-law exponent of 1.6 ± 0.1. SEM imaging of electrodes with near-average capacities provides statistically significant measures of the shape and size variation of electrodeposited Li_2O_2 particles with respect to discharge current.

CHAPTER 1

Introduction

Electrochemical energy storage is a useful tool for a broad range of applications with scales of devices ranging from the hundreds of kilowatt-hours necessary for grid level storage to the tens of milliamp-hours used in commercial watch batteries, with some interesting research on even smaller devices.[1] For every application there is a specific combination of chemistry, geometry, etc. that is optimal; for instance, energy storage designed for the power grid level can be large and heavy, as long as it lasts for many years, as opposed to energy storage designed for transportation, which needs to be light, small, and only needs to last as long as the vehicle. Across all of these possible combinations, however, there is one common characteristic: current in the device is carried by ions diffusing through the electrolytic solution. In addition to the ions carrying the current, there are frequently other species present in the electrolytic solution. Examples include everything from electrolyte additives in lithium-ion batteries, present in relatively low concentrations, to the active species in Redox Flow Battery (RFB) batteries, present at or near their saturated concentration. If the concentration of the other species is high, or if the interaction between the two species is strong, these other species can have a significant effect on the transport of the charge carrying ion and, by extension, the overall performance of the battery. This is why understanding the physics of diffusion of multiple species in electrochemical energy storage systems is so important. This document will focus on measuring multi-component diffusion and evaluating its effect on battery performance and operation, focusing on two battery systems: RFB and Li/O_2 batteries.

1.1 Grid Level Energy Storage

In the near future, batteries could be used to reduce the environmental impact of energy generation and distribution by reducing the usage of fossil fuels. Presently coal burning power plants provide most of the electricity in the US and the rest of the world. In prin-

ciple, with the aid of energy storage, solar and wind power could eventually replace coal burning power plants for energy generation. Both wind and solar energy generation are intermittent, generating power only part of the time, and variable, meaning that while they are providing power, that power fluctuates. This provides enormous challenges when trying to provide the precise synchronization of power generation and consumption necessary for the dependability of electrical power expected by consumers. These challenges could be overcome by large scale energy storage. If the renewables plants were sized such that their generation exceeded consumption while they were active, the excess could be stored and used later during lulls in power generation. Storage with a short time response could also be used to even out instantaneous disparities in power generation and consumption by either storing the excess or providing the dearth. In addition to being useful for integrating renewable energy sources, batteries could perform some similar tasks to increase the efficiency of power distribution from coal burning power plants. For instance, electricity demand usually peaks late in the afternoon. Currently the coal power plants adjust their generation throughout the day to match the average demand, however during these hours of peak demand, additional power plants burning natural gas are required. Properly designed energy storage systems could be used for this purpose, as well as the instantaneous matching of supply and demand. This is one of many examples of uses and synergies for large scale energy storage in the present power grid.[2]

Presently the most promising technology for providing grid level energy storage is the RFB. RFBs differ from other batteries in that they allow for the energy capacity and power of the battery to be controlled separately. In a typical battery, energy is stored through reactions that involve a change of phase for one or more of the ions in the system from the electrolytic solution to the solid electrode. For example, in lead-acid batteries, the sulfate goes from the solution into the electrodes on discharge, and then from the electrodes, back into the solution on charge. In such a system, the energy capacity is determined by the total amount of the limiting ion in the battery, and the power the battery is capable of delivering scales with the surface area of the electrodes. This is why energy capacity and power of these systems are necessarily coupled. In contrast, reactions in a RFB occur solely in the liquid phase. This means that the electrolytic solution can be pumped through a reactor, then stored in tanks. This allows the power of the battery to be controlled by the reactor design and the energy capacity of the battery to be controlled by the size of the storage tanks. While there are a number of interesting RFB chemistries discussed in literature, the system in the most advanced stages of testing is the all-vanadium RFB shown schematically in Figure 1.1.

The popularity of this system stems from its high energy density owing to the high

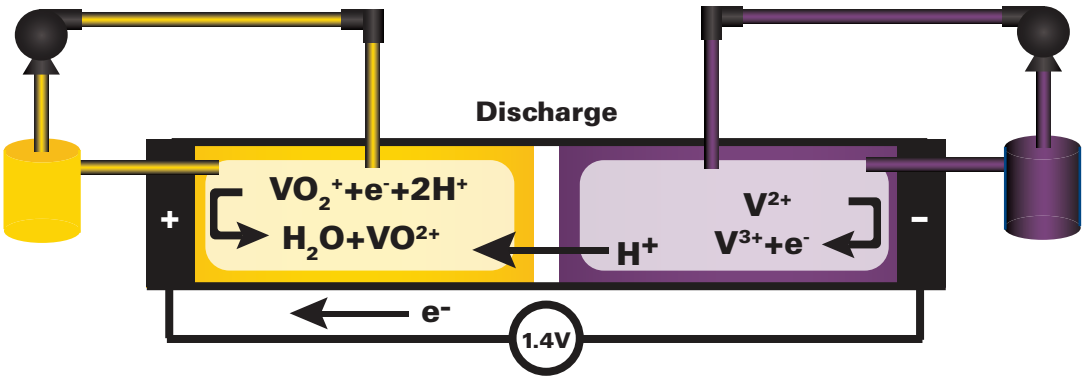

Figure 1.1: Schematic diagram of an all-vanadium RFB and its discharge mechanism. Redox reactions at the electrodes (black) involve various vanadium species, which are dissolved in the catholyte (yellow) and anolyte (purple) liquids. An overall charge balance is maintained by transport of hydrogen ions across the ion-selective membrane (white).

solubility of the vanadium species in the acid electrolytic solution and cell potential that approaches the maximum possible in aqueous solvents. It works by shuffling vanadium between four stable oxidation states; vanadium II and III at the negative electrode and vanadium IV and V at the positive electrode. During these changes, charge in the battery is balanced by transport of H^+ across the membrane. Ion selective membranes are usually used in all-vanadium RFBs to allow facile transport of H^+, minimizing the internal resistance of the battery, while shutting down vanadium transport, maximizing coulombic efficiency. Nafion is the ion selective membrane used by many RFBs, however its extremely high cost has motivated research into alternative membranes. Developing a membrane with the characteristics necessary to replace Nafion is a very challenging task due to the nature of the conditions inside a functioning RFB.

The list of desirable characteristics for a separator for a all-vanadium RFB is long and demanding. One of the least exclusive requirements is that the membrane have the mechanical strength and flexibility necessary for making stacks of RFB cells. The membrane must also be easily wetable; i.e. hydrophilic for aqueous chemistries. A more serious challenge is posed by the charge carrying ions in the battery, typically concentrated H^+ or OH^-. These species are very mobile, owing to their relatively small size, however they are also very reactive. This means that any potential membrane must be highly stable to a very acidic or basic environment. Similarly, the reactivity of the active species in the battery can change with the state of charge. For instance the VO_2^+ produced on charging the all-vanadium RFB is highly reactive with many hydrocarbon membranes.[3] The cherry on top of this requirement sundae is that the membrane must prevent, to the highest possible

extent, the crossover of any active species, while maintaining facile transport of the supporting electrolyte. Any novel membrane must not only demonstrate this extensive suite of characteristics, but also clearly show some advantage over the reigning champion, Nafion.

Clearly, with such a daunting list of challenges, the development of a new membrane for the all-vanadium RFB (or RFBs in general) would benefit from employment of as many highly specialized macromolecular scientists and engineers as possible. Prevalent methods of RFB membrane characterization require testing in an operating RFB, however, posing a significant barrier to many such teams. Aside from not being generally accessible, direct testing in the desired application is usually indicative of characterization methods that have yet to reach their full maturity. Therefore different methods for characterization of transport in membranes for RFBs could be more accessible to and possibly more useful for the people most capable of designing novel membranes.

One promising avenue toward this goal is using the extended Stefan-Maxwell equations to model the multi-component diffusion in membranes for RFBs. Several straightforward measurements can be done to measure the diffusivity of a model vanadium species (vanadyl sulfate in this document) and the supporting electrolyte (sulfuric acid), and the interactions between the two. Though this method does not capture any migration effects. It is useful as a screening tool for novel membranes, and with a few additional measurements the migration effects could be completely accounted for. Chapter 3 will walk through the application of this method to Nafion and Celgard membranes.

1.2 Transportation Energy Storage

1.2.1 Motivation

About 1/3 of energy consumption in US goes to transportation,[4] which is mostly supplied by burning fossil fuels at present. The amount of fossil fuel necessary could be significantly reduced and possibly eliminated by using efficient battery powered electric vehicles instead of fuel burning cars. Since battery powered vehicles can be powered by any electricity source, fuels more plentiful than petroleum, such as coal, can be used. In the future renewable energy sources such as wind and solar could also be used to replace fossil fuel as an energy source altogether.

Presently the largest hurdles for battery powered electric vehicles are high cost of batteries and limited range due to low specific energy and energy density of the batteries. Even with significant improvement, the state of the art lithium-ion batteries used today will likely fall short of future demands. For this reason we need a battery that can operate at similar

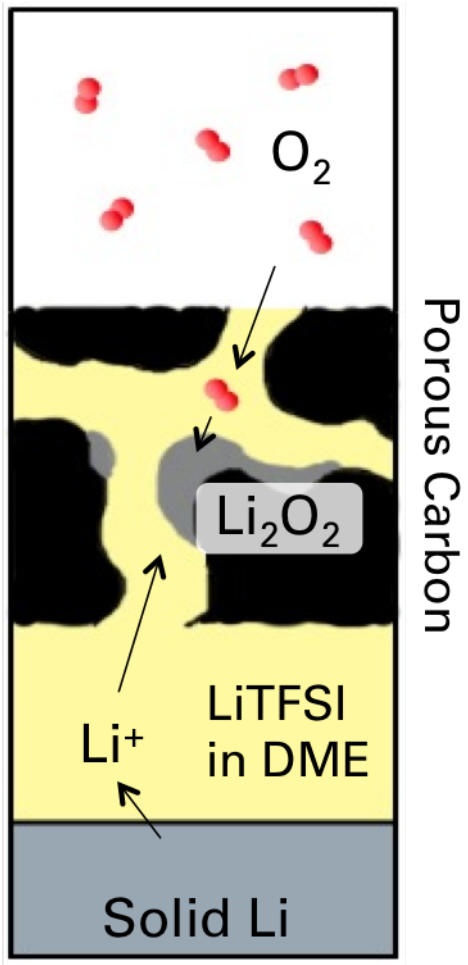

Figure 1.2: Schematic diagram of lithium/oxygen battery and its discharge mechanism. During discharge, lithium is oxidized at the anode and oxygen is reduced at the cathode ideally resulting in solid Li_2O_2 forming on the porous cathode.

rates, cell potentials, and cycling efficiency as state of the art lithium-ion batteries over a similar number of cycles but with higher specific energy and energy density.

1.2.2 Operating Principles of the Lithium/Oxygen Battery

One promising technology is the lithium/oxygen battery, shown schematically in Figure 1.2. Even though the Li/O_2 battery employs lithium to store charge like the lithium-ion battery, the positive electrode, electrolytic solution, and negative electrode are all different.

Ideally, the positive electrode consists of a metallic Li electrode instead of a lithiated carbon electrode. Lithium metal has a very high specific energy and facile electron exchange, making it a reasonable choice for a battery electrode material. Presently, it is not

used in commercial secondary battery systems due to its tendency to form dendrites upon cycling. This problem could possibly be solved by employing a solid separator with sufficient hardness to suppress dendrite growth.[5] In absence of a solution to this problem any lithium ion source, e.g. lithiated carbon or silicon, could serve as the positive electrode. Lithium metal positive electrodes are still a very active field of research.

Given their established ability to dissolve lithium, and stability at the relevant potentials, the carbonate solvents were used in early Li/O2 batteries, however, these batteries suffered from extremely limited cyclability (only achieving ~10 cycles).[6,7] It was established that the carbonate solvents were not stable when oxygen was introduced into the electrolytic solution.[8] 1,2-Dimethoxyethane (DME) was highlighted as a promising candidate for Li/O_2 solvent due to its high oxygen solubility,[9] and shown to be more stable.[10] Also since oxygen must move through the electrolytic solution, solubility and diffusivity of oxygen become critical for the rate performance of the battery.[11]

The most significant differences between a lithium-ion battery and a Li/O_2 are in their negative electrodes. As opposed to the lithium-ion battery, the negative electrode in an Li/O_2 battery does not directly participate in the chemistry, but rather serves as a site for the reduction of oxygen to form lithium peroxide, Li_2O_2. Li_2O_2 is not soluble in any of the solvents studied for Li/O_2 batteries, however, so it is deposited as a solid at the negative electrode.

1.2.3 Challenges

Compared to the Li-ion battery system the Li/O_2 system is in its infancy. As such the challenges the system faces are many and varied. Principle among these challenges are the low cycling efficiency due to high over potential during the charging of the battery, and the low cycle life of the battery. Secondary challenges include issues such as oxygen management and poor rate performance of the battery. Though these challenges are significant, there is also significant research being done on these batteries. Recent years have seen much progress toward identifying the physical processes underlying these challenges and proposing strategies for overcoming them.

One of the most sought after research goals for Li/O_2 batteries is an understanding of the fundamental discharge / charge mechanism, in terms of both the elementary chemical steps comprising the overall reaction as well as the growth and dissolution of the solid Li_2O_2. Many early efforts in this direction were stymied by chemical instability of cell components such as the electrolyte[10], lithium salt[12], and electrodes.[13] It was also determined that water content of the solvent had a significant impact on the operation of the

battery, affecting the microstructure of the discharge product and the capacity and cycle life of the battery.[14] Recent progress supports the hypothesis that the reaction proceeds through a lithium superoxide LiO_2 intermediate.[15–17] The solubility of the LiO_2 intermediate in solution determines the balance between the Li_2O_2 formed directly on the surface and that which precipitates from solution.[17] This level of mechanistic understanding can help explain the successes of various projects yielding relatively high cyclability and efficiency.[18,19] Other groups have used this information to propose new reaction pathways targeting lithium hydroxide instead of Li_2O_2, that are more tolerant of the presence of water.[20]

As the principle challenges of the Li/O_2 battery are met, strategies for overcoming the secondary challenges will be more important. All the systems presently discussed in literature are very sensitive to impurities present in ambient air. Taking a systems level approach, Gallagher *et al.* suggested building the entire battery stack inside a pressurized oxygen vessel would solve this problem while adding minimal weight to the battery system. Several studies have suggested that the poor rate capability of the battery is due to oxygen diffusion limitations.[11,21] The diffusivity of oxygen is the product of its concentration and diffusion coefficient, both of which are possibly affected by the lithium salt. Read *et al.* show that adding 1M lithium hexafluorophosphate to propylene carbonate lowers the oxygen solubility.[9] Hartmann *et al.* show that adding 0.5M sodium triflate to diglyme lowers the effective oxygen diffusion coefficient as well. Understanding the multi-component transport of the solvent, lithium salt, and oxygen will provide a way to predict these dependences. Solvent salt combinations can then be selected based on their oxygen solubility and diffusion coefficient, since both will be important to the operation of the battery.

CHAPTER 2

Experimental Methods

2.1 Transport in membranes for redox flow batteries

2.1.1 Densitometric solubility measurements

Most common methods for solubility measurement require adding the solute to solution until a solid precipitate is observed in the container. For opaque solutions such as vanadium acetylacetonate ($V(acac)_3$), any precipitate is not visible. For this reason, the solution density as a function of concentration for $V(acac)_3$ was used to determine its solubility. If density ρ varies linearly with concentration c then the partial molar volume $\bar{V}$ of the solute is constant[22] and can be calculated from the slope of the density vs. concentration curve at fixed temperature and pressure $(\partial\rho/\partial c)_{T,p}$, the molar mass of the solute M and the solvent density ρ_0.

$$\bar{V} = \frac{M - (\partial\rho/\partial c)_{T,p}}{\rho_0} \tag{2.1}$$

Figure 2.1 shows the density vs. concentration curve for $V(acac)_3$ in acetonitrile used to calculate $\bar{V} = 256$ mL mol^{-1}. It also shows the measured density of a carefully prepared saturated solution of $V(acac)_3$ in acetonitrile. Based on this density and a linear fit of the data the saturated concentration can be calculated

$$c_{\text{sat}} = \frac{\rho_{\text{sat}} - \rho_0}{M - \rho_0 \bar{V}} = 0.59 \pm .02 \text{ M} \tag{2.2}$$

2.1.2 Densitometric preparation of solutions

Detailed density vs. concentration measurements for vanadyl sulfate were performed by Tian-Hong (Saber) Hou. Vanadyl sulfate stock solutions were prepared by dissolving vanadyl sulfate x-hydrate (99.9% metals basis, Alfa Aesar, US) in ultrapure water. The

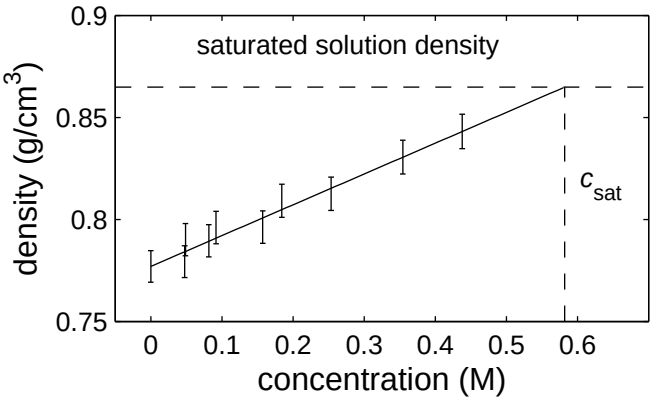

Figure 2.1: Densities of solutions of $V(acac)_3$ in acetonitrile at room temperature fit with a line forced through the density of pure acetonitrile at $c = 0$ allow for calculation of the saturated concentration of $V(acac)_3$ in acetonitrile.

mass fractions of stock solutions were determined using potentiometric titration. A 20 mL sample of the vanadyl sulfate stock solution was taken, massed, and then combined with 5 mL 6M sulfuric acid (99.999% Sigam Aldrich, US) to make the vanadyl /pervanadyl reaction accessible. Sodium oxalate (99.5% purity, Sigma Aldrich, US) standardized potassium permanganate (99.95%purity, Sigma Aldrich, US) was then added to the sulfuric acid, vanadyl sulfate mixture while the potential was monitored with a Hg/HgO reference electrode and a Platinum working electrode. Potassium permanganate drove conversion of vanadyl sulfate to pervanadyl sulfate to completion, resulting in a steep change in electrochemical potential of the solution. The volume of $KMnO_4$ necessary to drive the reaction to completion was then used to calculate the initial vanadyl sulfate concentration. The vanadyl sulfate stock solution was then used to prepare known mass fraction solutions. The density of these solutions was measured using a DMA4100 densitometer(Anton Paar) at temperatures of 15, 20, 25, 30 and 35 °C. The density vs. mass fraction curves were used to calculate concentration of vanadyl sulfate for each mass fraction. The deviation in solution density ρ at concentration c and temperature T from the density of water ρ_w was fit empirically using the form

$$\rho = A_0(T)\left(\frac{c}{c_{\text{ref}}}\right)^{3/2} + A_1(T)\frac{c}{c_{\text{ref}}} + \rho_w(T). \tag{2.3}$$

A reference concentration $c_{\text{ref}} = 1\text{M}$ was chosen to make coefficients A_i have similar units. Fit parameters, A_i, were found to vary linearly with temperature:

$$A_i = A_i^1 \frac{T - T_{\text{ref}}}{T_{\text{ref}}} + A_i^{\text{ref}} \tag{2.4}$$

Table 2.1: Parameters for equations that describe the density of aqueous $VOSO_4$ and H_2SO_4 over the composition range 5mM $\leq c \leq$ 0.5M and temperature range 15°C $\leq T \leq$ 30°C with, c_{ref} = 1M and T_{ref} = 298.15K

		A_i^{ref}	A_i^1
$VOSO_4$	$A_0\left(\text{g cm}^{-3}\right)$	0.0291	-0.0100
	$A_1\left(\text{g cm}^{-3}\right)$	-0.0596	0.153
H_2SO_4	$A_0\left(\text{g cm}^{-3}\right)$	0.0235	-0.00397
	$A_1\left(\text{g cm}^{-3}\right)$	-0.0750	0.0658

A reduced temperature difference relative to the temperature T_{ref} = 293.15K is used here, which allows the A_i^{ref} to be interpreted as the value of the corresponding A_i at 25 °C; division by T_{ref} in the reduced temperature ensures that all the A_i^j have similar units.

Density vs. concentration data for sulfuric acid from the CRC handbook were also fit using a similar procedure. The values of the coefficients for the fits of both sulfuric acid and vanadyl sulfate are given in Table 2.1 and the resulting fits are shown in Figure 2.2

Such a thorough calibration allowed for the precise preparation of solutions of a given concentration at the reference temperature of 25°C. Adding excess solute to a solution, measuring the density, and calculating the mass fraction allowed for the mass of water necessary to achieve the desired mass fraction at the desired concentration to be calculated and added. A density measurement of the resulting solution confirmed the success of the previous steps.

2.1.3 Conductivity Calibrations

Conductivities of solutions were measured using an InLab 731 conductivity probe with a Multi-Seven conductivity meter (Mettler-Toledo, US). Conductivities were measured at temperatures of $15-35\pm0.05$°C using an A-25 circulator (Anova, USA). Between individual conductivity measurements the conductivity probe was rinsed thoroughly with ultrapure water and dried; between experiments, the probe was soaked in a 100 mL bath of ultrapure water overnight. Solution conductivity was monitored to establish the transient evolution of aqueous electrolyte compositions during diffusional relaxation experiments. Accurate correlations between concentrations and conductivities were developed for binary aqueous solutions of $VOSO_4$ and H_2SO_4, for concentrations ranging from 0.001 M to 0.5 M at various temperatures. In binary electrolytic solutions, the ionic conductivity κ is to first order proportional to molar electrolyte concentration c. Therefore the equivalent conductance

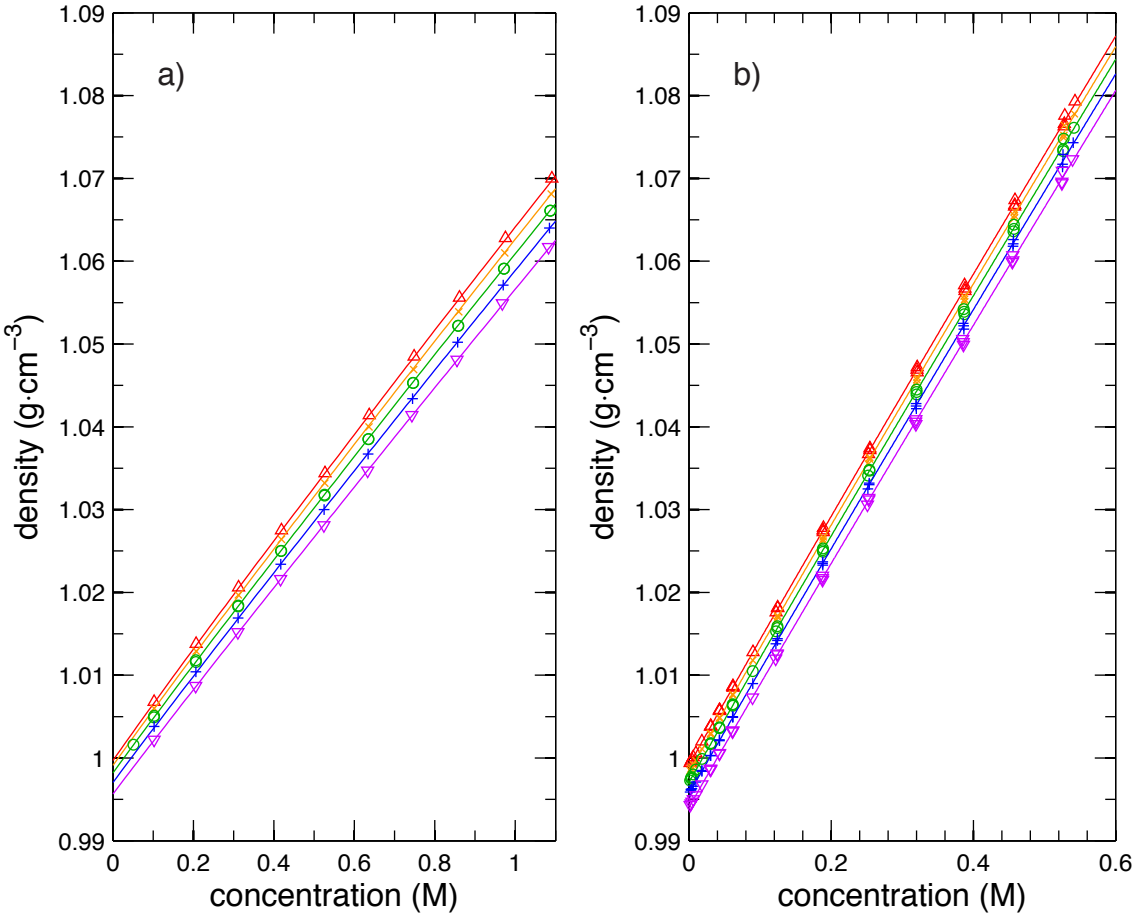

Figure 2.2: Empirical fits of the variation of density with concentration for a) H_2SO_4 and b) $VOSO_4$ where the symbols △, x, ◯, + and ▽ show the density at a) 30, 25, 20, 15, and 10 °C and b) 35, 30, 25, 20, and 15 °C.

$\Lambda\left(\mathrm{S}\cdot\mathrm{cm}^2\mathrm{eq}^{-1}\right)$,

$$\Lambda = \frac{\kappa}{z_+ \nu_+ c} \tag{2.5}$$

was modeled to account for higher-order concentration dependences of measured binary-solution conductivities. Here z_+ is the cation equivalent charge and ν_+, its formula-unit stoichiometry assuming complete dissociation. For solutions containing $VOSO_4$, $z_+ = 2$ eq$\cdot$ mol^{-1} and $\nu_+ = 1$; for those containing H_2SO_4, $z_+ = 1$ eq$\cdot$mol^{-1} and $\nu_+ = 2$. Following the functional dependence predicted by Onsager-Fuoss theory[23], the equivalent conductance Λ of the binary solutions depends on molar concentration c and temperature T through functions of the form

$$\Lambda(T,c) = \Lambda_0(T)\left[1 - \frac{\Lambda_1(T)\sqrt{c/c_{\mathrm{ref}}}}{1+\Lambda_2(T)\sqrt{c/c_{\mathrm{ref}}}}\right]. \tag{2.6}$$

The choice of reference concentration here is arbitrary, and was taken to be $c_{\mathrm{ref}} = 1$M to emphasize that a molar concentration basis was used. To parameterize equation 2.6 for binary aqueous solutions of $VOSO_4$ and H_2SO_4 experimental data were fit using Matlab nonlinear data-processing software to minimize residuals in the fit using the linear relation

$$\Lambda_i = \Lambda_i^1 \frac{T - T_{\mathrm{ref}}}{T_{\mathrm{ref}}} + \Lambda_i^{\mathrm{ref}}. \tag{2.7}$$

A reduced temperature difference relative to the temperature $T_{\mathrm{ref}} = 293.15$K is used here, which allows the Λ_i^{ref} to be interpreted as the value of the corresponding Λ_i at 25 °C; division by T_{ref} in the reduced temperature ensures that all the Λ_i^j have similar units. Table 2.2 summarizes parameter sets for equations 2.6 and 2.7 that describe the equivalent conductances of aqueous $VOSO_4$ and aqueous H_2SO_4 in the composition range 1mM $\leq c \leq$ 0.5 M and temperature range 15 °C $\leq T \leq$ 35 °C. Note that the extrapolative capability of the expressions was not assessed; outside these ranges of composition and temperature, measurements of $\Lambda(T,c)$ could differ significantly from values predicted using the parameters reported here.

Figure 2.3 summarizes the experimental data used to parameterize the conductivity of binary aqueous $VOSO_4$ and H_2SO_4 solutions. The figure also shows the predictions of equations 2.6 and 2.7, illustrating the quality of the equivalent conductance and conductivity correlations achieved with parameters from Table 2.2.

Conductivity was also useful for determining the mol fraction of H_2SO_4 in mixtures of H_2SO_4 and $VOSO_4$ of a given ionic strength. Known mol fraction solutions were prepared by adding a certain mass of stock solution of H_2SO_4 and $VOSO_4$ to a 10 mL volumetric

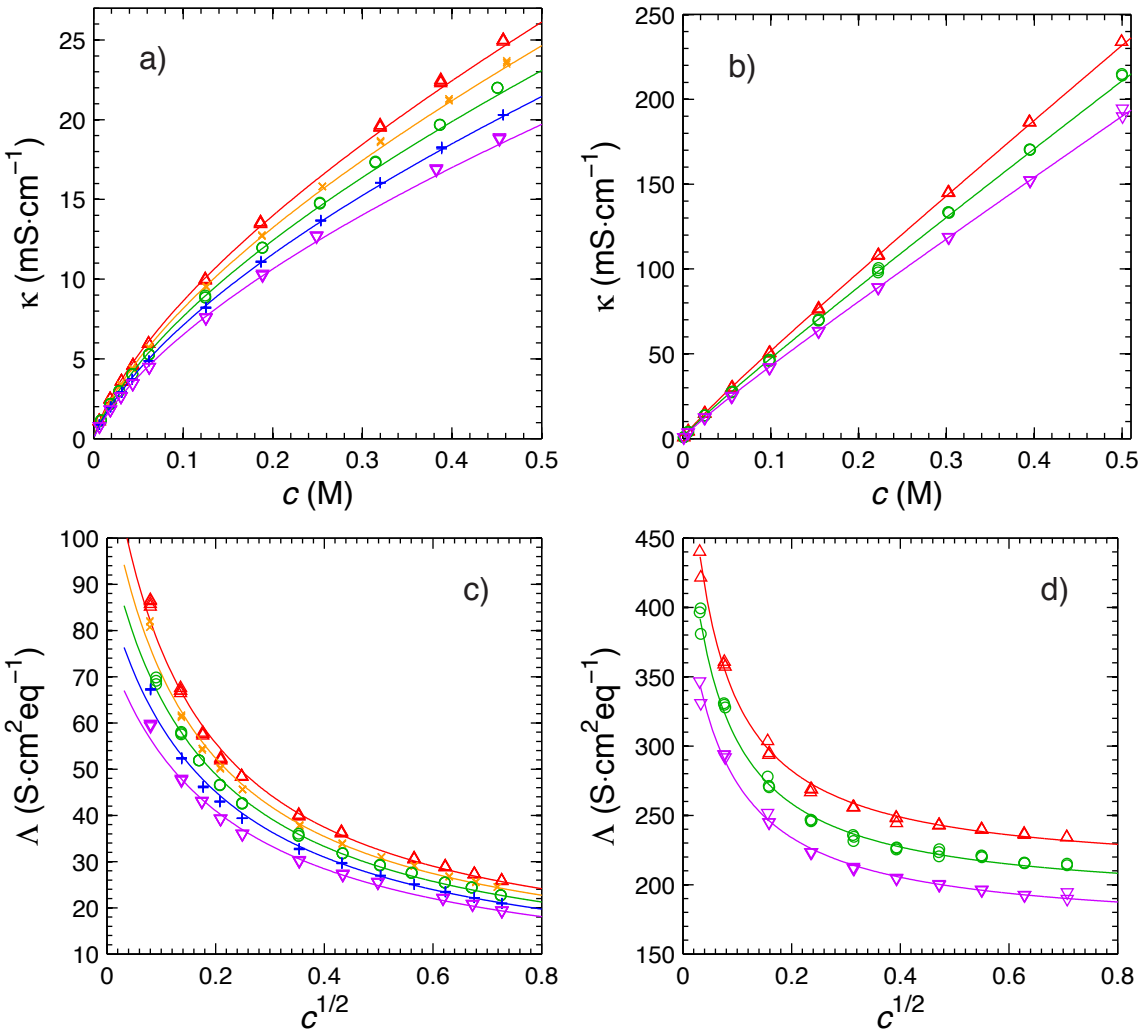

Figure 2.3: Conductivity vs concentration calibrations for $VOSO_4$ and H_2SO_4 allow non-invasive, fast response measurement of the transient concentration in the dialysis cell using conductivity probes. a) and b) show the nonlinear nature of conductivity κ as a function of concentration over the concentration range of interest, and c) and d) show equivalent conductance Λ as a function of $\sqrt{c}$, which provided an excellent fit at all concentrations relevant to the transport study.

Table 2.2: Parameters for Eqs.and that describe the equivalent conductances of aqueous $VOSO_4$, measured by Tian-Hong (Saber) Hou, and aqueous H_2SO_4 over the composition range 1mM $\leq c \leq$ 0.5 M and temperature range 15 °C $\leq T \leq$ 35 °C. In Eqs. and, c_{ref} = 1 M and T_{ref} = 298.15 K.

		Λ_i^1	Λ_i^{ref}
$VOSO_4$	$\Lambda_0\left(\text{S}\cdot\text{cm}^2\text{eq}^{-1}\right)$	708	100
	Λ_1 (unitless)	31.6	5.46
	Λ_2 (unitless)	34.8	5.68
H_2SO_4	$\Lambda_0\left(\text{S}\cdot\text{cm}^2\text{eq}^{-1}\right)$	2360	501
	Λ_1 (unitless)	63.8	10.5
	Λ_2 (unitless)	86.9	16.8

Table 2.3: List of parameters for fitting conductivity vs. mol fraction at temperatures 15-35 °C

a_1 mS cm^{-1}	a_2 mS cm^{-1}	a_3 mS cm^{-1}
-1,000	-82	-5.5

flask, then filling the flask with water. The conductivity meter and water bath were used as described previously to measure the conductivity of solutions with mol fractions of H_2SO_4, x, from 0 to 1, at fixed total concentration of 0.1 M, over the temperature range 15 $\leq$ $T \leq$ 35°C. Conductivities of the mixtures deviated slightly from the line connecting the conductivity of pure $VOSO_4$, κ_{V} and pure H_2SO_4, κ_{H}. The deviation followed a parabolic arc centered at $x = 0.5$. Conductivity vs x was fit empirically with an equation of the form

$$\kappa = \kappa_{\text{H}} x + \kappa_{\text{V}} (1 - x) + a(T)\, x(1 - x) \tag{2.8}$$

where the parameter $a(T)$ varies parabolically with temperature

$$a(T) = a_1 \left(\frac{T - T_{\text{ref}}}{T_{\text{ref}}} \right)^2 + a_2 \frac{T - T_{\text{ref}}}{T_{\text{ref}}} + a_3. \tag{2.9}$$

Again the reduced temperature difference relative to the temperature T_{ref} = 293.15K ensures each a_i has the appropriate unit (mS cm^{-1}). Parameters expressing the temperature dependence of a are given in table 2.3.

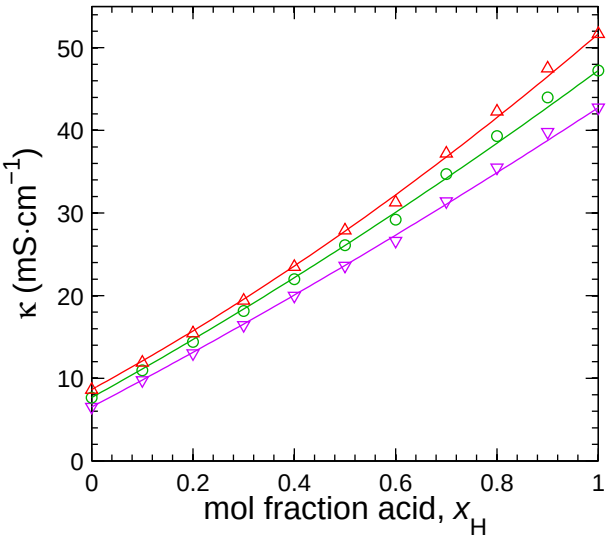

Figure 2.4: Conductivity vs acid mol fraction at a fixed total concentration of 0.1 M at temperatures of ▽15°C, ◯25°C, △35°C.

2.1.4 Batch dialysis cell

The batch dialysis cell used in diffusion experiments comprised two vertical glass tubes, meeting in an ”H” shape with the face of each side of the glass tubes compressing a membrane sandwiched by two gaskets. The cell was custom made by a master glass blower, to minimize the distance of the horizontal union, ensuring solutions could be mixed well by stir bars at the bottom of the vertical tubes. The vertical tubes of glass terminated in #15 threaded glass fittings (ACE glass, USA), so the cell could be sealed to prevent evaporation in longer diffusion experiments. The conductivity probe fit through one of these fittings, and an o-ring at the bottom of the threads compressed around the circumference of the conductivity probe when the threads were screwed down, providing a seal. The cell was seated in a clamp with four thumb screws that provided pressure on the gaskets to provide a good seal at the union of the gasket and the glass. The gaskets had an inner diameter of 0.5”, slightly less than the 15 mm tube diameter, and a thickness of 0.125”.

2.2 Li/O_2 cell experiments

2.2.1 Materials

Electrolytic solutions were prepared by dissolving lithium bis(trifluoromethane)sulfonimide (LiTFSI) (99.95%, Sigma-Aldrich, USA) to 1 M concentration in DME (99.5% anhydrous, Sigma-Aldrich, USA), which was dried over 4 molecular sieves (Fisher Scientific, USA). Each electrochemical cell employed a 0.75 mm thick, 18 mm diameter Li disk negative electrode (99.9%, Alfa Aesar, USA), a 0.55 mm thick, 18 mm diameter glass-fiber separator (EL-CELL GmbH, Germany), and an 18 mm diameter porous-carbon positive electrode (SIGRACET GDL 24 BC, Ion Power, Inc., USA). Both electrodes were cut from larger sheets of material using a steel punch. The average positive-electrode mass was 0.0265 g; its porosity, 0.8 (as per supplier); its thickness, 235±20 μm (as per supplier); and its specific surface area, 13.3±0.2 m^2g^{-1} (measured by N_2 physisorption with a Micromeritics ASAP 2010 analyzer employing the Brunauer-Emmett-Teller isotherm). Positive electrodes and separators were dried under vacuum at 110°C for 12 h to remove residual water.

2.2.2 Electrochemical cell cleaning

After tests were completed and any cell components of interest were harvested, the cells were disassembled, and placed in 250 mL beakers with 2 cells per beaker. The cells were then cleaned by sonicating in detergent, acetone, and ultra pure water sequentially, with several ultra pure water rinses in between different cleaning solutions. After this cells were stored in an oven at 80 °C for at least 12 hrs.

2.2.3 Electrochemical cell assembly

ECC-AIR metal-oxygen electrochemical test cells were purchased from EL-CELL GmbH (Germany). Cells were assembled in an Omnilab glove box (Vacuum Atmospheres, USA) with an Ar atmosphere (99.998%, Cryogenic Gases, USA) containing less than 1 ppm O_2 and less than 1 ppm H_2O. To prepare cells for discharge experiments, the vacuum-dried glass-fiber separator and positive electrode were soaked in the electrolytic solution for 1 min, after which the positive electrode was sandwiched between the separator and a perforated stainless-steel current collector. The wetted, stacked assembly was then slid into a cylindrical polyether ether ketone (PEEK) sleeve, leaving the soaked glass-fiber surface exposed. The Li foil was subsequently placed onto the glass-fiber surface, after which the entire assembly within the PEEK sleeve was inserted into a stainless-steel cell base, which

acted as the current collector for the negative electrode. The base was then sealed using an electrically isolated stainless-steel cap containing a spring-loaded, hollow piston that applied reproducible pressure on the stacked assembly; the spring was gold, also providing electrical contact with the positive current collector. The opening in the piston allowed distribution of gases to the positive electrode through the perforated plate.

2.2.4 Electrochemical cell gas manifold connections

Oxygen was supplied to the cells using a steel gas manifold. The gas manifold had 6 swagelok connections, which could supply either oxygen or argon to the cells and collect any exhaust gas from the cells, pass it through a bubbler, and carry it to the fume hood. Each cell was equipped with a three way valve on the supply line and a two way valve on the exhaust line. Once cells were connected to the gas manifold, the three way valve on the cells was used to purge the gas in the manifold lines through to the exhaust, removing any impurities that may have accumulated while the gas was stagnant. During the purge the pressure of the supply gas was set to 1 bar, and gas was allowed to flow for about 10 min. After the lines were purged, the argon atmosphere from the glove box in the cells was exchanged for an oxygen atmosphere by switching the three way valve to allow oxygen to enter the cell, opening the exhaust valve, and allowing the oxygen to flow through the cell for about 1 min. The exhaust valve was then sealed so the pressure in the cell could be set using the pressure regulator.

To initiate each test, a Series 4000 battery tester (Maccor, USA) was used to hold the assembled, sealed cell at open circuit until the rate of voltage change was observed to fall below 2 mVh^{-1}. Throughout the test a series HP702 pressure regulator (Harris Specialty Gas, USA) was used to maintain the pressure of stagnant O_2 gas (99.993%, Cryogenic Gases, USA) at 1 bar gauge. Once the test was completed, cells were purged with Ar gas, sealed and transferred to the glovebox for removal of the positive electrode.After the initial equilibration period (typically about 12 h), cells were discharged at constant current densities of 0.1, 0.2, 0.5, or 1.0 $mAcm^{-2}$ (superficial) until the voltage reached a lower cutoff of 2.0 V. Every cell was purged with Ar gas and sealed immediately after first discharge. (Control experiments were also run, by holding assembled cells at zero current under 1 bar gauge O_2 pressure for 24 h.)

2.2.5 Ex Situ Characterization

After discharge/charge testing was complete, cells were disassembled in the glove box. Positve electrodes were removed and rinsed with 10 mL of sieved DME, after which they

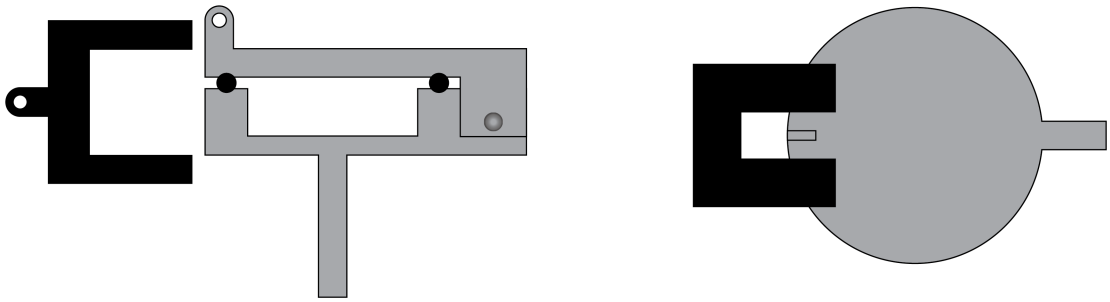

Figure 2.5: Airtight SEM sample holder schematics. Left: side view (of central cross section); Right: top view. The black portion represents the Be/Cu-alloy spring clamp.

were dried at room temperature under vacuum in the glove box antechamber for 20 min and returned to the main chamber. After removal, each electrode was sectioned into eight smaller samples for XRD and SEM using steel scissors.

XRD samples were prepared in the glove box by placing sections of the discharged electrodes in an airtight sample holder with a Be window (2455-SH-001, Rigaku, Japan). Diffraction patterns were gathered by a Rotaflex (40 kV, 100 mA) diffractometer (Rigaku, Japan) with a Cu source, using continuous scan at 0.75° min^{-1} in 2θ mode.

SEM samples were prepared in the glove box and transferred to the microscope chamber using an airtight holder designed and fabricated in house, to prevent exposure of samples to ambient air prior to micrograph acquisition. The sample holder comprised a clamshell design with a hinged Al cap atop a hollow Al cylindrical base that also served as a pin stub. After samples were anchored on double-sided Cu tape inside the hollow cylindrical cavity, the cap was wedged tightly in contact with an o-ring on the lip of the base by a u-shaped Be/Cu-alloy spring clamp attached in opposition to the hinge. For transfer to the SEM facility, the clamped sample holder was placed inside an airtight storage container in the glove box. Once removed from the glove box and transported to the microscope, the container was opened and the clamped sample holder was placed inside the SEM chamber. The spring clamp was affixed to an interior wall of the chamber with a taut wire, allowing it to be removed by translation of the sample stage after the chamber was closed and vacuum was drawn. The hinged cap was also affixed to an interior wall of the chamber with a second wire. After removal of the clamp, 180 rotation of the stage allowed the hinged cap to be opened, revealing the sample. Schematic diagrams of the sample holder and spring clamp are shown in Figure 2.5. SEM was performed with a FEI Nova NanoLab microscope (5 kV accelerating voltage, 98 pA). SEM images were gathered using a 50 ns acquisition time and integrating 64 frames. Particle dimensions were analyzed with SPIP software.

CHAPTER 3

Mass Transport in Membranes for Redox flow batteries

3.1 Introduction

RFB systems may provide the scalable capacity and long cycle life demanded by utility-storage applications.[24–27] Unlike conventional battery systems, the energy in RFBs is stored in a liquid phase. This design decouples energy capacity, which determines the volumes of the active liquids used, from power capability, which determines the reactor size. Presently the aqueous all-vanadium RFB, based on the reaction

$$VO_2^+ + 2H^+ \rightleftarrows H_2O + VO^{2+} \tag{3.1}$$

is one of the most popular commercially available chemistries. Skyllas-Kazacos *et al.* have identified the battery separator typically an ion-exchange membrane as one of the key barriers for this technology.[24,28] The important role separators play in determining RFB efficiency, and their significant contribution to reactor cost, have inspired a lot of recent research focused on creating robust, economical membranes.[24] Modeling can be a powerful tool to evaluate the effects of various control conditions and reactor designs on RFB performance, but accurate RFB reactor simulations require accurate characterizations of the multicomponent transport processes that take place in RFB membranes. During RFB operation, active species and the supporting electrolyte are able to diffuse through the separator membrane. Facile transport of support ions is necessary to maintain charge balances in the RFB liquids as electrode reactions occur. An ideal membrane is selective to the supporting electrolyte alone, because active-species crossover leads to coulombic inefficiency.[27] Typically, separators for all-vanadium RFBs are cation-exchange membranes. Since H^+ transport tends to be relatively fast, such membranes provide high ionic conductivity, reducing ohmic losses. Given that all the vanadium-containing redox-active species in equation 3.1

are also cations, some active-species crossover is likely unavoidable in all-vanadium RFBs.

To assess the viability of a separator for all-vanadium RFB applications, it is critical to understand its tendency to absorb (uptake) active species, and to know the relative rates of active-species and supporting-electrolyte diffusion. It is also of scientific interest to investigate the simultaneous diffusion of active species and supports, to establish how interactions between components affect membrane selectivity and crossover rates.

Many groups have recently focused on developing, evaluating, and characterizing membranes for all-vanadium RFBs.[29–33] The ionic conductivity of a membrane is a standard figure of merit, with a value for any given membrane being reproducible across various research efforts. Some research groups have also studied ion crossover in detail, either through commercially available Nafion™, or through novel modified membranes.[34–36] Vanadium permeability (the product of diffusivity and molar concentration) is a common metric used to assess a membranes tendency toward crossover. Usually vanadium transport is assessed in the presence of a supporting electrolyte, typically sulfuric acid, however concentrations of vanadium species and support vary across different experiments, making the effect of vanadium uptake on transport difficult to parse. Also, most mass-transfer analyses assume that ion-ion interactions within the membrane can be neglected, and that the anion chosen for the vanadium-containing electrolyte does not significantly affect transport rates.

Instead of focusing on detailed transport measurements, the impact of the ionic conductivity and vanadium permeability is often assessed by actually testing a given membrane in a working RFB reactor and comparing the performance of the system as a whole to a similar RFB with a different separator.[32,33,37,38] This system-level engineering path is undeniably the ultimate determinant of a membrane's utility for an RFB application, but it provides minimal information about how to improve particular characteristics of a given membrane; system-level analyses also do not provide a standard basis by which materials can be compared. Independent transport and sorption measurements provide useful quantitative membrane-performance metrics that may better inform RFB separator design.

The equilibrium relationship between the molar concentration of a solute in a membrane and its molar concentration in an adjacent aqueous solution can be described using a formulation similar to Henry's law, where a partition coefficient K expresses the concentration ratio at equilibrium. Wiedemann *et al.* measured partition coefficients of $VOSO_4$ in Neosepta cation-exchange membranes,[39] and observed values as high as $K = 40$ in some cases (i.e., the concentration of vanadium in the membrane could be as much as 40 times higher than its concentration in an adjacent aqueous solution at equilibrium). Since the relaxation time in a concentration cell depends on both the partition coefficient and the diffusivity, such sorption measurements are critical to the accurate determination of perme-

ability.

Transport across RFB membranes is complicated by the fact that multiple species are present within them. The analysis of permselectivity in concentrated multicomponent electrolytes is confounded by solute-solute diffusional interactions, which are often significant in electrochemical systems. Canonical work by Wendt showed that the diffusivity of H_2SO_4 through Na_2SO_4 in aqueous solution is comparable in magnitude to both the H_2SO_4/H_2O and Na_2SO_4/H_2O diffusivities.[40] Such electrolyte/electrolyte interactions are also probably important in membrane diffusion. A study by Heintz *et al.* showed that the H^+/Na^+ ion/ion diffusivity in a Neosepta cation-exchange membrane was comparable in magnitude to the ion/membrane diffusivites; a similar observation was made for $Br^-$and Cl^- with an AMS anion-exchange membrane.[41] These observations were additionally corroborated by Wiedemann *et al.* [20], who investigated a number of cation-exchange membranes. In light of these observations, it is likely that vanadium-ion/H^+ interactions strongly affect overall transport rates in RFB membranes.

This study uses vanadyl sulfate, $VOSO_4$, as a model for the vanadium active species involved in the all-vanadium RFB cell reaction 3.1. Detailed correlations are developed to relate the conductivities of aqueous solutions of $VOSO_4$ and H_2SO_4 to their concentrations in binary or ternary solutions. Using this information, measurements of conductivity can be used to determine the evolution of concentrations with respect to time on either side of a dialysis cell during a diffusional relaxation experiment.

A novel implementation of Barnes's classical model of dialysis-cell diffusion[42] is applied to measure the binary diffusion coefficients and sorption equilibria for single solutes ($VOSO_4$ or H_2SO_4) in both a porous membrane and a cation-exchange membrane. With the binary diffusion and uptake measurement in hand, a computer simulation based on the extended Stefan-Maxwell analysis of Heintz *et al.*[41] is used to establish parameters that describe the drag forces $VOSO_4$ and H_2SO_4 exert on each other as they interdiffuse through membranes.

3.2 Theory

A closed dialysis cell was used to measure diffusion coefficients; parameters relevant to the time evolution of concentration profiles are depicted schematically in Figure 3.1. The liquids on either side of the cell are assumed to be stirred with a characteristic mixing time sufficiently short in comparison to the timescales for membrane diffusion that the concentration of species i varies only with time t, $c_i^1(t)$ and $c_i^2(t)$. Transport in the separator is mass-transfer limited, so the concentration of a species in the membrane can vary both

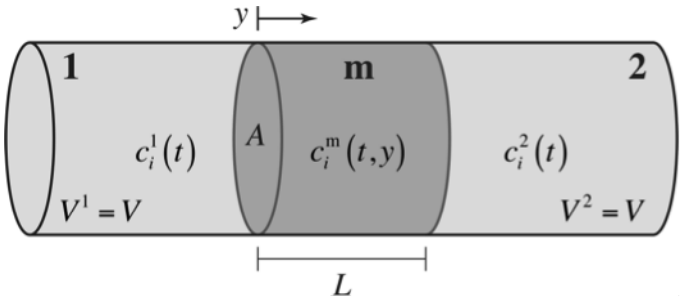

Figure 3.1: Schematic diagram of the dialysis cell (not to scale) that illustrates geometric parameters, including chamber volumes V_1 and V_2, membrane area A, and membrane thickness L. During experiments, solutes travel between well-stirred liquid chambers 1 and 2 through the membrane m.

with time and position y, $c_i^{\mathrm{m}}(t,y)$.

During relaxation of the dialysis cell, the concentration of species i can be taken to satisfy transient material balances

$$V_1 \frac{dc_i^1}{dt} = -AN_i^{\mathrm{m}}(t,0) \quad \text{and} \quad V_2 \frac{dc_i^1}{dt} = -AN_i^{\mathrm{m}}(t,L), \tag{3.2}$$

where $N_i^{\mathrm{m}}(t,y)$ is the molar flux of species i in the y direction inside the membrane, $V_1 = V_2 = V$ is the volume of the liquid in the chambers adjacent to the membrane, A is the membrane area, and L is the membrane thickness. Within the membrane, solute i satisfies a transient local material balance

$$\frac{\partial c_i^{\mathrm{m}}}{\partial t} = -\frac{\partial N_i^{\mathrm{m}}}{\partial y}. \tag{3.3}$$

Sorption kinetics is assumed to be sufficiently fast that at the membrane surfaces, the concentrations of vanadyl sulfate V and sulfuric acid H instantaneously equilibrate with the adjacent solutions,

$$\begin{bmatrix} K_{\mathrm{V}} & \beta c_{\mathrm{V}}^1 \\ \beta c_{\mathrm{H}}^1 & K_{\mathrm{H}} \end{bmatrix} \times \begin{bmatrix} c_{\mathrm{V}}^1(t) \\ c_{\mathrm{H}}^1(t) \end{bmatrix} = \begin{bmatrix} c_{\mathrm{V}}^{\mathrm{m}}(t,0) \\ c_{\mathrm{H}}^{\mathrm{m}}(t,0) \end{bmatrix}$$
$$\begin{bmatrix} K_{\mathrm{V}} & \beta c_{\mathrm{V}}^2 \\ \beta c_{\mathrm{H}}^2 & K_{\mathrm{H}} \end{bmatrix} \times \begin{bmatrix} c_{\mathrm{V}}^2(t) \\ c_{\mathrm{H}}^2(t) \end{bmatrix} = \begin{bmatrix} c_{\mathrm{V}}^{\mathrm{m}}(t,L) \\ c_{\mathrm{H}}^{\mathrm{m}}(t,L) \end{bmatrix}. \tag{3.4}$$

Here, binary partition coefficients K_{V} and K_{H} can be thought of as equilibrium constants

for sorption for vanadyl sulfate and sulfuric acid respectively. The parameter β describes the effect of the presence of one species in the membrane on the sorption of the other. Governing equations and boundary conditions 3.2, 3.3 and 3.4 were used to model both binary and ternary diffusion experiments.

The flux laws used for multicomponent diffusion are based in the Onsager-Stefan-Maxwell theory,[43,44] in which the fundamental transport constitutive law is

$$-c_i\frac{\partial\mu_i}{\partial y}=\frac{RT}{c_{\mathrm{T}}}\sum_{j\neq i}\frac{c_jN_i-c_iN_j}{\mathscr{D}_{ij}}. \tag{3.5}$$

Here R is the ideal gas constant T is the absolute temperature, $c_{\mathrm{T}}=\sum_i c_i$ is the total molar concentration of the condensed phase, and $\mathscr{D}_{ij}$ is the Stefan-Maxwell coefficient describing the diffusional conduction of species i through j (or j through i since $\mathscr{D}_{ij}=\mathscr{D}_{ji}$). The chemical potential gradient is assumed to satisfy a constitutive law

$$\frac{\partial\mu_i}{\partial y}=\left(\frac{\partial\mu_i}{\partial\ln c_i}\right)_{T,P,c_{j\neq i}}\quad\frac{\partial\ln c_i}{\partial y}=\frac{RT\mathscr{X}_i}{c_i}\frac{\partial c_i}{\partial y} \tag{3.6}$$

in which the Darken thermodynamic factor $\mathscr{X}$ is predominately determined by the concentration of species i, independent of the concentrations of all other species. For simplicity, it is convenient to rewrite the Onsager-Stefan-Maxwell equations as

$$-\frac{\partial c_i}{\partial y}=\sum_{j\neq i}\frac{c_jN_i-c_iN_j}{c_{\mathrm{T}}D_{ij}}, \tag{3.7}$$

where $D_{ij}=\mathscr{X}\mathscr{D}_{ij}$ defines a Fickian diffusivity.

Once constitutive law 3.6 is inserted, a standard inversion procedure[45,46] can be used to put equation 3.7 in the flux-explicit form

$$N_i=\sum_{k\neq m}L_{km}\nabla c_k+\frac{c_i}{c_{\mathrm{m}}}N_{\mathrm{m}}=\sum_{k\neq m}L_{km}\nabla c_k, \tag{3.8}$$

where the last equality comes from the assumption that the membrane, being stationary, does not move so $N_{\mathrm{m}}=0$ uniformly.

3.2.1 Binary Diffusion Experiments

In cases where a single solute diffuses, the flux of i through the membrane is described to a first approximation by a constitutive law similar to Ficks law,

$$N_i^{\mathrm{m}} = -L_{i\mathrm{m}} \frac{\partial c_i^{\mathrm{m}}}{\partial y} \quad \text{in which} \quad L_{i\mathrm{m}} = \frac{c_{\mathrm{T}} D_{i\mathrm{m}}}{c_{\mathrm{m}}}. \tag{3.9}$$

Binary diffusion experiments were performed using a membrane equilibrated with ultra pure water, in contact with volume V of ultrapure water in chamber 2. At time $t = 0$, chamber 1 was loaded with a volume V of an aqueous solution with given initial concentration of solute i. Thus the initial conditions for binary diffusion experiments were

$$c_i^{\mathrm{m}}(0, y) = 0, \quad c_i^2(0) = 0, \text{ and } \quad c_i^1(0) = c_i^0. \tag{3.10}$$

In a classic paper Barnes provided a general path to solving governing equations 3.2, 3.3, and 3.9, subject to boundary conditions 3.4, with initial conditions 3.10, for the case of binary diffusion.[42] Note that in this analysis, the solute ($VOSO_4$ or H_2SO_4) is treated as a single entity, and hydrated membrane is considered to be the diffusion medium.

For the present analysis it suffices to use Barness method to solve only for the transient solute concentration in chamber 2 of the dialysis cell; the side that is initially unloaded with solute. The problem is simplified by introducing a dimensionless concentration θ_i^2, time τ, and partition coefficient γ,

$$\theta_i^2 = \frac{c_i^2}{c_i^0}, \quad \tau = \frac{L_{i\mathrm{m}} t}{L^2}, \quad \text{and} \quad \gamma = \frac{ALK_i}{V_1} \tag{3.11}$$

where L is the membrane thickness. The transient concentration distribution is then

$$\theta_i^2(\tau) = \theta_{\mathrm{eq}}^2 + 2\gamma \sum_{m=1}^{\infty} \frac{\left(\gamma^2 - \lambda_m^2\right) \sec \lambda_m \exp -\lambda_m^2 \tau}{\left[\gamma(1+\gamma) + \lambda_m^2\right]^2 - \gamma^2} \quad \text{where} \quad \theta_{\mathrm{eq}} = \frac{1}{2+\gamma}. \tag{3.12}$$

Here the eigenvalue λ_m is computed by finding the mth smallest positive real value satisfying

$$\tan \lambda_m = \frac{2\gamma\lambda_m}{\lambda_m^2 - \gamma^2}. \tag{3.13}$$

Equations 3.12 and 3.13 identify with the solution provided by Barnes.

Although no approximations about parameter sizes will be made in this work, asymptotic analysis helps to get a better qualitative understanding of the content of equations 3.12 and 3.13. In the asymptotic regime where $\gamma << 1, \lambda \approx \sqrt{2\gamma}$; then, when τ is relatively

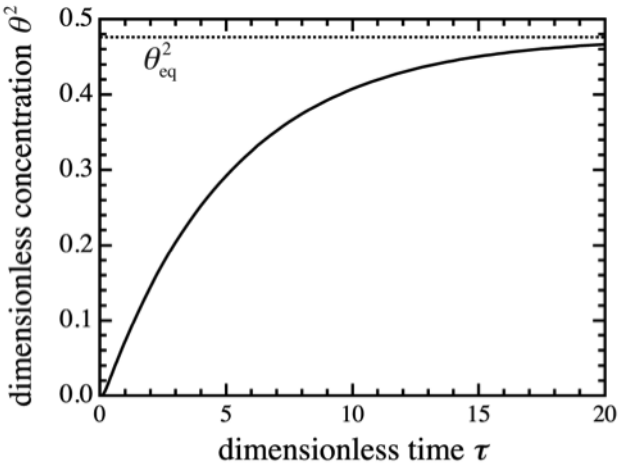

Figure 3.2: Relaxation of the dimensionless concentration in the initially unloaded chamber of the dialysis cell, described by equations 3.12 and 3.13 with $\gamma = 0.1$.

large, equation 3.12 expresses simple exponential decay to an equilibrium of about $^1/_2$, $\theta(\tau) \approx {}^1/_2 - {}^1/_2 e^{-2\gamma\tau}$. Most experiments are fit well by this expression at long times, since K_i is of order unity and the ratio of membrane volume to liquid volume AL/V tends to be very small. Observe that the relaxation time depends on both τ and γ - both the diffusivity and the partition coefficient are involved.

Figure 3.2 shows the result of equation 3.12 for a relaxation experiment in which $\gamma = 0.1$ an extremely large value, chosen to exaggerate some of the qualitative features of the data in Figure 3.3. Over time, there is a relaxation to the equilibrium concentration θ_{eq}. Conductimetric measurements in the unloaded chamber yield raw data with this overall appearance.

Figure 3.3a illustrates the special character of the system response at short times. Since the membrane is initially devoid of solute, the concentration in chamber 2 does not begin to rise until sufficient time has elapsed for the diffusion boundary layer to penetrate through the membrane. This onset time τ_{onset}, at which the concentration first begins to rise appreciably in the unloaded chamber, depends on the dimensionless partition coefficient γ.

For any value of γ, the $\theta^2(\tau)$ curve passes through an inflection point, at which the transient concentration goes from being concave up to concave down. The time when this inflection occurs is labeled τ_{inf} in Figure 3.3a. The onset time was defined formally by dropping a tangent from the inflection point and extrapolating to the intercept at the abscissa:

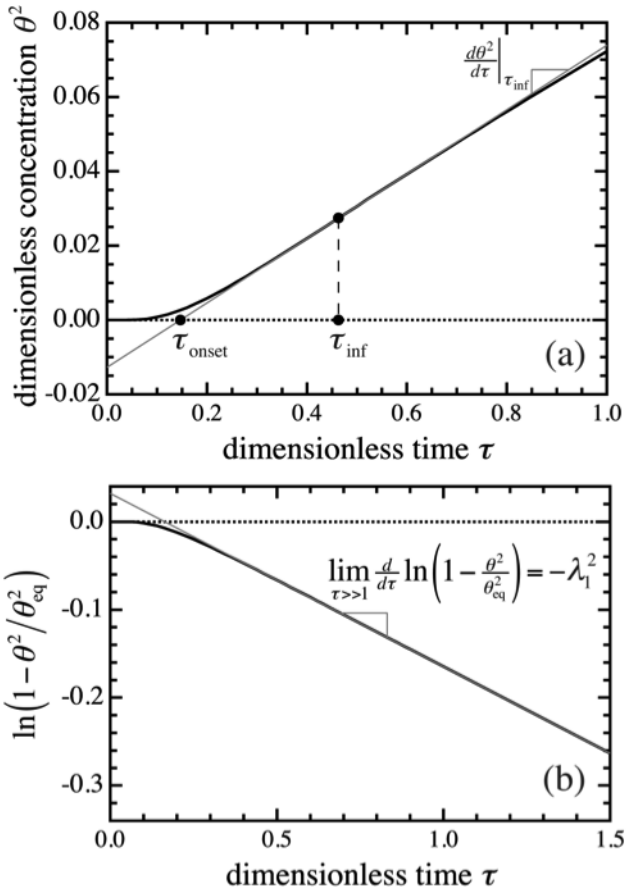

Figure 3.3: Alternative ways of plotting the relaxation data from Figure 3.2. (a) At short times there is a lag in the concentration rise, which begins at τ_{onset}. There is an inflection point in the transient concentration at τ_{inf}. (b) At longer times, the relaxation becomes a simple exponential decay; the slope of $1 - \frac{\theta^2}{\theta_{\text{eq}}^2}$ on a semilog plot relates to the first eigenvalue from equation 3.13.

$$\tau_{\text{onset}} = \tau_{\text{inf}} - \frac{\theta^2(\tau_{\text{inf}})}{(d\theta^2/d\tau)|_{\tau_{\text{inf}}}} \tag{3.14}$$

The procedure for determining τ_{onset} is also depicted graphically in figure 3.3a. Figure 3.3b shows that an essentially exponential decay dominates the response by dimensionless times of order unity, and that the slope of a plot of $\ln\left(1 - \frac{\theta^2}{\theta^2_{\text{eq}}}\right)$ with respect to dimensionless time τ relates directly to the first eigenvalue from equation 3.13.

The diffusivity and partition coefficient were measured simultaneously using a single set of transient concentration data gathered from the unloaded chamber of the dialysis cell. Data were plotted as molar concentration with respect to time, $c^2(t)$. Using short-time data, a dimensional onset time, τ_{onset}, was calculated using an extrapolation similar to that in Figure 3.3a. Data at longer times were plotted as $\ln\left(1 - \frac{c^2}{c^2_{\text{eq}}}\right)$ versus time (in seconds), and were fit with a linear function, with the parameter c^2_{eq} chosen to minimize residuals. The slope of this line, S, has units of inverse seconds, and relates to the first eigenvalue through $S = \lambda^2 L_{i\text{m}}/L^2$. The product $-S\,t_{\text{onset}} = \lambda_1^2 \tau_{\text{onset}}$ corresponds to a unique γ value, following the correlation shown in Figure 3.4 (or a Matlab routine that performs the inversion). Once γ was known, it was used to compute K_i through equation 3.11; the first eigenvalue was computed directly using equation 3.13, and the solutes Onsager diffusivity $L_{i\text{m}} = -S\,L^2/\lambda_1^2$ was calculated from the relaxation slope.

3.2.2 Interdiffusion

Simultaneous diffusion of $VOSO_4$ and H_22SO_4 across the dialysis cell can be modeled as a ternary ($VOSO_4$/H_2SO_4/hydrated membrane) diffusion scenario, following the assumptions made by Wendt.[40] Material balances and boundary conditions in this case are still given by equations 3.2-3.4, with that set of equations written to describe each solute i ($VOSO_4$ and H_2SO_4). A Stefan-Maxwell equation in the form of equation 3.5 applies to each solute species; with no membrane flux the system can be written as

$$\frac{\partial c_{\text{V}}}{\partial y} = -\frac{1}{c_{\text{T}}} N_{\text{V}} \left(\frac{c_{\text{H}}}{\mathscr{D}_{\text{VH}}} + \frac{c_{\text{m}}}{\mathscr{D}_{\text{Vm}}} \right) N_{\text{V}} + \frac{c_{\text{V}}}{c_{\text{T}} \mathscr{D}_{\text{VH}}} N_{\text{H}} \tag{3.15}$$

$$\frac{\partial c_{\text{H}}}{\partial y} = -\frac{c_{\text{H}}}{c_{\text{T}} \mathscr{D}_{\text{HV}}} N_{\text{V}} + \frac{1}{c_{\text{T}}} \left(\frac{c_{\text{V}}}{\mathscr{D}_{\text{HV}}} + \frac{c_{\text{m}}}{\mathscr{D}_{\text{Hm}}} \right) N_{\text{H}} \tag{3.16}$$

These equations invert to yield

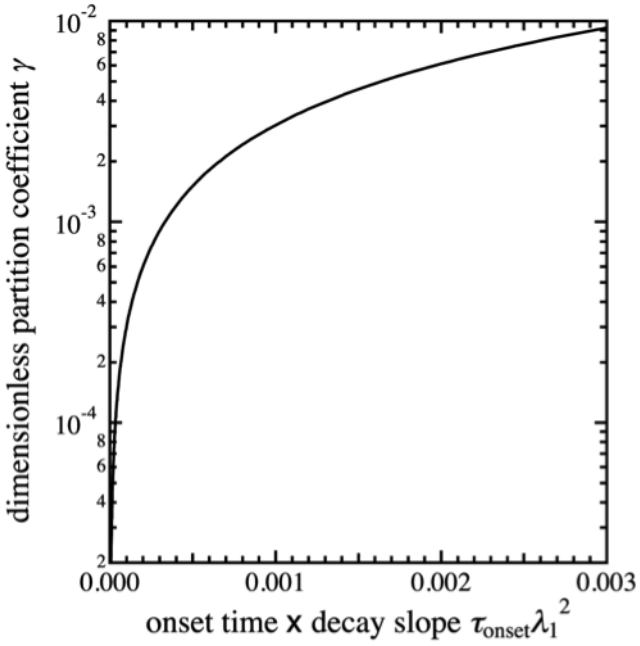

Figure 3.4: Plot of the relation between $\lambda_1^2\tau_{\text{onset}}$, which is directly experimentally measurable, and the dimensionless partition coefficient γ.

$$N_{\text{V}} = -L_{\text{VV}}\frac{\partial c_{\text{V}}}{\partial y} - L_{\text{VH}}\frac{\partial c_{\text{H}}}{\partial y} \tag{3.17}$$

$$N_{\text{H}} = -L_{\text{HV}}\frac{\partial c_{\text{V}}}{\partial y} - L_{\text{HH}}\frac{\partial c_{\text{H}}}{\partial y} \tag{3.18}$$

in which the matrix of transport coefficients relates to the Fickian diffusion coefficients through

$$\begin{bmatrix} L_{\text{VV}} & L_{\text{VH}} \\ L_{\text{HV}} & L_{\text{HH}} \end{bmatrix} = \frac{c_{\text{T}}}{c_{\text{m}}\left(1 + \frac{c_{\text{V}}\mathscr{D}_{\text{Hm}}}{c_{\text{m}}\mathscr{D}_{\text{HV}}} + \frac{c_{\text{H}}\mathscr{D}_{\text{Vm}}}{c_{\text{m}}\mathscr{D}_{\text{VH}}}\right)} \begin{bmatrix} \mathscr{D}_{\text{Vm}}\left(1 + \frac{c_{\text{V}}\mathscr{D}_{\text{Hm}}}{c_{\text{m}}\mathscr{D}_{\text{HV}}}\right) & \frac{c_{\text{V}}\mathscr{D}_{\text{Hm}}\mathscr{D}_{\text{Vm}}}{c_{\text{m}}\mathscr{D}_{\text{VH}}} \\ \frac{c_{\text{H}}\mathscr{D}_{\text{Hm}}\mathscr{D}_{\text{Vm}}}{c_{\text{m}}\mathscr{D}_{\text{HV}}} & \mathscr{D}_{\text{Hm}}\left(1 + \frac{c_{\text{H}}\mathscr{D}_{\text{Vm}}}{c_{\text{m}}\mathscr{D}_{\text{VH}}}\right) \end{bmatrix}. \tag{3.19}$$

To model experimental conditions for interdiffusion experiments, equations 3.2, 3.3, and 3.19, subject to boundary conditions 3.4, were solved with initial conditions

$$\begin{bmatrix} c_{\mathrm{V}}^{1}(0) \\ c_{\mathrm{H}}^{1}(0) \end{bmatrix} = \begin{bmatrix} 0 \\ c_0 \end{bmatrix}, \begin{bmatrix} c_{\mathrm{V}}^{2}(0) \\ c_{\mathrm{H}}^{2}(0) \end{bmatrix} = \begin{bmatrix} c_0 \\ 0 \end{bmatrix}, \text{ and}$$

$$\begin{bmatrix} c_{\mathrm{V}}^{\mathrm{m}}(0,x) \\ c_{\mathrm{H}}^{\mathrm{m}}(0,x) \end{bmatrix} = \begin{bmatrix} K_{\mathrm{V}} & \beta c_{\mathrm{V}} \\ \beta c_{\mathrm{H}} & K_{\mathrm{H}} \end{bmatrix} \times \begin{bmatrix} c_0/2 \\ c_0/2 \end{bmatrix}. \quad (3.20)$$

These equations say that the separator begins the experiment equilibrated with a solution of aqueous H_2SO_4 and $VOSO_4$ each at a concentration of $c_0/2$ (combined concentration c_0); that chamber 1 initially contains aqueous H_2SO_4 at concentration c_0; and that chamber 2 initially contains aqueous $VOSO_4$ at concentration c_0. Comsol multi physics PDE solver was used to solve the governing system.

For simplicity, data analysis was performed under the assumption that $D_{\mathrm{HV}} = D_{\mathrm{VH}}$, so that $L_{\mathrm{VH}}/c_{\mathrm{V}} = L_{\mathrm{HV}}/c_{\mathrm{H}}$, although strictly speaking, a truly symmetric Onsager reciprocal relation only applies to the Stefan-Maxwell diffusivities, $\mathscr{D}_{\mathrm{VH}} = \mathscr{D}_{\mathrm{HV}}$.[47,48] Taking the **L** matrix in equation 3.19 to be symmetric amounts to an assumption that the Darken thermodynamic factors are of similar order for both $VOSO_4$ and H_2SO_4.

Values of solute-solute interaction parameters were obtained by fitting the results of the Comsol simulation to experimental conductimetric measurements of the transient solute concentrations in both dialysis-cell chambers. To perform the fitting, the partition coefficients K_{V} and K_{H}, and the Fickian diffusivities D_{Vm} and D_{Hm}, were assumed to be the same as they were in the binary experiments. Then, under the assumption that $D_{\mathrm{HV}} = D_{\mathrm{VH}}$, the parameters D_{VH} and β were varied to minimize the residuals in a fit of long-time relaxation data. The second law requires the **L** matrix defined in equation 3.19 to be positive-definite, a condition that bounds the values of the solute-solute diffusivity. The range of physical values for D_{VH} was explored to find the value that fit the data within experimental error at long times.

3.3 Experimental Results

Figure 3.5 shows typical binary diffusion measurements for aqueous $VOSO_4$ and H_2SO_4 in Celgard.

For binary diffusion measurements, the regime of exponential relaxation was reached several seconds after the experiment began. The relaxation constants L_{Vm}, L_{Hm} and partition coefficients K_{V}, K_{H} for Celgard were calculated using the dialysis-cell data from the first three hours of relaxation. Additional data was gathered for cells where H_2SO_4 was

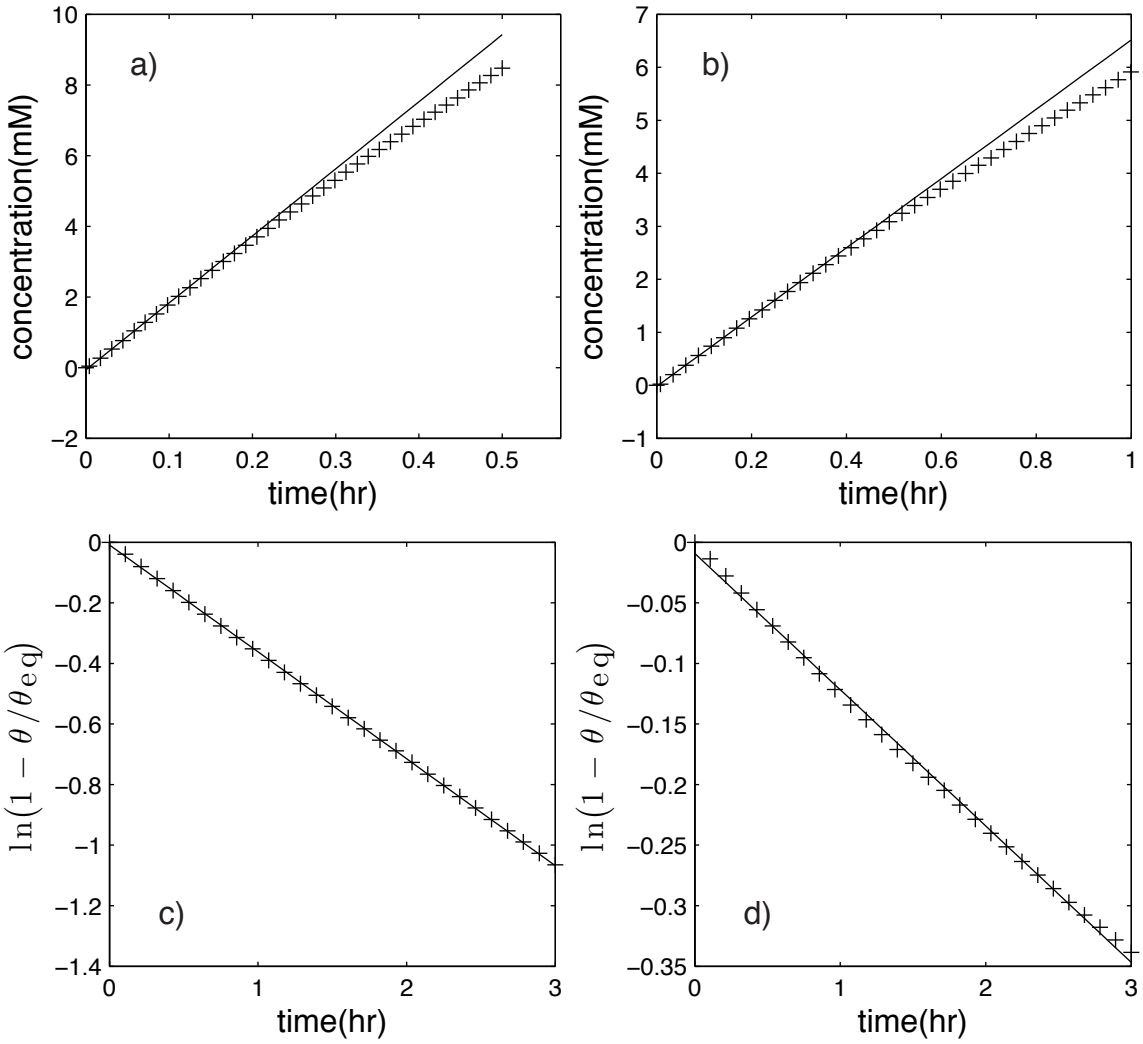

Figure 3.5: Relaxation data for binary diffusion of H_2SO_4 (left) and $VOSO_4$ (right) through Celgard at ambient temperature. a), b) Short-time measurements of the concentration on the unloaded side of the dialysis cell, showing the fit used to measure the onset time. c), d) Data from the first three hours of relaxation, showing that exponential relaxation occurs shortly after the start of the experiment.

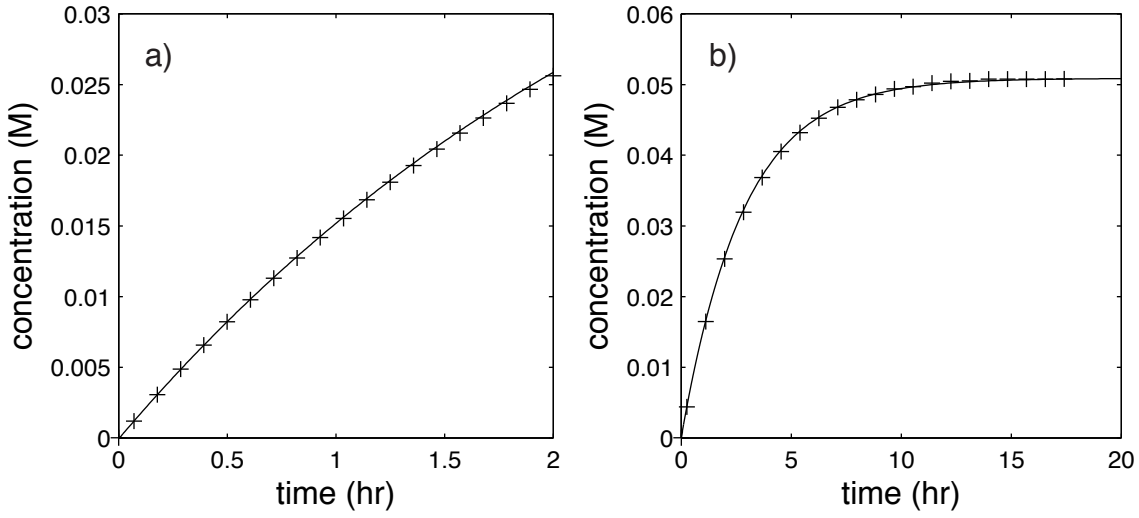

Figure 3.6: Model fits for H_2SO_4 diffusion through Celgard for a) the first 2 hours and b) over the entire concentration relaxation show that the diffusion and partition coefficients measured from the first few hours are predictive of the entire relaxation.

diffusing Figure 3.6 shows the excellent fit over the entire relaxation, predicted by the parameters that were measured in the first three hours, suggesting the assumption of linear response (constancy of L_{ij} and K_i) is reasonable for these systems.

Identical measurements were performed using a Nafion membrane. Figure 3.7 shows the analogous plots for $VOSO_4$ and H_2SO_4 diffusing through Nafion. Two distinct slopes appear in the log plot of concentration vs. time for $VOSO_4$ diffusing through Nafion, suggesting there is some physical process not included in the previously described model. The Comsol model was used to probe several plausible scenarios to test their consistentcy with the observed response. These scenarios included; some concentration of H_2SO_4 or $VOSO_4$ left over in the membrane leeching out at the beginning of the experiment, or H_2SO_4 created from the equilibration of aqueous vanadyl sulfate with water crossing the membrane concurrently with $VOSO_4$. None of these scenarios produced a set of parameters consistent with all the available experimental data. For this reason only the values of the partition coefficient and diffusion coefficient of H_2SO_4 will be reported; $D_{\mathrm{Hm}} = 1.6 \times 10^{-10} \mathrm{cm}^2\mathrm{s}^{-1}$, $K_{\mathrm{H}} = 0.11$

Results of conductimetric interdiffusion experiments with Nafion and Celgard membranes are shown in figure 3.8, in comparison to the best fits from the multicomponent diffusion simulation.

The transient composition curves in Figures 3.5 and 3.8 allowed for the parameterization of the transport model for Celgard. Values for the six transport parameters are given in

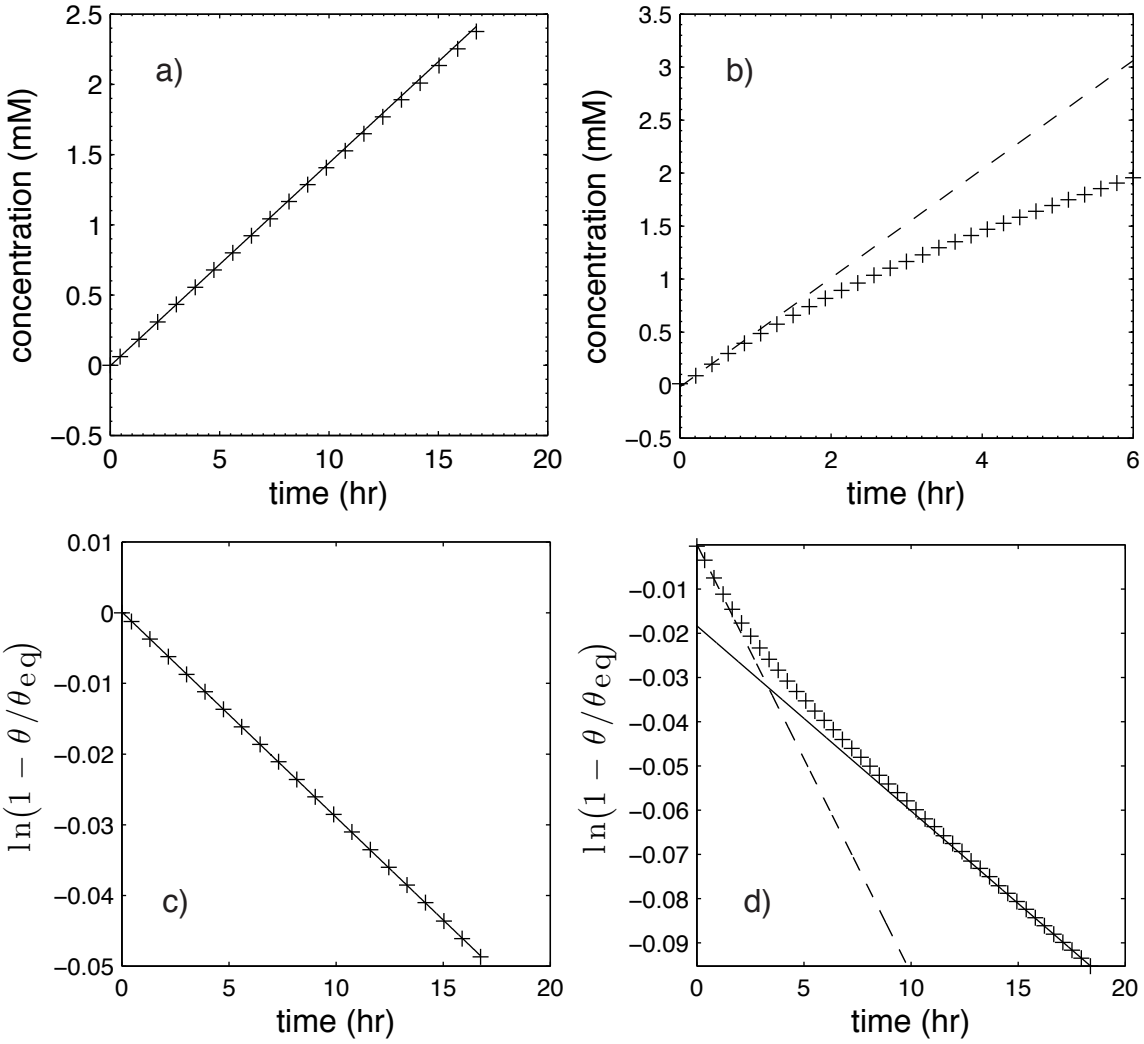

Figure 3.7: Comparison of transient concentration profiles to the theory for a) H_2SO_4 and b) $VOSO_4$ diffusing through Nafion. Two distinct slopes for the $VOSO_4$ indicate processes not accounted for in the model.

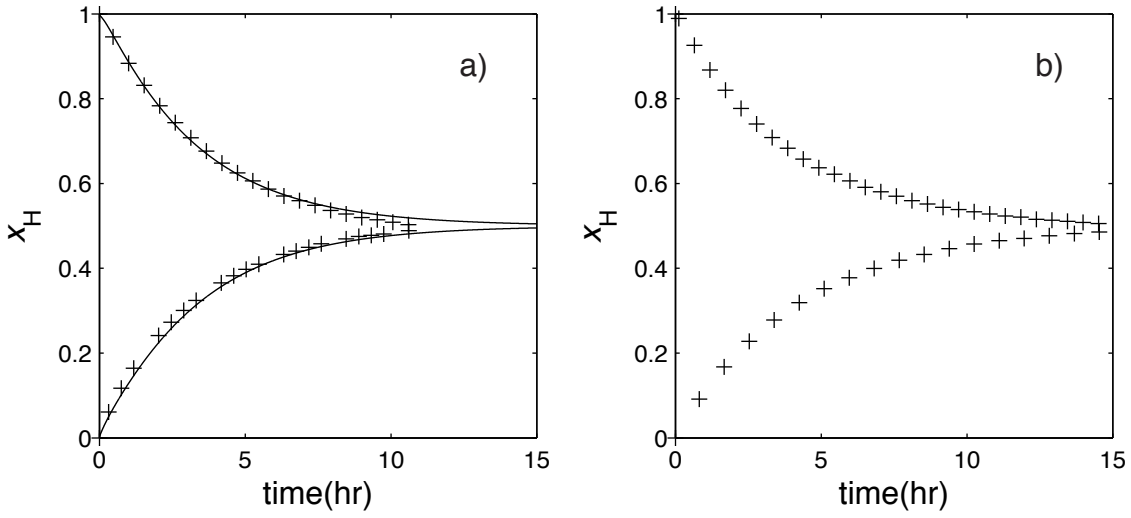

Figure 3.8: Interdiffusion experiments for a) Celgard and b) Nafion reach equilibrium over similar timescales. Experimental data are represented by x and the line in a) represents the fitted model result

Table 3.1: Partition coefficient and diffusion coefficient for $VOSO_4$ and H_2SO_4 in celgard

D_{Vm} cm^{2}s^{-1}	K_{V}	D_{Hm} cm^{2}s^{-1}	K_{H}	D_{HV} cm^{2}s^{-1}	β
$2.1 \pm 0.2e-7$	1.31 ± 0.06	$2.2 \pm 0.6e-7$	5 ± 1	$-1.5e-11$	0.71

Table 3.1. Individual curves were fit very well by each parameter, and the associated errors in Table 3.1 comes from extracting values from multiple curves.

3.4 Discussion

Comparison of the binary results for Celgard shows that H_2SO_4 and $VOSO_4$ have similar diffusion coefficients. The significance of this similarity can be interpreted considered through the understanding of diffusion provided by the Stokes-Einstein relation, where k_B is Boltzmann's constant

$$D = \frac{k_B T}{6\pi\eta r}. \tag{3.21}$$

Both species are moving through water with viscosity η at temperature T, so their similar diffusion coefficients suggests their effective atomic radii are also similar. This supports the prediction from charge neutrality that both H_2SO_4 and $VOSO_4$ diffuse in neutral com-

bination. It also suggests their effective atomic radii are dominated by SO_4^{-2}, since VO^{2+} is much larger than two H^+ ions.

The partition coefficients and β value for H_2SO_4 and $VOSO_4$ in Celgard provide insight into the thermodynamics in the membrane. Partition coefficients for both species in Celgard are larger than 1 meaning that the concentration in the membrane is higher than in the adjacent solution. Celgard is normally hydrophobic, and has to be coated with a surfactant for aqueous applications. The presence of the surfactant on the high surface area of the membrane could stabilize ionic species in the membrane leading to a partition coefficient higher than one. The positive value of the β parameter suggests that the presence of either electrolyte stabilizes the presence of the other, similar to the salting in effect that has been observed for pairs of solutes. This suggests a significant interaction between the two that will also manifest itself in the interaction parameter D_{HV}.

The measured value of D_{HV} is comparable in magnitude to the binary diffusion coefficients and negative. It was mentioned in the theory section that this work was done in a way to ensure the parameters obtained would be thermodynamically consistent. This leaves the question of the interpretation of a negative value. Since diffusion coefficients represent a conductance, very small values can be thought of as representing a high resistance. Keeping this in mind, it is actually more intuitive to consider the impact of the resistance to transport that one species exerts on the other $1/D_{\mathrm{HV}}$. When the resistance is small compared to the resistance through the diffusion medium ($|D_{\mathrm{HV}}| >> D_i\mathrm{m}$) there is negligible impact on transport. Only when the resistance is high compared to the resistance imposed by the diffusion medium ($|D_{\mathrm{HV}}| << D_i\mathrm{m}$) will the effect on transport be apparent. The sign of the parameter indicates the effect a gradient in concentration of one species will have on the flux of another. A negative value simply means there is a driving force for one species to travel up the concentration gradient of another. This is consistent with the salting in effect that was observed from the β parameter in the membrane. Figure 3.9 shows model results for given values of D_{HV}.

Despite being unable to provide quantitative measurements for Nafion, it is worth noting that the time for the completion of the interdiffusion experiments for Nafion is similar to that of Celgard, despite its thickness being nearly ten times that of Celgard. For a given substance, a tenfold increase in thickness would result in a hundredfold increase in the time required to reach equilibrium. This suggests that Celgard may inhibit the cross diffusion of vanadyl species in the presence of acid more strongly than Nafion, so in addition to the capital cost benefit to using Celgard (it is much cheaper than Nafion) there may also be an operating cost benefit due to less frequent electrolyte regeneration from lower crossover rates in Celgard than Nafion. If a Celgard separator thin enough to match the high conduc-

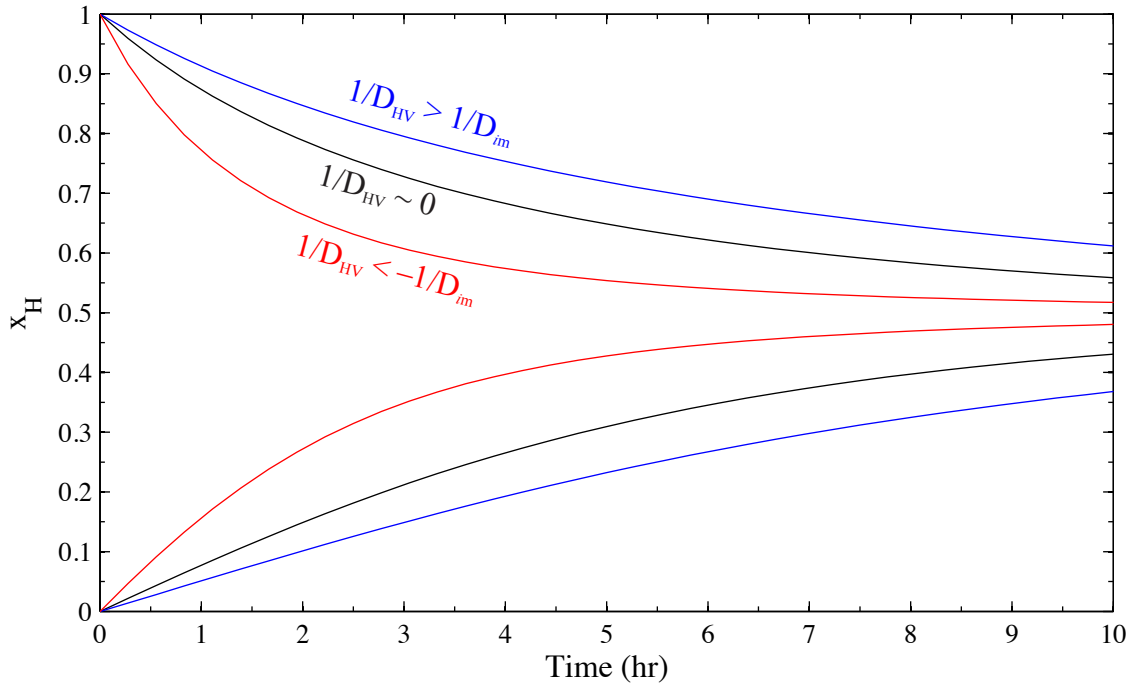

Figure 3.9: Looking at the top 3 curves representing the initially pure H_2SO_4 side in a simulated interdiffusion experiment: the top curve shows that when D_{HV} is positive and small, it slows the interdiffusion of the two species; the middle curve shows that when D_{HV} is large and positive or negative, it has little effect on diffusion; the bottom curve shows that when D_{HV} is negative and small it can speed up interdiffusion.

tivity of Nafion is able to withstand the mechanical requirements of use if a flow battery, Celgard could provide a very attractive alternative to Nafion.

CHAPTER 4

Effect of Oxygen Transport on Cell Voltages of Lithium/Oxygen Batteries

4.1 Introduction

There is reason to believe that diffusion potentials from oxygen exist in some metal/oxygen batteries. Experiments with aprotic Li/O_2 cells, for example, typically require a preconditioning interval, during which the system is held at open circuit while being exposed to oxygen at fixed pressure until the cell voltage equilibrates[10,49–51]. During preconditioning, which can last for hours[10,50,51], the open-circuit potential can vary across tens or hundreds of millivolts. It is likely that some part of this variation arises from a diffusion potential: since salt flux is negligible and the interfacial kinetics of oxygen absorption is probably fast, relaxation of the oxygen distribution inside the cell could be the source of the slow voltage change. This hypothesis is supported by the observation that far shorter preconditioning is needed when Li/O_2 cells are thinner[49].

A standard liquid electrolyte for a metal/oxygen battery is made up of a neutral solvent, dissolved oxygen, and a salt with a single type of anion and a single type of cation. Given that four electrochemical species comprise these electrolytes, one expects on the basis of the Onsager mass-transport theory[43] that six independent transport coefficients are needed to describe all the possible pairwise interactions associated with diffusion and migration. Most state-of-the-art models of metal/oxygen-battery electrolytes[52–56] only include four of the six properties that thermodynamic completeness requires: oxygen diffusivity, electrolyte diffusivity, ionic conductivity, and cation transference number.

Onsager-Stefan-Maxwell constitutive laws contain the six properties needed to ensure a proper accounting of dynamic energy dissipation. Flux laws in Nernst-Planck form (describing the excess fluxes of oxygen, cations, and anions relative to solvent explicitly, using terms that distinguish the impacts of individual diffusion and migration driving forces) can be derived by inverting the Onsager-Stefan-Maxwell equations. This flux-law inversion

process suggests natural definitions for two additional transport properties: an 'electro-osmotic drag coefficient', which determines how the flow of ionic current can drive oxygen flux, and a 'cross-diffusion coefficient', which quantifies how salt gradients drive oxygen flux (and how oxygen gradients drive salt flux). The inversion procedure also yields a 'MacInnes equation' (extended form of Ohm's law[22,57]), showing how electro-osmotic drag can manifest a diffusion potential associated with oxygen gradients.

The theory is applied to experimental preconditioning data from lithium/oxygen cells to develop a first measurement of the electro-osmotic drag coefficient for oxygen in an electrolyte comprising 1 M LiTFSI in DME under oxygen at 14 psig. Experiments suggest that significant overpotential can arise from non-uniform oxygen distributions in Li/O_2 batteries—a factor that may significantly impact performance during high-rate operation.[52]

4.2 Macroscopic Transport Properties

Both a MacInnes equation and flux laws in Nernst-Planck form can be derived directly from the Onsager-Stefan-Maxwell equations by a sequence of linear transformations. A general implementation of this process, which shows how to identify and count independent macroscopic transport properties for multicomponent electrochemical systems, was presented by Monroe and Delacourt[58].

According to the procedure, a formulation of thermodynamically complete multicomponent transport laws in Nernst-Planck form begins with the arrangement of species indices in an ordered list. (In this context, 'thermodynamically complete' means that the flux laws incorporate all the possible sources of energy dissipation identified from a local entropy balance.) Let indices $\{0, o, -, +\}$ indicate the neutral-solvent, oxygen, anion, and cation species, respectively. Placement of cations in the last position identifies them as the sole charged species whose electrochemical potential will appear in the MacInnes equation that emerges from the Onsager-Stefan-Maxwell laws. This choice is natural in the present context because cations are generally produced and consumed at the negative electrodes of metal/oxygen batteries, and reference electrodes reversible to cations are typically used in experiments.

The general treatment of electrochemical flux-law inversion allows electroneutrality to be relaxed if needed[58]. For most applications, however, it is suitable to assume local electroneutrality,

$$F \sum_i z_i c_i \approx 0. \tag{4.1}$$

Here F is Faraday's constant, and z_i and c_i respectively represent the equivalent charge and local molar concentration of species i. Since the stoichiometric coefficents ν_i in a salt formula unit relate through the Guggenheim condition $z_+\nu_+ + z_-\nu_- = 0$, electroneutrality allows one to write both of the ion concentrations in terms of an electrolyte concentration c_e: $c_\mathrm{e} = c_+/\nu_+ = c_-/\nu_-$. The number of ions in a salt formula unit is written as ν_e: $\nu_\mathrm{e} = \nu_+ + \nu_-$.

Onsager-Stefan-Maxwell equations describing multicomponent transport in isothermal, isobaric phases are expressed in terms of electrochemical-potential-gradient diffusion driving forces as

$$-c_i\vec{\nabla}\mu_i = \frac{RT}{c_\mathrm{T}}\sum_{j\neq i}\frac{c_j\vec{N}_i - c_i\vec{N}_j}{\mathscr{D}_{ij}}, \tag{4.2}$$

in which R is the gas constant, T the absolute temperature, $c_\mathrm{T} = \sum_i c_i = c_0 + c_\mathrm{o} + \nu_\mathrm{e}c_\mathrm{e}$ is the total molar concentration of the solution, $\vec{N}_i$ is the total molar flux of species i, and $\mathscr{D}_{ij}$ is the Stefan-Maxwell diffusivity of species i through species j. Onsager reciprocal relations require the symmetry $\mathscr{D}_{ij} = \mathscr{D}_{ji}$, so equations 4.2 only contain $4\cdot(4-1)/2 = 6$ distinct transport coefficients.

Since the oxygen and solvent species are uncharged, the Stefan-Maxwell diffusivity of oxygen through solvent, $\mathscr{D}_{\mathrm{o}0}$, can be readily understood from a macroscopic point of view. (It can be approximated as equaling the thermodynamic diffusivity of oxygen through solvent, measured in the absence of salt.) When recasting equations 4.2 in the Nernst-Planck form it will be convenient to exchange the other Stefan-Maxwell diffusivities for similarly tangible properties.

In the concentrated-solution theory for binary electrolytes[22], the thermodynamic diffusion coefficient of electrolyte through solvent, $\mathscr{D}_{\mathrm{e}0}$, and the cation transference number relative to solvent, $t^0_{+\mathrm{o}}$, are defined in terms of Stefan-Maxwell diffusivities as

$$\mathscr{D}_{\mathrm{e}0} = \frac{(z_+ - z_-)\,\mathscr{D}_{0+}\mathscr{D}_{0-}}{z_+\mathscr{D}_{0+} - z_-\mathscr{D}_{0-}} \quad \text{and} \quad t^0_{+\mathrm{o}} = \frac{z_+\mathscr{D}_{0+}}{z_+\mathscr{D}_{0+} - z_-\mathscr{D}_{0-}}. \tag{4.3}$$

For an electrolytic solution that also contains dissolved oxygen, the definition of the cation transference number differs somewhat from the familiar form in equation 4.3. Thus a subscript o is added to $t^0_{+\mathrm{o}}$ here, to emphasize that it represents 'the cation transference number relative to solvent, as defined in the absence of oxygen.' The ionic conductivity as defined in the absence of oxygen, κ_o, is

$$\frac{1}{\kappa_\mathrm{o}} = -\frac{RT}{c_\mathrm{T}F^2z_+z_-}\left[\frac{1}{\mathscr{D}_{+-}} - \frac{z_-c_0}{\nu_+c_\mathrm{e}\,(z_+\mathscr{D}_{0+} - z_-\mathscr{D}_{0-})}\right]. \tag{4.4}$$

Values of $\mathscr{D}_{e0}$, t^0_{+o}, and κ_o measured in oxygen-free liquid electrolytes can be used to estimate $\mathscr{D}_{0+}$, $\mathscr{D}_{0-}$, and $\mathscr{D}_{+-}$.

By analogy to t^0_{+o} and $\mathscr{D}_{e0}$, it is helpful to identify a cation transference number relative to oxygen as defined in the absence of solvent, t^o_{+0}, and a thermodynamic diffusivity of electrolyte through oxygen, $\mathscr{D}_{eo}$,

$$t^o_{+0} = \frac{z_+ \mathscr{D}_{o+}}{z_+ \mathscr{D}_{o+} - z_- \mathscr{D}_{o-}} \quad \text{and} \quad \mathscr{D}_{eo} = \frac{(z_+ - z_-)\, \mathscr{D}_{o+} \mathscr{D}_{o-}}{z_+ \mathscr{D}_{o+} - z_- \mathscr{D}_{o-}}. \tag{4.5}$$

It is probably not possible to implement a binary oxygen/salt solution, but these definitions provide notational convenience.

If the cation transference number relative to solvent differs from the cation transference number relative to oxygen (*i.e.*, if $t^0_{+o} \neq t^o_{+0}$), ion fluxes induced by an electric field can exert drag forces on oxygen that differ from the drag forces the ion fluxes exert on solvent, inducing a flux of oxygen relative to solvent. These differences in the impact of migration can be understood as an electro-osmotic effect, similar to the phenomenon that drives water transport across polarized ionomer membranes in fuel cells[59]. The magnitude of $1/\mathscr{D}_{eo}$ relative to $1/\mathscr{D}_{e0}$ also quantifies the significance of the electro-osmotic drag force on oxygen.

Six macroscopic coefficients can ultimately be identified in the flux-explicit transport laws. Four are typical.

1. Thermodynamic electrolyte diffusivity:

$$\mathscr{D}_e = \frac{\mathscr{D}_{e0}\,(c_0 \mathscr{D}_{eo} + \nu_e c_e \mathscr{D}_{o0})}{c_0 \mathscr{D}_{eo} + \nu_e c_e \mathscr{D}_{o0} + c_o \mathscr{D}_{e0}}. \tag{4.6}$$

2. Thermodynamic oxygen diffusivity:

$$\mathscr{D}_o = \frac{\mathscr{D}_{o0}\,(c_0 \mathscr{D}_{eo} + c_o \mathscr{D}_{e0})}{c_0 \mathscr{D}_{eo} + \nu_e c_e \mathscr{D}_{o0} + c_o \mathscr{D}_{e0}}. \tag{4.7}$$

3. Cation transference number:

$$t^0_+ = \frac{(c_0 \mathscr{D}_{eo} + \nu_e c_e \mathscr{D}_{o0})\, t^0_{+o} + c_o \mathscr{D}_{e0} t^o_{+0}}{c_0 \mathscr{D}_{eo} + \nu_e c_e \mathscr{D}_{o0} + c_o \mathscr{D}_{e0}}. \tag{4.8}$$

4. Ionic conductivity:

$$\frac{1}{\kappa} = \frac{1}{\kappa_\mathrm{o}} + \frac{\nu_\mathrm{e} c_\mathrm{o} RT}{F^2 z_+^2 \nu_+^2 c_\mathrm{e} c_\mathrm{T} \mathscr{D}_\mathrm{eo}} \times \left[t_{+0}^\mathrm{o} \left(1 - t_{+0}^\mathrm{o}\right) + \frac{c_0 \mathscr{D}_\mathrm{e0} \left(t_{+\mathrm{o}}^0 - t_{+0}^\mathrm{o}\right)^2}{c_0 \mathscr{D}_\mathrm{eo} + \nu_\mathrm{e} c_\mathrm{e} \mathscr{D}_\mathrm{o0} + c_\mathrm{o} \mathscr{D}_\mathrm{e0}} \right]. \quad (4.9)$$

Two properties arise that are not usually considered.

5. Electro-osmotic coefficient:

$$\Xi = \frac{c_\mathrm{o} \mathscr{D}_\mathrm{o0} \left(t_{+\mathrm{o}}^0 - t_{+0}^\mathrm{o}\right)}{c_0 \mathscr{D}_\mathrm{eo} + \nu_\mathrm{e} c_\mathrm{e} \mathscr{D}_\mathrm{o0} + c_\mathrm{o} \mathscr{D}_\mathrm{e0}}. \quad (4.10)$$

6. Cross diffusivity:

$$\mathscr{X}_\mathrm{eo} = \frac{c_\mathrm{T} \mathscr{D}_\mathrm{e0} \mathscr{D}_\mathrm{o0}}{c_0 \mathscr{D}_\mathrm{eo} + \nu_\mathrm{e} c_\mathrm{e} \mathscr{D}_\mathrm{o0}}. \quad (4.11)$$

Since this is a four-species electrolyte, it naturally affords one ionic conductivity (κ), two dimensionless transport numbers (t_+^0 and Ξ), and three diffusivities ($\mathscr{D}_\mathrm{e}$, $\mathscr{D}_\mathrm{o}$, and $\mathscr{X}_\mathrm{eo}$). An anion transference number is identified by noting that $t_0^0 = 0$ because the solvent velocity is the reference for convection, $t_\mathrm{o}^0 = 0$ because both oxygen and solvent are uncharged, and $\sum_i t_i^0 = 1$ for consistency with Faraday's law, so $t_-^0 = 1 - t_+^0$ [58]. Equations 4.6 through 4.11 can be inverted to express the Stefan-Maxwell coefficients as explicit functions of κ, t_+^0, Ξ, $\mathscr{D}_\mathrm{e}$, $\mathscr{D}_\mathrm{o}$, and $\mathscr{X}_\mathrm{eo}$, as well.

4.3 Transport laws for air-battery electrolytes

Implementation of the inversion procedure and insertion of the properties defined in equations 4.6 through 4.11 result in a MacInnes equation involving oxygen gradients,

$$\vec{i} = -\frac{\kappa}{F z_+} \vec{\nabla} \mu_+ + \frac{\left(1 - t_+^0\right) \kappa}{F z_+ \nu_+} \vec{\nabla} \mu_\mathrm{e} + \frac{(z_+ - z_-) \Xi \kappa}{F z_+ z_-} \vec{\nabla} \mu_\mathrm{o}. \quad (4.12)$$

To arrive at this result the isothermal, isobaric, electroneutral Gibbs-Duhem equation

$$c_0 \vec{\nabla} \mu_0 + c_\mathrm{o} \vec{\nabla} \mu_\mathrm{o} + c_\mathrm{e} \vec{\nabla} \mu_\mathrm{e} = 0 \quad (4.13)$$

has been used, in which $\mu_\mathrm{e} = \nu_+ \mu_+ + \nu_- \mu_-$. The inversion process further yields equations in Nernst-Planck form that describe the excess fluxes of oxygen, anions, and cations:

$$\vec{N}_\mathrm{o} - c_\mathrm{o}\vec{v}_0 = \frac{\mathscr{X}_\mathrm{eo}c_\mathrm{o}}{c_\mathrm{T}}\vec{d}_\mathrm{e} + \mathscr{D}_\mathrm{o}\vec{d}_\mathrm{o} - \frac{(z_+ - z_-)\,\Xi}{Fz_+z_-}\vec{i}, \tag{4.14}$$

$$\vec{N}_- - c_-\vec{v}_0 = \mathscr{D}_\mathrm{e}\nu_-\vec{d}_\mathrm{e} + \frac{\mathscr{X}_\mathrm{eo}c_-}{c_\mathrm{T}}\vec{d}_\mathrm{o} + \frac{\left(1 - t_+^0\right)}{Fz_-}\vec{i}, \tag{4.15}$$

$$\vec{N}_+ - c_+\vec{v}_0 = \mathscr{D}_\mathrm{e}\nu_+\vec{d}_\mathrm{e} + \frac{\mathscr{X}_\mathrm{eo}c_+}{c_\mathrm{T}}\vec{d}_\mathrm{o} + \frac{t_+^0}{Fz_+}\vec{i}. \tag{4.16}$$

Here the current density $\vec{i}$ is taken to drive migration and the solvent velocity $\vec{v}_0 = \vec{N}_0/c_0$ drives convection; forces driving diffusion of the two neutral-solute components, $\vec{d}_\mathrm{e}$ and $\vec{d}_\mathrm{o}$, appear:

$$\vec{d}_\mathrm{e} = -\frac{c_\mathrm{T}c_\mathrm{e}\vec{\nabla}\mu_\mathrm{e}}{c_0\nu_\mathrm{e}RT} \quad \text{and} \quad \vec{d}_\mathrm{o} = -\frac{c_\mathrm{T}c_\mathrm{o}\vec{\nabla}\mu_\mathrm{o}}{c_0RT}. \tag{4.17}$$

Note that $\vec{d}_i$ has units of molar-concentration gradient.

Under isothermal, isobaric conditions, the Gibbs phase rule requires that the component chemical potentials depend at most on c_e and c_o. Thus the thermodynamic driving forces can be expressed as linear combinations of $\vec{\nabla}c_\mathrm{e}$ and $\vec{\nabla}c_\mathrm{o}$, through thermodynamic factors $\chi_{ij}(c_\mathrm{e}, c_\mathrm{o})$,

$$\begin{aligned}\vec{d}_\mathrm{e} &= -\chi_\mathrm{ee}\vec{\nabla}c_\mathrm{e} - \chi_\mathrm{eo}\vec{\nabla}c_\mathrm{o},\\ \vec{d}_\mathrm{o} &= -\chi_\mathrm{oe}\vec{\nabla}c_\mathrm{e} - \chi_\mathrm{oo}\vec{\nabla}c_\mathrm{o}.\end{aligned} \tag{4.18}$$

Assuming standard constitutive laws[60,61]

$$\begin{aligned}\mu_\mathrm{e}(T,p,c_\mathrm{e},c_\mathrm{o}) &= \mu_\mathrm{e}^\theta(T,p) + \nu_\mathrm{e}RT\ln(f_\mathrm{e}c_\mathrm{e}),\\ \mu_\mathrm{o}(T,p,c_\mathrm{e},c_\mathrm{o}) &= \mu_\mathrm{o}^\theta(T,p) + RT\ln(f_\mathrm{o}c_\mathrm{o}),\end{aligned} \tag{4.19}$$

where μ_i^θ is the chemical potential in a primary reference state, f_e is the mean molar activity coefficient of the electrolyte, and f_o is the activity coefficient of oxygen on a molar basis, one can write

$$\chi_{ij} = \frac{c_\mathrm{T}}{c_0}\left[\delta_{ij} + c_i\left(\frac{\partial \ln f_i}{\partial c_j}\right)_{T,p,c_{k\neq j}}\right], \tag{4.20}$$

in which δ_{ij} is the Kronecker delta. For an ideal neutral component i, f_i is independent of composition; in the limit of infinite dilution, $c_\mathrm{T} \approx c_0$. Thus the force driving mass transport of neutral-solute component i in an ideal, dilute air-battery electrolyte is $\vec{d}_i \approx -\vec{\nabla}c_i$.

4.4 Consequences of ion/oxygen interactions

Existing models of air-battery electrolytes tend to use the equations from Nernst-Planck theory or the theory of concentrated binary electrolytes to describe the ion fluxes, and additionally adopt Fick's law to describe the oxygen flux. This theoretical structure is (uniquely) achieved by taking Ξ and $\mathscr{X}_{\mathrm{eo}}$ to vanish in equations 4.12 and 4.14–4.16, leaving a theory with four transport coefficients.

Given a system in which the species concentrations are all finite, the conditions $\mathscr{X}_{\mathrm{eo}} \to 0$ and $\Xi \to 0$ imply through equations 4.31 and 4.32 that $1/\mathscr{D}_{\mathrm{o}+} \to 0$ and $1/\mathscr{D}_{\mathrm{o}-} \to 0$; conversely, the conditions $1/\mathscr{D}_{\mathrm{o}+} \to 0$ and $1/\mathscr{D}_{\mathrm{o}-} \to 0$ imply through equations 4.5, 4.10, and 4.11 that $\Xi \to 0$ and $\mathscr{X}_{\mathrm{eo}} \to 0$. Thus the electro-osmotic coefficient and cross-diffusivity vanish if and only if the Stefan-Maxwell diffusional resistances associated with microscopic ion/oxygen interactions vanish. Prior models thus result from neglecting drag forces that ion fluxes could exert on oxygen.

In all known air-battery electrolytes, the maximum oxygen concentration is extremely small in comparison to the concentrations of both salt and solvent[62], which is a limit worth exploring. In this case one is not justified in neglecting the cross-diffusion terms in equations 4.15 and 4.16; although $\|\vec{d}_{\mathrm{o}}\| \sim \|\vec{\nabla} c_{\mathrm{o}}\|$, the fact that $c_{\mathrm{o}} << c_{\mathrm{e}}$ does not require that $\|\vec{\nabla} c_{\mathrm{o}}\| << \|\vec{\nabla} c_{\mathrm{e}}\|$. (Indeed, at the beginning of preconditioning, $\|\vec{\nabla} c_{\mathrm{e}}\| \approx 0$, while the oxygen gradient can be very large.) Since $\Xi \propto c_{\mathrm{o}}$, the molar electro-osmotic coefficient $\tilde{\Xi}$,

$$\tilde{\Xi} = \frac{\Xi c_{\mathrm{T}}}{c_{\mathrm{o}}}, \tag{4.21}$$

remains finite as $c_{\mathrm{o}} \to 0$ if the Stefan-Maxwell diffusivities are all finite. Incorporation of $\tilde{\Xi}$ into the oxygen flux law (equation 4.14) shows that the $\vec{d}_{\mathrm{e}}$, $\vec{d}_{\mathrm{o}}$, and $\vec{i}$ terms are all of $O(c_{\mathrm{o}})$; no term can be neglected in favor of the others on the grounds that c_{o} is small.

It is thermodynamically inconsistent to incorporate a concentration overpotential associated with oxygen gradients (such as the $\vec{\nabla}\mu_{\mathrm{o}}$ term in equation 4.12) without placing a corresponding migration term in the oxygen flux law (such as the $\vec{i}$ term in equation 4.14). Significant modification of all the transport laws may be needed to account for how the oxygen distribution affects cell potential.

Assuming that a reference electrode reversible to cations only is used to measure the voltage drop across the cell interior (so that $\vec{\nabla}\mu_{+} = F z_{+} \vec{\nabla}\Phi$), equation 4.12 yields a law that governs the change in electrode potential Φ,

$$-\vec{\nabla}\Phi = \frac{\vec{i}}{\kappa} + \frac{RTc_0}{Fz_{+}c_{\mathrm{T}}c_{\mathrm{e}}}\left[\left(1 - t_{+}^{0}\right)\frac{\nu_{\mathrm{e}}}{\nu_{+}}\vec{d}_{\mathrm{e}} - \tilde{\Xi}\frac{c_{\mathrm{e}}}{c_{\mathrm{T}}}\vec{d}_{\mathrm{o}}\right]. \tag{4.22}$$

The term with $\vec{d}_o$ scales as $\vec{\nabla} c_o$. Thus large oxygen gradients could induce an electric field—even if c_o is very low.

4.5 Analysis of metal/oxygen cell preconditioning

Equation 4.22 can be used to rationalize the voltage response observed during a standard preconditioning experiment — formally, an open-circuit hold of a planar air-battery cell initially equilibrated under an inert gas, whose atmosphere undergoes a sudden change from inert gas to fixed-pressure oxygen at time $t = 0$. The current vanishes (so $\vec{i} = \vec{0}$), and electrolyte gradients are negligible (so $\vec{d}_e \approx \vec{0}$ and $c_e \approx$ constant). Since the oxygen concentration is very small, c_T and c_0 are both relatively constant when c_e is. Assuming $f_o \approx 1$ (oxygen is an ideal solute), a thermodynamic analysis of the cell reaction, accompanied by integration of equation 4.22 under the assumption that $\tilde{\Xi}$ is relatively constant in the limit of low oxygen concentration, yields an expression for the instantaneous open-circuit cell potential, $\Delta\Phi$. Defining $\Delta\Phi$ as the voltage drop from the positive to the negative electrode, one finds a relationship in terms of the difference in oxygen concentration across the cell,

$$\Delta\Phi = \frac{RT\nu_e\tilde{\Xi}}{Fz_+\nu_+c_T}\left(c_o|_- - c_o|_+\right) + U^\theta. \tag{4.23}$$

Here $c_o|_-$ is the oxygen concentration in the liquid adjacent to the negative-electrode surface, and $c_o|_+$ is its liquid-phase concentration adjacent to the interface with ambient gas; U^θ is the equilibrium potential of the cell reaction that would be observed if the oxygen concentration throughout the cell were equilibrated at $c_o|_+$. Thus oxygen gradients within a cell at open circuit can in principle lead to a cell potential different from U^θ.

Immediately after the cell is exposed to oxygen (time $t = 0^+$), $c_o|_+$ should rapidly reach the saturated liquid-phase oxygen concentration c_o^{sat} if the kinetics of oxygen absorption is fast in comparison to oxygen diffusion rates. (During this very early time, the cell potential will rise quite rapidly from the equilibrium potential achieved at open circuit under inert gas to a value somewhat above or below the equilibrium potential under oxygen.) At sufficiently short times after the kinetic relaxation associated with sorption, diffusing oxygen will have reached its equilibrium concentration at the gas interface, but will not have penetrated through the separator, so $c_o|_{anode} = 0$, and a concentration overpotential arising from oxygen may affect the cell voltage. When present, this overpotential would be expected to relax on a diffusional timescale, which — unlike the kinetic relaxation — would depend on the separator thickness. As time passes during the preconditioning, the oxygen concentration at the negative electrode rises from zero, eventually reaching c_o^{sat} after sufficient time;

the cell voltage correspondingly relaxes to U^θ.

To analyze the transient evolution of cell voltage, note that in a one-dimensional cell at open circuit with no salt gradients, equation 4.14 does reduce to Fick's law for oxygen. If the early kinetic relaxation is assumed to be very short in comparison to the diffusion time, the open-circuit potential drop across a planar separator of thickness L with constant Fickian oxygen diffusivity $D_\mathrm{o} = c_\mathrm{T}\mathscr{D}_\mathrm{o}/c_0$ during preconditioning relaxes according to

$$\Delta\Phi(t) - U^\theta = \frac{RT\nu_\mathrm{e}c_\mathrm{o}^\mathrm{sat}\tilde{\Xi}}{Fz_+\nu_+c_\mathrm{T}}f(t), \quad \text{where}$$

$$f(t) = -\frac{2}{\pi}\sum_{k=1}^{\infty}\frac{(-1)^k}{k-\frac{1}{2}}\exp\left[-\frac{\left(k-\frac{1}{2}\right)^2\pi^2 D_\mathrm{o}t}{L^2}\right]. \quad (4.24)$$

(The function f is defined so that $f(0) = 1$ and $\lim_{t\to\infty} f(t) = 0$.) Voltage relaxation occurs over a time interval that scales as L^2/D_o; thus thinner cells require far shorter preconditioning intervals.

4.6 Experimental quantification of electro-osmosis

The above discussion highlights a straightforward method for measuring the effective oxygen diffusivity and electro-osmotic coefficient. Known oxygen gradients in the cell can be established by saturating electrolytic solutions with very small initial oxygen concentrations. The parameters can be measured by measuring the OCP over time as an imposed oxygen activity gradient relaxes. At these long times, the first eigenvalue of equation 4.24 will dominate giving,

$$\Delta\Phi(t) - U^\theta \approx \frac{4RT\nu_\mathrm{e}c_\mathrm{o}^\mathrm{sat}\tilde{\Xi}}{\pi Fz_+\nu_+c_\mathrm{T}}\exp\left(-\frac{\pi^2 D_\mathrm{o}t}{4L^2}\right). \quad (4.25)$$

The exponential time constant for the potential relaxation will be the same whether oxygen is diffusing into the electrolyte, which we will call oxygen saturation, or diffusing out of the electrolyte, which we will call oxygen starvation. Rearrangement of equation 4.25 suggests plotting a normalized OCP, Φ_n, and normalized time, t_n, as shown in equation 4.26, so the electro-osmotic coefficient and the effective oxygen diffusivity can be read directly from the intercept and the slope of the plot.

$$\ln\Phi_\mathrm{n} = \ln\tilde{\Xi} - D_\mathrm{o}t_\mathrm{n}, \quad (4.26)$$

$$\Phi_{\mathrm{n}} = \frac{\left(\Delta\Phi\left(t\right) - U^{\theta}\right)\pi F z_{+}\nu_{+}c_{\mathrm{T}}}{4RT\nu_{\mathrm{e}}c_{\mathrm{o}}^{\mathrm{sat}}}, \tag{4.27}$$

$$t_{\mathrm{n}} = \frac{\pi^2 t}{4L^2} \tag{4.28}$$

In the preconditioning of Li/O_2 cells described by Griffith *et al.*,[21] initially argon saturated electrolytic solutions were exposed to and eventually saturated with oxygen while the OCP was measured, yielding many oxygen saturation data sets. In these measurements, the OCP rose rapidly over the first several minutes, likely owing to saturation of oxygen in the solution at the liquid/gas interface, then gradually over the next few hours, resulting from relaxation of oxygen activity gradients as oxygen saturated the electrolytic solution. Additionally, preconditioning the cells as before, then purging with argon gas for 1 min and measuring the OCP as it fell provided several oxygen starvation data sets. Purge time was limited to 1 min to prevent changes in the thickness of the cell due to evaporation of the solvent. The short purges left a certain amount of oxygen in the headspace of these cells. Figure 4.1 shows the relaxation of cell potential to equilibrium over time for both conditions.

Figure 4.1 shows that the magnitude of the relaxation was starkly lower for the cells where oxygen was leaving the electrolytic solution than the cells where oxygen was saturating the electrolytic solution. There are likely multiple reasons for this. Fresh metallic lithium electrodes were used in this experiment, which were likely forming a solid electrolyte interphase while these measurements were being taken. The initial oxygen concentration gradients were also likely higher in the oxygen saturation experiments, since the limited purge time left a certain amount of oxygen in the headspace of the cell. Lastly, there was a linear change in potential over the whole course of the oxygen starvation experiments, which was attributed to corrosion processes and subtracted out to yield the data shown in Figure 4.1. To evaluate the impact of this corrosive process on the measurement of transport parameters, both oxygen saturation and starvation experiments were repeated with 100 μm, 100 mesh nickel electrodes (99.7% Alfa-Aesar, USA) instead of porous carbon electrodes. When nickel electrodes were used, no signature of corrosion was apparent in either of the OCP relaxations. The thinner nickel electrodes also allowed the sensitivity of the relaxation constant to the cell thickness to be evaluated. Direct comparison of the parameters measured using the two different electrode thicknesses can be achieved by plotting the normalized data suggested in equation 4.26. Figure 4.2 shows the data plotted this way for both the porous carbon and nickel electrode oxygen saturation and oxygen starvation tests. Note that the magnitude of the voltage relaxations were higher for oxygen saturation experiments than oxygen starvation experiments for the nickel electrodes as

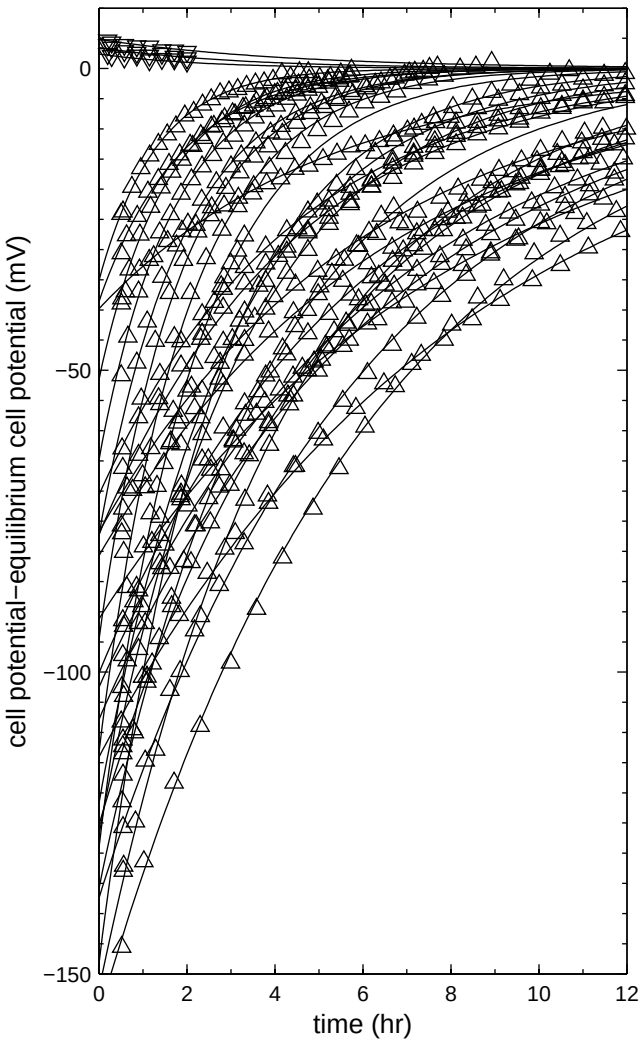

Figure 4.1: Cell potentials exponentially approaching their equilibrium value for cells with porous carbon electrodes being saturated with oxygen △ and starved of oxygen ▽ with solid lines showing the exponential fits.

Table 4.1: Values for the electro-osmotic coefficient $\tilde{\Xi}$ measured from voltage relaxations vary significantly for each set of experimental conditions

carbon		nickel	
saturation	starvation	saturation	starvation
-2000 ± 730	-73 ± 25	-7400 ± 5000	-800 ± 170

well.

Figure 4.2 shows that the effective oxygen diffusivity measured for all four cases are the same within experimental error. The average effective oxygen diffusivity from all the experiments is $2.8 \pm 1.8 \times 10^{-7} \mathrm{cm}^2 \mathrm{s}^{-1}$. Significant error in the measured effective diffusivity is likely due to variability in the cell thickness owing to the use of non-rigid, glassy fiber separators. The values of the electro-osmotic coefficients are different for each data set. At the end of the oxygen saturation experiments, cells with both nickel and porous carbon electrodes had an OCP of 2.96 V within experimental error. The values of the electro-osmotic coefficient measured for each test are given in Table 4.1.

Given that the values for the electro-osmotic coefficient for each condition are significantly different, it is worth performing an auxiliary measurement to provide a range of reasonable values for the parameter. The ionic conductivity of a solution is directly measurable and relates to the other transport parameters as shown in equation 4.9 making it a very desirable alternative. Ionic conductivities of 1 M Li TFSI equilibrated with an argon (<1 ppm oxygen) atmosphere and pure oxygen (99.98% Cryogenic Gases USA) at 0.5 bar gauge atmosphere were measured with a Seven-Multi conductivity meter (Metler Toledo, USA) in an argon glovebox (Vacuum Atmospheres, USA) with less than 1 ppm oxygen and moisture concentration. First the oxygen free value was obtained by measuring the as prepared solution in the glovebox giving a conductivity of 15.18 mS cm^{-1}. Then, the electrolytic solution was exposed to oxygen at 0.5 bar gauge and the conductivity was measured for several hours. During this time the oxygen concentration in solution equilibrated with the pressure of oxygen in the gas phase and the conductivity fell to a value of 15.11 mS cm^{-1}. This minute deviation from the oxygen-free value is actually lower than the minimum difference detectable with the conductivity probe, which is precise to 0.5%. Practically this value can be used as an upper bound for the conductivity change.

To relate the values of the conductivity to the electro-osmotic coefficient, several other transport parameters must be known. In the limit of zero oxygen concentration, it can be shown that the electrolyte diffusivity, cation transference number, and ionic conductivity simplify to their oxygen free values. This means that of the six coefficients necessary to

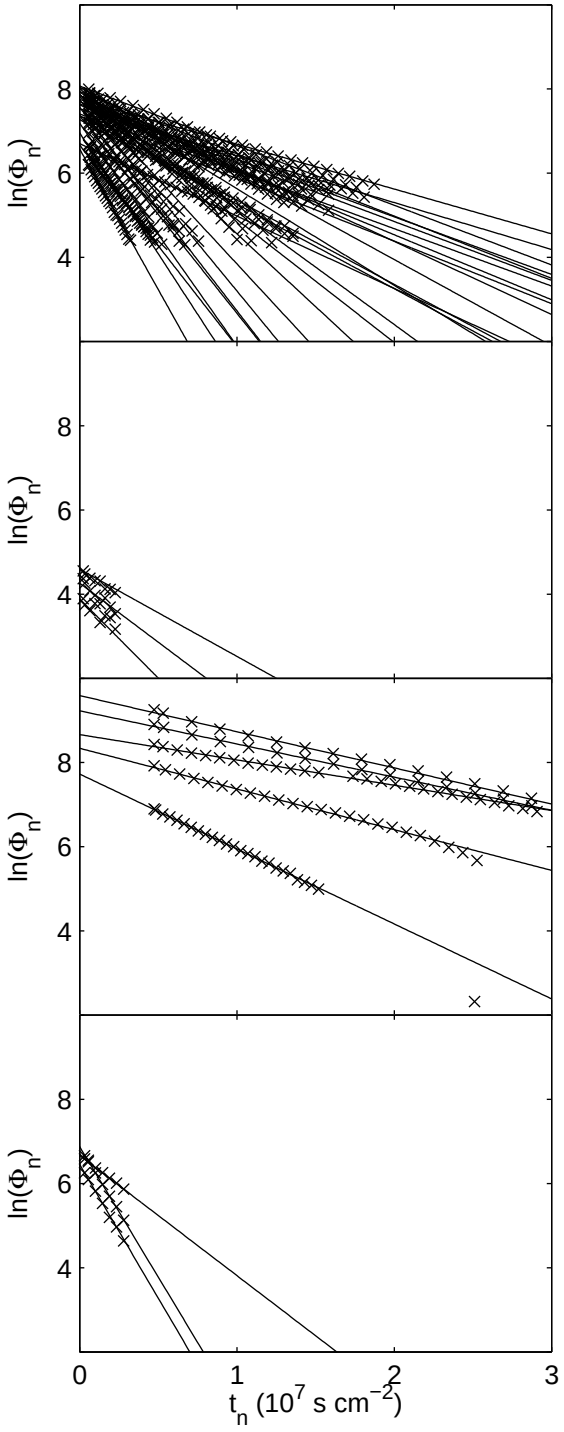

Figure 4.2: Normalized plots of the relaxations for the cells with nickel electrodes and the cells with porous carbon electrodes intercept the y axis at the natural log of the electro-osmotic coefficient, and have slopes of the effective oxygen diffusivity through the cell.

model the system, three can be obtained from literature and the oxygen-free electrolyte conductivity can provide a fourth. Diffusivities of lithium salts in organic solvents are commonly on the order of $1\times10^{-5}\mathrm{cm}^2\mathrm{s}^{-1}$. Transference numbers for lithium salts in organic solvents are about 0.4. The diffusivity of oxygen in pure DME is given by Hartmann *et al.* as $6\times10^{-5}\mathrm{cm}^2\mathrm{s}^{-1}$. Assuming the oxygen contributes negligibly to the solution volume, the composition of the solution can be calculated using the partial molar volumes of electrolyte and solvent. The measurements of Brouillette *et al.* put the partial molar volumes of LiTFSI in DME and of pure DME at 0.1046 M^{-1} and 0.0210 M^{-1}, respectively.[63] The remaining coefficients, D_{eo} and t^{o}_{+0}, can then be calculated using the measured effective oxygen diffusivity and either the measured electro-osmotic coefficient or the measured conductivity and equations 4.7 and 4.10 or 4.9. This allows the six macroscopic coefficients to be estimated at any solution composition. Note that even in the limit of zero oxygen concentration, equations 4.7 and 4.11 remain finite, suggesting that diffusion can be affected by very small concentrations of oxygen.

Following this analysis, we see that all four values of the electro-osmotic coefficient measured from relaxation experiments predict that the ionic conductivity falls to negative values at the saturated oxygen concentration suggested by Hartmann *et al.*.[64] This aphysical result likely owes to corrosion processes occurring in the cell and affecting the OCP measurement. Using the ionic conductivity to calculate t^{o}_{+0} gives two possible values since equation 4.9 is quadratic in t^{o}_{+0}. Conveniently insertion of the two possible values of t^{o}_{+0} into equation 4.10 gives two different signs for Ξ, so the value giving the sign consistent with the measured value is chosen. Using this value of t^{o}_{+0} the corresponding value of $\tilde{\Xi} = -7$ can be calculated. Not only is this value far smaller than any value suggested from the relaxation experiment, but it also predicts that the total voltage change in any of the relaxation experiments should be less than a millivolt.

Given the uncertainty in the values of the measured transport parameters, it is more important than ever to check their thermodynamic consistency. This is done most simply using the Onsager-Stefan-Maxwell transport coefficients. The five Stefan-Maxwell coefficients $\mathscr{D}_{0+}$, $\mathscr{D}_{0-}$, $\mathscr{D}_{\mathrm{o}+}$, $\mathscr{D}_{\mathrm{o}-}$, and $\mathscr{D}_{\mathrm{o}0}$ can be expressed in terms of the five macroscopic properties $\mathscr{D}_{\mathrm{e}}$, $\mathscr{D}_{\mathrm{o}}$, $\mathscr{X}_{\mathrm{eo}}$, t^0_+, and Ξ as

$$\mathscr{D}_{0+} = \frac{\frac{\nu_+}{\nu_{\mathrm{e}}}\left(\mathscr{D}_{\mathrm{e}}\mathscr{D}_{\mathrm{o}} - \frac{\nu_{\mathrm{e}}c_{\mathrm{e}}c_{\mathrm{o}}}{c_{\mathrm{T}}^2}\mathscr{X}_{\mathrm{eo}}^2\right)}{\left(\mathscr{D}_{\mathrm{o}} - \frac{c_{\mathrm{o}}}{c_{\mathrm{T}}}\mathscr{X}_{\mathrm{eo}}\right)\left(1-t^0_+\right) - \left(\mathscr{D}_{\mathrm{e}} - \frac{\nu_{\mathrm{e}}c_{\mathrm{e}}}{c_{\mathrm{T}}}\mathscr{X}_{\mathrm{eo}}\right)\Xi}, \tag{4.29}$$

Table 4.2: Values of the macroscopic and microscopic transport coefficients in the limit of saturated oxygen concentration and negligible concentration

	$\mathscr{D}_\mathrm{e}$	$\mathscr{D}_\mathrm{o}$	t_+^0	κ	Ξ	$\mathscr{X}_\mathrm{eo}$
$c_\mathrm{o}=0$	1e-05	2.3e-7	0.4	15.8	0	4.8e-5
$c_\mathrm{o}=c_\mathrm{o}^\mathrm{sat}$	1e-5	3e-7	0.4	15.69	-6e-3	5.0e-5
	$\mathscr{D}_{0+}$	$\mathscr{D}_{0-}$	$\mathscr{D}_{\mathrm{o}+}$	$\mathscr{D}_{\mathrm{o}-}$	$\mathscr{D}_{\mathrm{o}0}$	$\mathscr{D}_{+-}$
$c_\mathrm{o}=0$	8e-6	8e-6	4e-8	7e-8	5e-7	6e-7
$c_\mathrm{o}=c_\mathrm{o}^\mathrm{sat}$	8.e-6	1e-5	-4.e-8	2e-8	8e-5	4e-7

$$\mathscr{D}_{0-}=\frac{\frac{\nu_-}{\nu_\mathrm{e}}\left(\mathscr{D}_\mathrm{e}\mathscr{D}_\mathrm{o}-\frac{\nu_\mathrm{e}c_\mathrm{e}c_\mathrm{o}}{c_\mathrm{T}^2}\mathscr{X}_\mathrm{eo}^2\right)}{\left(\mathscr{D}_\mathrm{o}-\frac{c_\mathrm{o}}{c_\mathrm{T}}\mathscr{X}_\mathrm{eo}\right)t_+^0+\left(\mathscr{D}_\mathrm{e}-\frac{\nu_\mathrm{e}c_\mathrm{e}}{c_\mathrm{T}}\mathscr{X}_\mathrm{eo}\right)\Xi}, \tag{4.30}$$

$$\mathscr{D}_{\mathrm{o}+}=\frac{\frac{\nu_+c_\mathrm{o}}{\nu_\mathrm{e}c_0}\left(\mathscr{D}_\mathrm{e}\mathscr{D}_\mathrm{o}-\frac{\nu_\mathrm{e}c_\mathrm{e}c_\mathrm{o}}{c_\mathrm{T}^2}\mathscr{X}_\mathrm{eo}^2\right)}{\frac{c_\mathrm{o}}{c_\mathrm{T}}\mathscr{X}_\mathrm{eo}\left(1-t_+^0\right)+\mathscr{D}_\mathrm{e}\Xi}, \tag{4.31}$$

$$\mathscr{D}_{\mathrm{o}-}=\frac{\frac{\nu_-c_\mathrm{o}}{\nu_\mathrm{e}c_0}\left(\mathscr{D}_\mathrm{e}\mathscr{D}_\mathrm{o}-\frac{\nu_\mathrm{e}c_\mathrm{e}c_\mathrm{o}}{c_\mathrm{T}^2}\mathscr{X}_\mathrm{eo}^2\right)}{\frac{c_\mathrm{o}}{c_\mathrm{T}}\mathscr{X}_\mathrm{eo}t_+^0-\mathscr{D}_\mathrm{e}\Xi}, \tag{4.32}$$

$$\mathscr{D}_{\mathrm{o}0}=\frac{\mathscr{D}_\mathrm{e}\mathscr{D}_\mathrm{o}-\frac{\nu_\mathrm{e}c_\mathrm{e}c_\mathrm{o}}{c_\mathrm{T}^2}\mathscr{X}_\mathrm{eo}^2}{\mathscr{D}_\mathrm{e}-\frac{\nu_\mathrm{e}c_\mathrm{e}}{c_\mathrm{T}}\mathscr{X}_\mathrm{eo}}. \tag{4.33}$$

Given these relationships, one can compute $\mathscr{D}_{+-}$ as a function of κ, $\mathscr{D}_\mathrm{e}$, $\mathscr{D}_\mathrm{o}$, $\mathscr{X}_\mathrm{eo}$, t_+^0, and Ξ through

$$\frac{1}{\mathscr{D}_{+-}}=-\frac{F^2c_\mathrm{T}z_+z_-}{RT\kappa}+\frac{\nu_\mathrm{e}c_0\left(t_{+0}^\mathrm{o}-t_{+\mathrm{o}}^0\right)\Xi}{\nu_+\nu_-c_\mathrm{e}\mathscr{D}_{\mathrm{o}0}} - \frac{1}{c_\mathrm{e}}\left(\frac{c_0}{\nu_-\mathscr{D}_{0+}+\nu_+\mathscr{D}_{0-}}+\frac{c_\mathrm{o}}{\nu_-\mathscr{D}_{\mathrm{o}+}+\nu_+\mathscr{D}_{\mathrm{o}-}}\right). \tag{4.34}$$

Both the macroscopic transport coefficients and Stefan-Maxwell coefficients depend to some extent on the concentration of oxygen in the electrolytic solution. It has been suggested that the oxygen concentration in an operating Li/O_2 battery will range from negligible to saturated.[11,21] Table 4.2 gives values of the macroscopic coefficients as well as the Stefan-Maxwell coefficients in these two limits of oxygen concentration.

From table 4.2 it is clear that the transport properties at zero oxygen concentration are thermodynamically consistent. At saturated concentration, however, $\mathscr{D}_\mathrm{op}$ becomes negative, so a more thorough check is required. The simplest way to check the thermodynamic

consistency of the transport coefficients is to construct a truncated transport matrix by taking on of the ions as a reference.[58] Arbitrarily taking the positive ion of the electrolyte as the reference we can see that the eigenvalues of the M^{++} matrix are negative definite and therefore thermodynamically consistent.

4.7 Discussion

The apparent disagreement between relaxation experiments and the conductivity measurement is puzzling. Overall, the conductivity measurement is more trustworthy, since it is affected less by any chemical instability or impurity where cell potential will be affected by both these things. Given the lack of change in conductivity, it is reasonable to conclude the effects of multicomponent transport in Li/O_2 batteries will not have a significant impact on cell potential. Also since the conductivity measurement suggests that the OCP relaxation should be small for a range of reasonable values of the effective oxygen diffusivity, the validity of the effective oxygen diffusion measured by fitting large OCP relaxations must be examined closely. It is important to keep in mind that the OCP increased when oxygen was supplied and decreased when oxygen was withdrawn, showing that whatever process determined the OCP, it was dependent on the oxygen concentration. One possibility is that the OCP was being determined by some corrosion process. It is likely that any such reactions would occur at the less stable lithium electrode as opposed to the porous carbon electrode, so the cell geometry would affect the relaxation time for such a process identically. Even in this case it can be argued that the OCP relaxation experiments provide a reasonable estimation of the effective oxygen diffusivity in the electrolytic solution. It can be shown that the impact of the lithium salt on oxygen diffusion suggested by these experiments agrees with data published in the literature.

Capacity vs. discharge rate data commonly show a relatively constant capacity at the lower rates, then a capacity that drops off steeply at higher rates.[11,50] Griffith *el al.* propose that this qualitative shape is a signature of oxygen diffusion limitations in the battery. A simple mass balance shows that for the entire thickness of the electrode L to be supplied with oxygen, the limiting current density i_{L} is determined by the maximum oxygen flux into the electrode, which scales with the effective oxygen diffusivity D_{o} and the saturated oxygen concentration $c_{\mathrm{o,sat}}$.

$$\frac{i_{\mathrm{L}}F}{2} = \frac{D_{\mathrm{o}}c_{\mathrm{o,sat}}}{L} \tag{4.35}$$

If the capacity vs. rate data show both the plateau and the steep drop off, the rate where the

drop off begins is identified as i_L and can be used to estimate the effective oxygen diffusivity in a cell with known geometry. If the composition is known and estimates of several transport parameters are available, the interaction between oxygen and electrolyte can also be estimated allowing for comparison of material properties insinuated from experiments with ranging geometries and electrolyte compositions.

Despite the detailedf information necessary to make these estimations, two sources were identified that could provide estimations of the transport parameters using this method. Table 4.3 gives numbers extracted from Lu *et al.* and Adams *et al.* necessary for the calculation, and the resulting estimates of the effective oxygen diffusivity and the values of D_{eo}. All of these experiments show that oxygen diffuses more slowly through electrolytic solutions than the pure solvent, since the effective oxygen diffusivity is less than the oxygen diffusivity through pure solvent. Note the Lu *et al.* use $LiPF_6$ and DME, Adams *et al.* use LiTFSI and tetraglyme, and the measurements reported here were done in DME with LiTFSI salt. Despite these small differences in solvent and salt, the values of the effective oxygen diffusion coefficient and D_{eo} from the relaxation experiments and the two literature sources are comparable. This means that even though there is a degree of uncertainty in the origin of the OCP change, the timescale for its relaxation is still consistent with a diffusion process and provides a reasonable estimation of transport parameters.

Table 4.3: Values of geometry and composition of cells used in capacity vs. rate studies showing a transition to oxygen diffusion limited behavior.

Source	$L(\mu\text{m})$	i_L (μA cm^{-2})	D_o (cm^2 s^{-1})	$D_{\text{o}0}$ (cm^2 s^{-1})	$D_{\text{e}0}$ (cm^2 s^{-1})	c_0 (M)	c_e (M)	c_o (M)	D_eo (cm^2 s^{-1})
Lu *et al.*	20	410	$2e-6$	$6e-5$	$1e-5$	8.5	0.1	$8e-3$	1.6e-8
Adams *et al.*	113	25	$0.7e-6$	$3e-5$	$1e-5$	4.5	1	$7e-3$	1.5e-7

As mentioned previously, continuum models of Li/O_2 batteries typically decouple the transport of the electrolyte and oxygen in the solvent. The implicit assumption in this approach, that oxygen gradients will have negligible effect on the cell potential, has been verified experimentally: introduction of oxygen into the electrolyte caused no measurable change in the ionic conductivity. The impact of the presence of the electrolyte on the oxygen diffusion coefficient is much more important however. It has been shown that the diffusivity of oxygen in the electrolytic solution is much lower than the value of the oxygen diffusivity in pure solvent for a range reasonable cell compositions. Since the oxygen diffusivity falls so steeply with electrolyte concentration, it may be advantageous to use lower concentrations of lithium salts. These transport parameters could be used in conjunction with an accurate continuum model of a Li/O_2 cell to estimate an optimum electrolyte concentration, which will provide decent ionic conductivity while minimally decreasing the oxygen diffusion coefficient.

4.8 Conclusion

In this section we used the procedure outlined by Monroe *et al.*[58] for modeling transport of four species; two with charge and two neutral. This procedure provided relations between transport coefficients and measurable macroscopic quantities. Relations for several macroscopic quantities simplified to their oxygen-free values in the limit of zero oxygen concentration, allowing 3 of the six parameters to be acquired from pre-existing literature. A procedure for using the OCP of Li/O_2 cells, and the ionic conductivity to calculate the remaining transport parameters was proposed. Relaxation experiments showed that the cell potential took several hours to re-equilibrate after a step change in the oxygen partial pressure in the head space of the cell. It was also observed that the sign of the deviation from equilibrium cell potential was directly related to the direction of the imposed oxygen concentration gradient. Ionic conductivity measurements of the solution equilibrated with argon and equilibrated with 0.5 bar oxygen provided an upper bound for the electro-osmotic coefficient. Comparison of the experimental results along with values estimated from literature showed the elecro-osmotic coefficient negligibly impacts the OCP, however the effective oxygen diffusivity can be three times smaller than what is typically measured in pure solvents. This validates the common approach to modeling transport in the cell using Fick's law on the oxygen and concentrated solution theory for the electrolyte, however, it shows that the effective oxygen diffusivity in this approach will be much smaller than the value of the oxygen diffusivity through pure solvent.

CHAPTER 5

Rate Performance of Lithium/Oxygen Batteries

5.1 Introduction

Limited range and high cost currently prevent the widespread implementation of battery-electric vehicles.[65] Both of these challenges could be addressed by realizing an efficient, cyclable lithium/oxygen (Li/O_2) battery. For automotive applications, the high theoretical specific energy of Li/O_2 chemistry makes it attractive as a possible alternative to lithium-ion chemistries.[66,67]

Although relatively high cell capacities have been obtained on the laboratory scale,[68] a number of significant barriers, including short cycle life and low charging efficiency, must be overcome for Li/O_2 battery technology to become practical.[66] Addressing such challenges demands a deeper understanding of the energy storage and retrieval mechanisms in the porous positive electrode. This investigation aims to shed light on the operating mechanisms of non-aqueous Li/O_2 cells, by examining how cell capacity and discharge-product morphology depend on the discharge rate.

Non-aqueous Li/O_2 cells ideally discharge by the reduction of oxygen to form an oxygenated lithium species at the positive electrode,[69] which substantial literature confirms is mostly lithium peroxide (Li_2O_2).[10,15,50,70,71] During an ideal recharge process, the Li_2O_2 should decompose electrochemically, returning lithium and oxygen to their original states. Even when taking the masses of the electrode substrate and the oxygen added to the peroxide into account, Li/O_2 cells exhibit theoretical specific energies 3-5 times greater than conventional lithium-ion cells.[68] This benefit owes both to the exchange of intercalation-compound-laden positive electrodes for lighter gas-diffusion electrodes, and to the replacement of the graphite negative electrode with energy-dense metallic Li.

There are many reports of discharged Li/O_2 cells whose positive electrodes contain electrodeposited Li_2O_2 particles with a toroid-like morphology; the toroids typically have characteristic dimensions of the order of 100 nm.[50,70,72–75] Since Li_2O_2 is a bulk insulator

that in principle should prevent electrons from traveling such distances,[76] the observations suggest that unconventional electron-transport pathways or diffusion of intermediates may play roles in the discharge process. For example, mechanisms by which charge could travel through amorphous Li_2O_2[77] or across crystalline Li_2O_2 via its surface,[78] grain boundaries,[79] or defects in its bulk[76] have been proposed. Studies also show that the morphology of Li_2O_2 deposited on a porous-carbon positive electrode can change when additives are incorporated.[74,80] Adams *et al.* provided a detailed set of hypotheses to rationalize how discharge-product morphology depends on discharge rate.[50] They observed that the Li_2O_2 morphology transitioned from toroids to a compact film as the discharge-current density increased; they also noted that capacity remained relatively stable until a critical rate was reached, above which the capacity substantially deteriorated.

Although a few studies highlight challenges related to the rate performance of Li/O_2 cells and cell design, research in this direction has received relatively little attention.[68] For example, Adams *et al.*[81] fabricated a bipolar-plate battery design aimed at meeting various goals set by the U.S. Advanced Battery Consortium;[82] their testing, which explored discharge currents up to 4 $mAcm^{-2}$ (per superficial electrode area), suggests that current densities of the order of 1 $mAcm^{-2}$ could be required in practice. Lu *et al.* fabricated extremely thin electrodes, with the aims of mitigating mass-transport limitations and allowing higher current densities.[11] They discharged their cells at up to 0.76 $mAcm^{-2}$ superficial positive-electrode area. Jung *et al.* achieved one hundred cycles at rates of ± 1 $mAcm^{-2}$ by limiting the depth of discharge, and also demonstrated comparable capacity at ± 3 $mAcm^{-2}$.[83]

A viable vehicular battery must retain its performance at higher rates. Consequently, more work is needed to understand the properties of Li/O_2 batteries operated at high current densities. In addition to the aforementioned effects on capacity and Li_2O_2 morphology, there is evidence that higher rates of discharge result in lower overpotentials during recharging.[50,70] Hence discharge rate may ultimately control not only the capacity, but also the round-trip efficiency of a Li/O_2 battery. This paper explores the capacity of Li/O_2 cells and morphology of Li_2O_2 at the end of first discharge in the practically significant 0.1 to 1 $mAcm^{-2}$ superficial current-density range. Cell capacity is found to fall with a power-law dependence on current across these rates. Understanding this response, which can be associated with a Peukerts-law[84] exponent of 1.6 ± 0.1, could aid the engineering of cells with better rate performance.

More than 60 separate first-discharge experiments were performed across four rates. Electrodes exhibiting near-average capacity at a given rate were characterized using XRD and SEM. Air-free sample-transfer techniques were used to implement XRD of representative electrodes, minimizing any changes to the discharge-product morphology incurred by

air exposure. A novel sample-transfer technique was developed for SEM that allows air-tight argon-filled sample holders to be opened inside the microscope chamber after vacuum is drawn. Micrographs from representative cells are used to develop quantitative measures of how the sizes and shapes of deposited Li_2O_2 particles vary with control conditions.

The observed power-law dependence of discharge capacity on discharge rate is consistent with a macroscopic oxygen-transport limitation that lowers utilization of the porous positive electrode. Particle volumes are also found to fall dramatically with rate, and their surface-to-volume ratios rise correspondingly. Thus Li_2O_2 appears to be produced by a nucleation-and-growth process over the range of currents studied, supporting the notion that particle growth is transport-limited on a microscopic scale, as well as on a macroscopic scale.[85] Particle shapes could be determined by voltage-dependent surface energetics, consistent with a deposition mechanism involving direct charge transfer. Alternatively, the particle-growth process could be mediated by chemical precipitation of a neutral reaction intermediate, whose local supersaturation in the liquid rises with discharge rate.

5.2 Experimental

5.3 Results

5.3.1 First-discharge capacity vs. Rate

More than 60 independent cells were assembled and discharged at four rates to establish the average capacity. Over the course of data collection approximately two out of every three assembled cells discharged successfully (there were a total of 42 successful first discharges). For each discharge rate, a successful discharge was defined by: monotonically decreasing potential for the entire discharge period; clear sudden death of voltage at the end of discharge (i.e., a cell-voltage vs. capacity slope within two standard deviations of the mean for that rate at the cutoff voltage); and a first-discharge capacity within two standard deviations of the mean for that rate. Figure 5.1 shows the potential vs. capacity curves for all successful discharges at each discharge rate studied.

Averages and standard deviations of the first-discharge capacities are shown in vertical solid and vertical dashed lines respectively. The figure shows eight successful discharges at 0.1 $mAcm^{-2}$, twelve at 0.2 $mAcm^{-2}$, thirteen at 0.5 $mAcm^{-2}$, and nine at 1 $mAcm^{-2}$. Significant statistical variation was observed in both the first-discharge capacity and overpotential. Figure 5.2 shows the cell potential at 50% depth of discharge (DOD) vs. discharge rate for all successful discharges, along with the averages and standard deviations

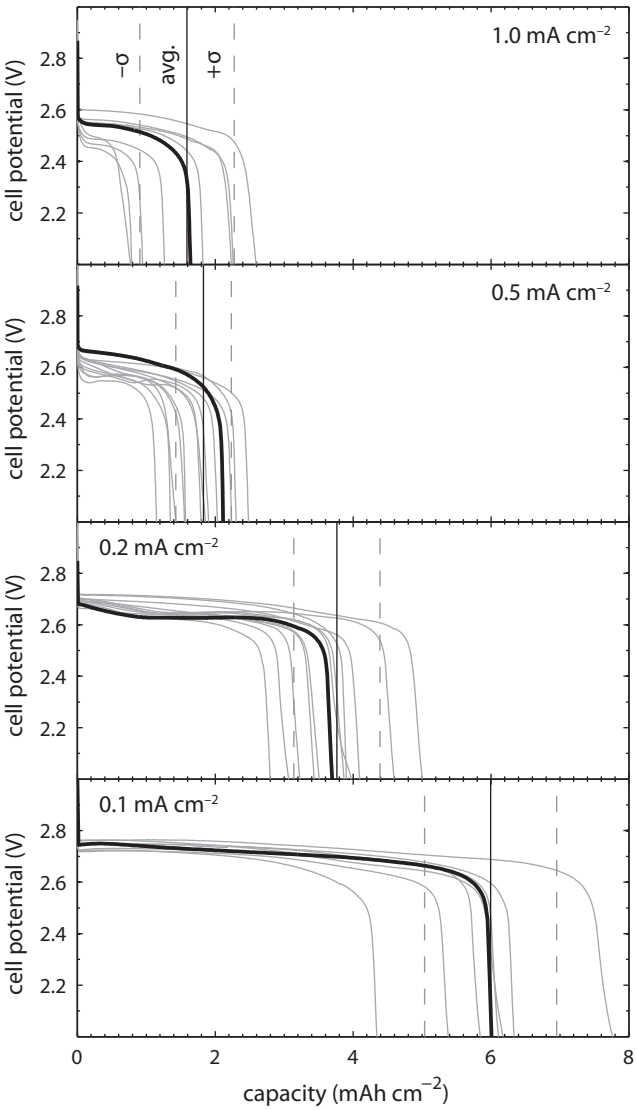

Figure 5.1: Dependence of potential on capacity (per superficial area) for lithium/oxygen cells discharged at 1.0, 0.5, 0.2, and 0.1 mAcm^{-2}. Vertical solid lines show the average discharge capacity; vertical dashed lines indicate its standard deviation. The black curves correspond to the discharges of cells used for SEM and XRD.

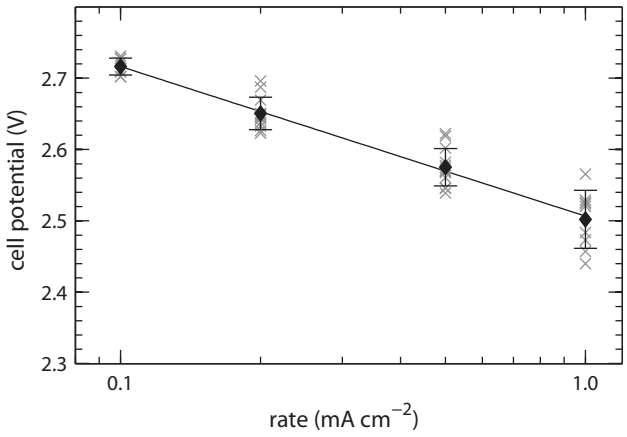

Figure 5.2: Cell potential at 50% depth-of-discharge with respect to rate. Diamonds show the mean potential, and error bars, one standard deviation.

of the cell potentials at 50% DOD. Following an analysis similar to that of Viswanathan *et al.*,[86] these yield a Tafel slope of 11±1 V^{-1} and an exchange-current density of 7±3 μA cm^{-2} (superficial).

As far as we know, no prior reports have quantified the inherent random variability of Li_2O_2 cells. The stochastic variation is measured by the standard deviation of capacity and mid-discharge cell potential, which both vary increasingly as the discharge rate rises. Large mean overpotentials could arise from sluggish reaction kinetics[87] or oxygen-diffusion limitations;[9] the extent of variation in the overpotential could owe to the inherent variability of pore-surface area in the electrodes.

Peukerts law is a well-known empirical expression that describes the relationship between a battery cells discharge current and discharge duration as a power law.[84] In the present context it is convenient to express Peukerts law in terms of the areal capacity q_{total} (superficial basis) and the superficial discharge-current density i, as

$$\ln\left(\frac{q_{\text{total}}}{1\ \text{mAhcm}^{-2}}\right) = (1-k)\ln\left(\frac{i}{i_{\text{ref}}}\right) \tag{5.1}$$

where k is the Peukert exponent and i_{ref} is an empirically evaluated reference current density. If the full capacity of a battery system were available at all discharge rates, its Peukert exponent would be 1. The second law of thermodynamics requires that $k > 1$; the specific exponent observed for a given cell chemistry and geometry is commonly acknowledged to arise from the combination of dissipative processes that limits capacity (ohmic loss, mass-transport limitations, kinetic resistances, etc.).[88] Peukerts law fits the observed rate depen-

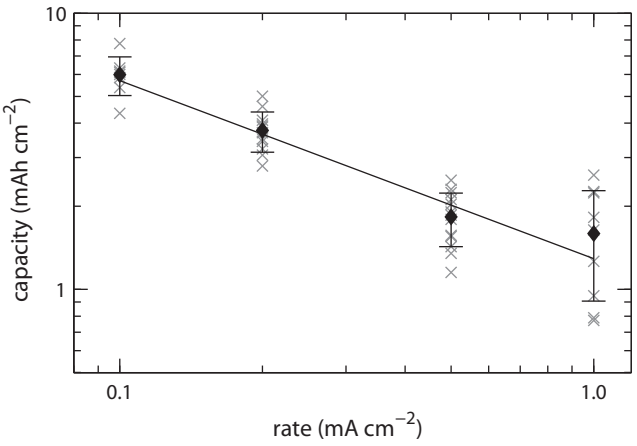

Figure 5.3: Capacity falls as a power law with respect to discharge rate. Capacity per geometric electrode area achieved at the 2 V cutoff potential as a function of discharge-current density on a geometric-area basis. Diamonds show the average discharge capacity, and error bars show one standard deviation

dence of capacity in some current ranges for lead/acid and lithium-ion batteries.[84,89–91] The lead/acid system, which may be most comparable to Li/O_2 because it also operates by a precipitation-dissolution mechanism, satisfies Peukerts law well over a broad current range, with an exponent of 1.4.[89]

Figure 5.3 presents the areal discharge capacities with respect to discharge rate for the successfully discharged Li/O_2 cells. The capacities observed during the Li/O_2-cell discharges follow a power-law dependence on the discharge current, yielding a Peukert exponent of 1.6±0.1 and reference current density of 1.7±0.5 mAcm^{-2}.

5.3.2 Discharge-product identification

XRD spectra from representative positive electrodes at each discharge rate are shown in Figure 5.4. Since variability in capacity could arise from side reactions or poor selectivity for Li_2O_2, XRD was used to confirm the presence of the Li_2O_2 discharge product. (Note that because XRD can only identify crystalline phases, any amorphous compounds would not be detected.) Although past studies have identified products from side reactions with the solvent,6 lithium salt,33 and positive electrode,34 the only consistently apparent diffraction peak unique to the electrodes studied here corresponds to crystalline Li_2O_2. Evidence of trace crystalline LiOH, which manifests as an apparent small second peak adjacent to the Li_2O_2 (100) peak, was seen in some cases; in Figure 5.4, for example, trace LiOH affects the spectrum of the electrode discharged at 0.5 mAcm^{-2}. In every XRD spectrum, the

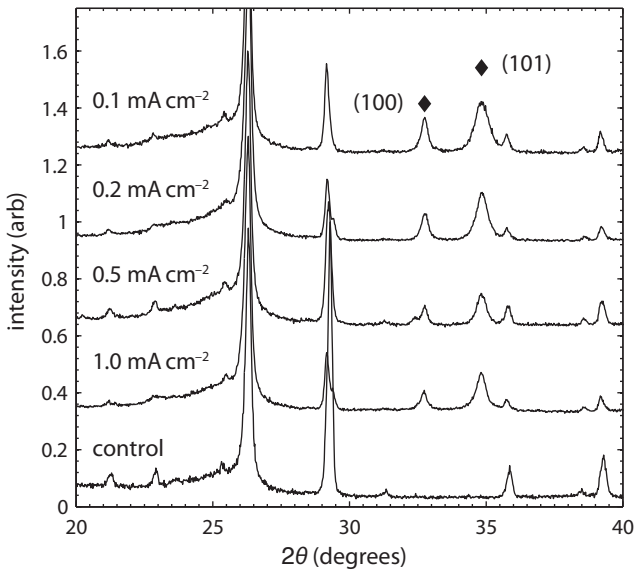

Figure 5.4: Diffraction spectra of representative positive electrodes at all four discharge rates exhibit peaks that correspond to the (100) and (101) reflections of Li_2O_2.

height of the peak corresponding to the Li_2O_2 (100) plane is slightly larger relative to the (101) peak than would be expected for large crystallites of pure Li_2O_2. The broadening of the peaks associated with Li_2O_2 suggests a crystallite size of about 20 nm, which was constant across all rates. No signal for crystalline Li2CO3 or Li2O was observed in any XRD sample.

5.3.3 Discharge-product morphology

In hopes of isolating the effect of applied current on discharge-product morphology, microscopy was performed on electrodes from cells exhibiting near-average capacity at each of the discharge rates. Figure 5.5 shows SEM images of Li_2O_2 particles gathered at end-of-discharge from representative cells at each of the discharge rates, whose corresponding discharge curves are highlighted in Figure 5.1. During all measurements, the SEM beam was destructive to the Li_2O_2; owing to their smaller sizes, the Li_2O_2 particles deposited at higher rates were destroyed more quickly. Degradation of the Li_2O_2 particles during imaging was mitigated by using relatively fast scan rates and integrating over 64 scans, as described previously.

In general, the micrographs in Figure 5.5 show that the Li_2O_2 deposits take disk-like cylindrical shapes at the lower rates, while needle-like particles form at the highest rate.

Note that the characteristic Li_2O_2 discharge-product shape observed at low rates is often referred to in the literature as toroidal, as mentioned in the Introduction.[70,72–74,81] The shapes observed in the present work were consistent with those seen by other researchers, but the larger particles are referred to as disks or cylinders here because 1) none of the particles was observed to contain a central void space and 2) asserting that particles are toroids could imply a particular particle-growth mechanism in which nucleation progresses to propagation via a ring-shaped primary structure, rather than via a linear (needle- shaped) or hemispherical primary structure. At the lowest rate, 0.1 $mAcm^{-2}$, the axial dimension of the Li_2O_2 disks is largest. At the two lowest rates, 0.1 and 0.2 $mAcm^{-2}$, parallel stria spaced by about 20 nm can be discerned on the curved faces of the particles. As the rate increases from 0.1 to 0.5 $mAcm^{-2}$, the particle heights decrease, while their radii stay relatively constant the aspect ratio rises with current. The height and radius trends reverse for the particles formed at 1 $mAcm^{-2}$; if these particles are considered to be cylindrical rods as well, then the typical aspect ratio is dramatically smaller than the aspect ratios at lower currents due to the qualitative change in shape.

SPIP image-analysis software was used to determine average dimensions of the Li_2O_2 particles formed at each discharge rate. Multiple SEM images were processed to identify at least 25 particles from each carbon electrode at each discharge rate, for which average cylinder heights and diameters were recorded. Table 5.1 reports the diameter, height, surface-to-volume ratio, and number of particles (estimated using the density of crystalline Li_2O_2[92]) alongside the total product volume formed (estimated based on mean particle size) and capacity at each rate. Although diameters of the disk-like particles appear to be roughly constant within error across the three slowest discharges, their heights vary with more significance.

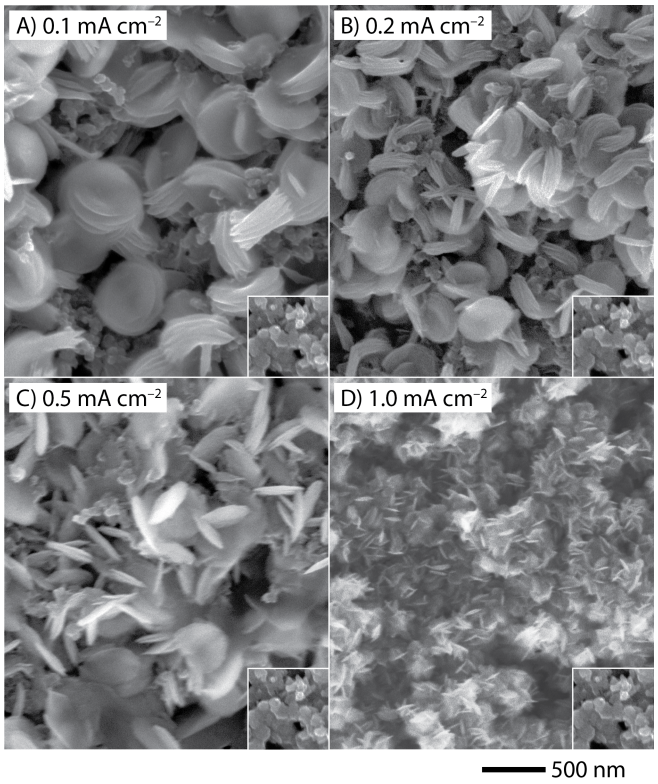

Figure 5.5: Scanning electron micrographs of Li_2O_2 formed at various discharge rates (100,000× magnification). The inset at the bottom right of each image shows a control electrode at similar magnification.

Table 5.1: Variation of the dimensions of individual Li_2O_2 particles and cumulative amount of Li_2O_2 formed with respect to the discharge current density

rate (mA cm^{-2})	particle diameter (nm)	particle height (nm)	particle volume ($\times 10^5$ nm^3)	surface-to-volume ratio ($\times 10^{-2}$ nm^{-1})	number of particles ($\times 10^{12}$)	total product volume (mm^3)	discharge capacity (mAh cm^{-2})
0.1	415 ± 47	188 ± 44	254 ± 72	2.0 ± 0.5	0.22 ± 0.07	5.7 ± 0.9	6.0 ± 1.0
0.2	346 ± 41	88 ± 24	83 ± 26	3.40 ± 1.0	0.43 ± 0.16	3.6 ± 0.6	3.8 ± 0.6
0.5	334 ± 51	65 ± 19	57 ± 21	4.3 ± 1.4	0.33 ± 0.13	1.9 ± 0.4	2.0 ± 0.4
1.0	18.6 ± 4.8	109 ± 17	0.30 ± 0.12	23.3 ± 7.0	51 ± 29	1.5 ± 0.6	1.6 ± 0.7

Figure 5.6 shows how the discharge-product-particle volume, total number of particles, and particle surface-to-volume ratio vary with discharge rate, as well as providing schematic illustrations of the mean particle shapes, with relative sizes to scale. Estimates of the total numbers of particles based on the mean capacity and mean particle size correlate well with estimates of the total number of particles on the electrode surface computed using a direct measurement of particle surface density, suggesting that the structures seen on the surface likely contribute to the total capacity of the discharged cell. The total number of particles appears to rise super-exponentially as the discharge rate increases.

5.4 Discussion

Significant attention has been given to possible kinetic limitations of Li_2O_2 formation and ways to address them.[7,87,93,94] The present electrochemical and morphology measurements suggest several factors besides reaction kinetics that could limit the performance of Li/O_2 cells, however. Performance limitations could owe in part to diffusive processes: although the importance of oxygen solubility and diffusivity in the liquid electrolyte has been recognized,[9] few efforts have been made to correlate these parameters with observed overpotentials and capacities in battery cells. Discharge-product morphology could also limit performance: a lowering of cell potential (i.e., an increase in apparent overpotential) could be associated with the surface-energy change incurred by creating Li_2O_2/electrolytic-solution and Li_2O_2/electrode interfacial areas at the expense of electrolytic-solution/electrode interfacial area.[95,96]

Since the primary advantage of the Li/O_2 chemistry over Li-ion chemistry is its high specific energy, it is important that much of the capacity of the battery be available in response to all practical current demands. Figure 5.3 shows that the available capacity of the battery falls faster with rate than it does in other typical precipitation/dissolution battery systems, posing a design problem that merits close study: indeed, the Li/O_2 Peukert exponent of 1.6 ± 0.1 is even greater than the exponent of 1.4 for lead/acid cells,[89] whose poor rate performance is well known. Substantial transport limitations associated with oxygen could partially explain the rapid decrease in capacity with increasing current density in Li/O_2 cells. Since the cell reaction consumes molecular O_2, the rate of reaction in the porous positive electrode, determined by the current density, should always be balanced by the rate of oxygen diffusion through the pore-filling electrolyte. This diffusion rate is proportional to the oxygen permeability (the product of saturated O_2 concentration and effective O_2 diffusivity).

Since oxygen is more readily available near the gas reservoir, discharge-product forma-

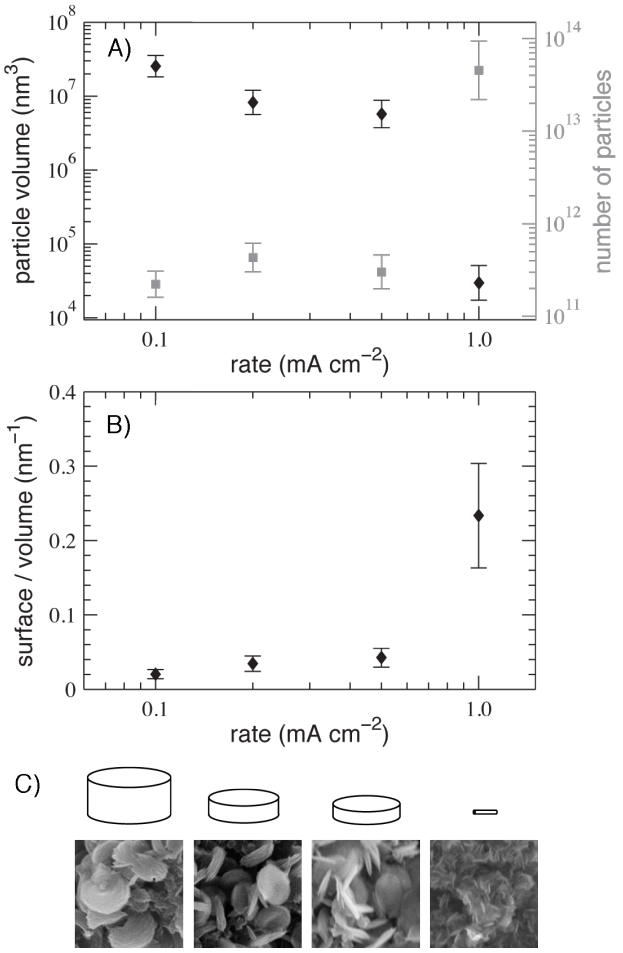

Figure 5.6: Particles decrease in volume, but increase in surface area and number as rate increases. A) Li_2O_2 particle volume and estimated total number of Li_2O_2 particles as functions of discharge rate. B) Surface-to-volume ratio of discharge-product particles as a function of discharge rate. C) Schematics of Li_2O_2 disks and needles with mean proportions drawn to scale, shown above SEM images for comparison.

tion should run to completion there first. Dissolved O_2 must subsequently diffuse through this Li_2O_2-saturated domain at the rate demanded by the applied current. Given the extremely low O_2 solubility of DME,[9] and in light of typical O_2 diffusivities, the flux demanded by the discharge current can drive the O_2 concentration to vanish within a distance far smaller than the positive-electrode thickness.[11] Sudden death of voltage then occurs when the O_2 flux across the Li_2O_2-saturated domain cannot maintain the current density. Under the assumption that the capacity of the battery will be proportional to the distance that O_2 can penetrate into the positive electrode, the capacity would be expected to fall as a function of current with a Peukert exponent of 2, sufficiently close to the observed value of 1.6 ± 0.1 to suggest that macroscopic O_2 transport contributes to rate limitations.

Higher-order corrections owing to the discharge-product morphology could explain the fact that the observed Peukert exponent is somewhat smaller than 2. Under the hypothesis that O_2 transport plays a role in limiting discharge capacity, deviations from a Peukert exponent of 2 can be attributed to local changes in the O_2 permeability. Since the saturated O_2 concentration is a thermodynamic quantity, it is by definition rate-independent; thus, to rationalize the data, the effective O_2 diffusivity must be increasing somewhat with rate, even as the O_2 penetration depth is falling. Such an affect can be explained by observing that the effective diffusivity involves the electrode porosity and tortuosity. The SEM images show that the mean size of the Li_2O_2 particles at the lowest rate is comparable to the approximate size of the pores in the electrode (~350 nm). Therefore at low rates, the effective O_2 diffusivity is decreased due to the lower porosity and much greater tortuosity of the diffusion path that O_2 must travel to reach un-utilized pore volume deeper within the electrode. At the highest rate, the needle-like deposits have a volume that is two to three orders of magnitude less than the disks. These needles occlude far less of the native pore structure of the carbon electrode, leading O_2 to have a higher effective diffusivity. This may explain why the Peukert exponent is dampened from the extreme value of 2.

To target better rate performance, the solubility and the effective diffusivity of oxygen in the positive electrode should be made as large as possible. A simple way to raise the oxygen solubility would be to raise the partial pressure of oxygen in the gas phase. McCloskey *et al.* show that this slightly reduces the overpotential for Li_2O_2 deposition, but do not discuss the effect of a pressure increase on capacity in great detail.[94] Nemanick *et al.* show that at a given discharge rate, the capacity increases with increasing pressure.[97]

The observed morphology differences among Li_2O_2 particles formed at different discharge rates raise more fundamental questions about the connection between the discharge mechanism of Li/O_2 cells and the cell voltage. Due to the nanoscale-particulate nature of the discharge products that form in the porous electrode, a large surface-area change is in-

curred during discharge. The free energy needed to produce this large area could come at the expense of the potential delivered by the cell, reducing energy efficiency. SEM images reported here and elsewhere [11,50,70,72] suggest that the energetics that determines discharge-product shape is clearly affected by the applied current. This interaction needs to be probed more deeply from a theoretical standpoint; some work in that direction has been presented by Horstmann *et al.* [54]

The exact mechanism of charge transport through solid Li_2O_2 (if bulk Li_2O_2 supports any appreciable current at all) is still debated, [76,98] and the reaction pathway by which Li_2O_2 is created is also under discussion. [15,71,98–100] Data about the rate-dependent morphology and distribution of Li_2O_2 particles are relevant to both topics.

At all rates, the particles observed with SEM exhibit at least one characteristic dimension that is too large for electron transport via tunneling. [98] A few alternative mechanisms for charge transport have been put forward to explain such large characteristic particle sizes. Adams *et al.* [81] suggest that the observed large particle sizes can be justified by a peroxide-formation mechanism that progresses through a LiO_2 intermediate, which may be soluble in the solution to an extent that allows it to react at the electrode and diffuse a significant distance before depositing as Li_2O_2. Some studies have proposed charge-conduction mechanisms by which electrons travel through amorphous Li_2O_2 [77] or through crystalline Li_2O_2 along the surface, [78] along grain boundaries, [79] or through bulk defects. [76]

Two of the proposed mechanisms for the formation of Li_2O_2 are: i) reaction/dissolution, where soluble lithium superoxide forms at the pore surfaces within the electrodes, diffuses within pore-filling liquid, and reacts chemically to precipitate on peroxide surfaces [15] and ii) an electrochemical deposition, where Li_2O_2 nucleates on the pore surface through a LiO_2 intermediate and propagates through additional charge exchange at the Li_2O_2 surface. [15] For the reaction/dissolution mechanism, a chemical deposition process involving neutral species would appear to be the mechanism that controls the dimensions of the Li_2O_2 particles; in this case, the increase in surface-to-volume ratio with rate could be attributable to a higher supersaturation of the precipitating neutral species in the liquid phase when the intermediate is produced at higher rate, and/or the surface-diffusion rate of those species on existing Li_2O_2 particles. Alternatively, if the particles form by an electrochemical process, the sizes and shapes of electro-deposits would be expected to change directly in response to the local kinetic overpotential, which propagating particles maximize by increasing their surface-to-volume ratios, which allows higher rates of mass transfer to the electrodeposit by shortening the diffusion lengths of species in the liquid phase. [96] Thus the observation of highly current-dependent morphology presented in Figure 5.5 supports the notions that either particle growth occurs by locally mass-transfer-limited processes (such as nucleation

and diffusion) involving neutral species, or by a locally mass-transfer-limited electrochemical mechanism; either mechanism can rationalize the significant variation in particle morphology as rate increases.

The processes that control discharge-product morphology can be further elucidated by examining Figure 5.6. The shape of the Li_2O_2 formed at 0.1 $mAcm^{-2}$ is similar to the equilibrium Wulff constructions predicted in the literature,[101,102] although all but the 0001 faces appear to be roughened in the SEM images. Note that the surface-to-volume ratios of the particles rise monotonically with rising discharge current, a trend supporting the assertion that non-equilibrium energetics (either owing to supersaturation of a dissolved neutral intermediate or shape-dependent overpotential) is a significant factor that determines product shapes. Either of these mechanisms is consistent with the classical theory of nucleation and growth in electrodeposition.[95,103]

Non-equilibrium surface energetics controls both the shapes and sizes of particles, as reflected by the changes in surface-to-volume ratio with current. Since the particle diameter was found to be relatively constant with respect to rate for the three lowest discharge currents, it appears that in the low-current limit, the growth perpendicular to the flat face is slowest in response to the overpotential, while growth perpendicular to the curved interface is sufficiently fast to reach its equilibrium curvature regardless of the local potential environment. At the highest current, however, the qualitative shape of the Li_2O_2 changes entirely, suggesting that the overpotential is sufficiently large that the curved interface also changes shape.

XRD results serve primarily to ensure that most of the electrochemical and microscopic information can be attributed to the production of Li_2O_2. It remains, however, to consider the origins of the stria evident on particles formed at the lowest two rates (cf. Figure 5.5). XRD spectra show a characteristic crystallite size of about 20 nm that stays constant with respect to discharge rate, consistent with the spacing of the stria.

5.5 Conclusions

There is a growing awareness in the literature that the efficiency of the oxygen-evolution/charging process in Li/O_2 batteries can depend on the structure of the phase that is being decomposed. To understand the high overpotentials typical of recharge, it is important to understand the morphology of the Li_2O_2 phase formed during the preceding discharge, and how that morphology is affected by operating conditions. The present study quantifies these relationships by investigating how the average discharge capacity and product-particle morphology in Li/O_2 cells vary with their discharge rates.

This investigation also clarifies several aspects of electrochemical experimental control. Systematic experiments were performed using porous positive electrodes without particulate additives, coatings, or binders, which were discharged at superficial current densities consistent with the needs for automotive applications. A steep decrease in discharge capacity with discharge rate was observed, consistent with the notion that macroscopic transport processes control capacity in this current regime. When macroscopic transport is limiting, superficial current density likely correlates better with discharge capacity than current densities normalized in other ways.

A statistically significant measured Peukert exponent of 1.6 ± 0.1 also highlights the poor rate performance of state-of-the-art Li/O_2 cells in comparison to other precipitation/dissolution chemistries. The scaling law observed can be rationalized by a hypothesis that a lowering of oxygen penetration depth in the positive electrode (decrease in electrode utilization) with increasing discharge rate is the dominant capacity-limiting factor.

SEM was performed using a novel air-free sample-transfer technique, which prevented samples from being exposed to air before vacuum was drawn in the microscope chamber. Performing dozens of repeated independent first discharges allowed the characteristic dimensions of the Li_2O_2 particles formed during an average first discharge to be established with a high degree of statistical certainty. The Li_2O_2 was found to deposit as disks (toroids) at lower rates, with a constant radius and a variable height; particles formed at lower rates appear to comprise stacked 20 nm layers of fixed diameter. Even at the highest rate, the discharge product phase was observed to have a particulate, rather than a compact, structure. Needle-like shapes with very small characteristic dimensions form at 1 $mAcm^{-2}$. There is a stark difference in product morphology at the highest rate: the surface-to-volume ratio of the needles is an order of magnitude greater than the disks, and the number of needles formed is two orders of magnitude greater than the typical number of disks.

The surface-area-to-volume ratio of discharge-product particles increases dramatically with increasing rate, suggesting that Li_2O_2 forms by a locally mass-transport-limited nucleation and growth mechanism. This is consistent with the notion that the interfacial energy of deposited Li_2O_2 varies with the discharge rate, either in response to the local overpotential environment, or in response to the concentration fields of reactants and/or reactant intermediates.

CHAPTER 6

Conclusions and Future Work

6.1 Future Work

The work described in the previous chapters highlights a few key future research directions. A full comparison of Celgard and Nafion membranes for RFBs will require a more detailed transport model. The impact of the mutli-component transport of oxygen and lithium salt in Li/O_2 batteries could be analyzed further to predict battery performance metrics and optimal electrolyte compositions. Work from the previous sections can provide a certain amount of guidance to these efforts.

6.1.1 Transport in Nafion

The approach in Chapter 3 is attractive, because it outlines a straightforward procedure to get a preliminary handle on the importance of ion-ion interactions in membranes for RFBs. Since the results of this procedure suggest ion-ion interactions are strong in Nafion, it will likely be worth while to experimentally verify the validity of several assumptions made in the procedure. In addition to providing a quantitative figure of merit for membranes for RFBs, these measurements should be done so they are applicable to an actual, operating RFB. This would significantly increase the impact of this work.

One of the core assumptions of the procedure outlined above, implicit in the way conductivity is used to measure mol fraction of acid, is that during interdiffusion, the total concentration on either side of the membrane remains constant. Despite the good fit to the experimental data obtained by the COMSOL model, the model results indicate the total concentration on either side of the membrane changes by as much as 5% over the course of the relaxation. This deviation from the assumption of constant concentration is large enough, it likely affects the values of the transport parameters measured. The internal consistency of the approach outlined above could be checked by performing co-diffusion experiments as well as interdiffusion experiments. In the previous approach salts were

treated as diffusing in their neutral, stoichiometric ratios. This is rigorous for the binary diffusion experiments. For the interdiffusion experiments however, the initially uniform concentration of sulfate likely allows the cations to diffuse freely. Since the cations have smaller atomic radii than the neutral species, this will result in a different relaxation time for the cell. This is one possible reason why the interdiffusion in Nafion occurs so much more quickly than the binary diffusion. Presently these differences are lumped into the ion-ion interaction parameter, D_{HV}, and the parameter for the partition coefficient in the membrane, β . In reality any difference in the diffusivity of H^+ and VO^2+ could result in a drag force on HSO_4^- or SO_4^{-2} and the total concentration on either side of the membrane in the interdiffusion experiment could change over time. The codiffusion experiment could provide an independent measure of D_{HV} and β. If the two agree it will prove that this approach is robust enough to accurately model the multi-component diffusion in membranes for RFBs. If they disagree, then the combination will provide a quantitative basis for comparison of different membranes for RFBs, but accurate modeling of diffusion in the battery will likely require the full characterization of the quaternary or pentanary system.

Measurement of the codiffusion of H_2SO_4 and $VOSO_4$ will require a measure of the concentration of each species independently or a measure of one species and a measure of the total concentration. The time for concentration measurement will also need to be fast compared to the time it takes the concentration in the cell to change. Measuring the UV-Vis absorbance and the conductivity of the solution could accomplish this with commonly available laboratory equipment. $VOSO_4$ is blue where H_2SO_4 is mostly transparent, so UV-Vis absorbance can be used to measure $VOSO_4$ concentration independent of H_2SO_4. Conductivity can be used to measure the total concentration. Since the conductivity is a monotonic increasing function of total concentration at all mol fractions, a given $VOSO_4$ concentration will draw a line on the conductivity vs. mol fraction acid curve, so the mol fraction can be measured by the conductivity. The mol fraction and $VOSO_4$ concentration uniquely determine the composition of the solution. Simultaneous measurement of the UV-Vis absorbance and conductivity can be taken in real time as long as a small fraction of the total solution can be circulated through the UV-Vis spectrometer and returned to the dialysis cell in a few tens of seconds. This would give a negligible time lag over the course of the 10 hr experiment.

Successful implementation of the above procedures would also open up a new avenue for measuring transport properties in Nafion. The presence of some conductive species diffusing at short time complicated the analysis of the $VOSO_4$ in Nafion transient concentration curve. To get around this obstacle the codiffusion experiment could be used in place of the $VOSO_4$ binary experiment. Calculating binary diffusion coefficients and par-

tition coefficients in this way would be very nonlinear, and possibly prone to error. The error of the procedure could be determined using results from the Celgard experiments as a benchmark. More quantitative data will allow for a more detailed comparison between the Celgard and Nafion.

6.1.2 Oxygen Transport in Li/O_2 Electrolytes

The analysis in chapter 4 provided a means for estimating transport parameters for Li/O_2 electrolytic solutions. Corrosion processes in the cells caused significant variability in the measured effective oxygen diffusion coefficient, and error in the measurement of the electro-osmotic coefficient however. This was largely due to the use of metallic lithium as one of the electrodes in these experiments. These experiments could be refined by selecting a more stable electrode combination. For example lithium ferrous phosphate electrodes give a very stable potential vs the lithium electrode and have been used in fundamental electrochemical characterization of Li/O_2 cells.[17] These could be used in place of the lithium electrodes used here. The stability of the electrodes themselves will be vital, because the value of the electro-osmotic coefficient is predicted to be quite small. Recall that in Chapter 4 the electro-osmotic coefficient, Ξ is related to the six microscopic transport coefficients through

$$\Xi = \frac{c_{\mathrm{o}}\mathscr{D}_{\mathrm{o}0}\left(t^0_{+\mathrm{o}} - t^{\mathrm{o}}_{+0}\right)}{c_0\mathscr{D}_{\mathrm{eo}} + \nu_{\mathrm{e}}c_{\mathrm{e}}\mathscr{D}_{\mathrm{o}0} + c_{\mathrm{o}}\mathscr{D}_{\mathrm{e}0}}. \tag{6.1}$$

where good estimates have been given for every number except the transference number t^{o}_{+0}. Inserting the available estimates shows how Ξ is expected to scale with t^{o}_{+0}

$$\Xi = 0.005\left(0.4 - t^{\mathrm{o}}_{+0}\right). \tag{6.2}$$

This means that for the electro-osmotic coefficient to be negative, the value of t^{o}_{+0} must be greater than 0.4. Recall also that the ionic conductivity is given by

$$\frac{1}{\kappa} = \frac{1}{\kappa_{\mathrm{o}}} + \frac{\nu_{\mathrm{e}}c_{\mathrm{o}}RT}{F^2z_+^2\nu_+^2c_{\mathrm{e}}c_{\mathrm{T}}\mathscr{D}_{\mathrm{eo}}}\times \left[t^{\mathrm{o}}_{+0}\left(1 - t^{\mathrm{o}}_{+0}\right) + \frac{c_0\mathscr{D}_{\mathrm{e}0}\left(t^0_{+\mathrm{o}} - t^{\mathrm{o}}_{+0}\right)^2}{c_0\mathscr{D}_{\mathrm{eo}} + \nu_{\mathrm{e}}c_{\mathrm{e}}\mathscr{D}_{\mathrm{o}0} + c_{\mathrm{o}}\mathscr{D}_{\mathrm{e}0}}\right]. \tag{6.3}$$

Inserting the estimates for the transport values as before, it can be shown that the expression for the conductivity of the oxygen saturated solution falls for values of $t^{o}_{+0} < 1.7$, then rises when $t^{o}_{+0} > 1.7$, and ultimately diverges for $t^{o}_{+0} > 5.4$ (after diverging the expression remains negative as t^{o}_{+0} increases toward infinity). So, given estimates of the other transport parameters, the expressions of Ξ and κ give a reasonable range for possible values of t^{o}_{+0}: $0.4 < t^{o}_{+0} < 5.4$. This in turn gives a range of possible values for the electro-osmotic coefficient $0 > \Xi > -.025$ and by extension, the deviation from the equilibrium open circuit cell potential $0 < \Delta\Phi - U^{\theta} < 0.001$V. Measuring such a small change in cell potential will require very stable electrodes. Increasing the partial pressure of oxygen in the head space of the cell would also increase the potential difference, making it easier to measure.

The observations in chapter 4 highlight an interesting optimization problem as well. Conductivity of an electrolyte generally increases with increasing concentration. Typically batteries use a high electrolyte concentration to achieve high conductivity and minimize ohmic losses. The values of the transport parameters suggest that the diffusion coefficient of oxygen will fall steeply with increasing electrolyte concentration, however. Therefore, if cell capacity is desired, a very small concentration of the electrolyte should be used. A continuum scale model of a Li/O_2 battery could be used to explore this tradeoff and suggest an electrolyte composition that would result in optimal energy available from the cell.

6.2 Conclusions

The previous chapters have shown that multi-component diffusion will be a vitally important factor to understand when designing next-generation batteries. The study of transport in separators for redox flow batteries, showed that diffusional interactions apparent in Nafion membranes will require detailed transport models to fully understand. Characterization of the rate performance in Li/O_2 batteries showed that oxygen diffusion was limiting the discharge capacity available at moderate rates. More detailed measurements of the transport of oxygen in electrolytes for Li/O_2 batteries showed that the oxygen diffusion coefficient fell precipitously with increasing lithium salt concentration in the electrolytic solution.

Transport of active species and supporting electrolyte were studied in Celgard and Nafion. Two binary diffusion experiments and one interdiffusion experiment in a batch dialysis cell gave measures of two partition coefficients and three diffusion coefficients, describing the transport of vanadyl sulfate and sulfuric acid in Celgard separators. The ten times higher diffusion coefficient of sulfuric acid compared to vanadyl sulfate indicated Celgard should have reasonably good selectivity. Interdiffusion experiments in Nafion and

Celgard reached completion in nearly the same amount of time, 15 and 10 hours respectively, showing that the diffusivity of sulfuric acid in the presence of vanadyl sulfate was comparable in each membrane. This means the Celgard should have a conductivity comparable to Nafion as well. These results highlight the usefulness of porous separators for RFBs.

The procedure outlined by Monroe *et al.*[58] for modeling transport of four species (two with charge and two neutral) provided relations between transport coefficients and measurable macroscopic quantities. Relations for several macroscopic quantities simplified to their oxygen-free values in the limit of zero oxygen concentration, allowing values for three of the six parameters to be taken from pre-existing literature. A procedure for using the OCP of Li/O_2 cells, and the ionic conductivity to calculate the remaining transport parameters was proposed. Relaxation experiments showed that the cell potential took several hours to re-equilibrate after a step change in the oxygen partial pressure in the head space of the cell. It was also observed that the sign of the deviation from equilibrium cell potential was directly related to the direction of the imposed oxygen concentration gradient. Ionic conductivity measurements of the solution equilibrated with argon and equilibrated with 0.5 bar oxygen provided an upper bound for the electro-osmotic coefficient. Comparison of the experimental results along with values estimated from literature showed the electro-osmotic coefficient negligibly impacts the OCP, however the effective oxygen diffusivity can be twenty to one hundred times smaller than what is typically measured in pure solvents. This validates the common approach to modeling transport in the cell using Fick's law on the oxygen and concentrated solution theory for the electrolyte, however, it shows that the effective oxygen diffusivity in this approach will be much smaller than the value of the oxygen diffusivity through pure solvent.

In the study of Li/O_2 battery rate performance, systematic experiments were performed using porous positive electrodes without particulate additives, coatings, or binders, which were discharged at superficial current densities consistent with the needs for automotive applications. A steep decrease in discharge capacity with discharge rate was observed, consistent with the notion that macroscopic transport processes control capacity in this current regime. When macroscopic transport is limiting, superficial current density likely correlates better with discharge capacity than current densities normalized in other ways. A statistically significant measured Peukert exponent of 1.6 ± 0.1 also highlights the poor rate performance of state-of-the-art Li/O_2 cells in comparison to other precipitation/dissolution chemistries. The scaling law observed can be rationalized by a hypothesis that a lowering of oxygen penetration depth in the positive electrode (decrease in electrode utilization) with increasing discharge rate is the dominant capacity-limiting factor.

BIBLIOGRAPHY

[1] Jonathon Duay, Eleanor Gillette, Junkai Hu, and Sang Bok Lee. Controlled electrochemical deposition and transformation of hetero-nanoarchitectured electrodes for energy storage. *Physical Chemistry Chemical Physics*, 15(21):7976–7993, 2013.

[2] Jim Eyer and Garth Corey. Energy storage for the electricity grid: Benefits and market potential assessment guide. *Sandia National Laboratories*, 2010.

[3] Xiaoliang Wei, Bin Li, and Wei Wang. Porous polymeric composite separators for redox flow batteries. *Polymer Reviews*, 55(2):247–272, 2015.

[4] U.S. Energy Information Administration. Monthly energy review.

[5] C. Monroe and J. Newman. The impact of elastic deformation on deposition kinetics at lithium/polymer interfaces. *Journal of the Electrochemical Society*, 152(2):A396–A404, 2005.

[6] T. Ogasawara, A. Debart, M. Holzapfel, P. Novak, and P. G. Bruce. Rechargeable li2o2 electrode for lithium batteries. *Journal of the American Chemical Society*, 128(4):1390–1393, 2006.

[7] A. Debart, J. Bao, G. Armstrong, and P. G. Bruce. An o-2 cathode for rechargeable lithium batteries: The effect of a catalyst. *Journal of Power Sources*, 174(2):1177–1182, 2007.

[8] S. A. Freunberger, Y. H. Chen, Z. Q. Peng, J. M. Griffin, L. J. Hardwick, F. Barde, P. Novak, and P. G. Bruce. Reactions in the rechargeable lithium-o-2 battery with alkyl carbonate electrolytes. *Journal of the American Chemical Society*, 133(20):8040–8047, 2011.

[9] J. Read, K. Mutolo, M. Ervin, W. Behl, J. Wolfenstine, A. Driedger, and D. Foster. Oxygen transport properties of organic electrolytes and performance of lithium/oxygen battery. *Journal of the Electrochemical Society*, 150(10):A1351–A1356, 2003.

[10] B. D. McCloskey, D. S. Bethune, R. M. Shelby, G. Girishkumar, and A. C. Luntz. Solvents' critical role in nonaqueous lithium-oxygen battery electrochemistry. *Journal of Physical Chemistry Letters*, 2(10):1161–1166, 2011.

[11] Yi-Chun Lu, David G Kwabi, Koffi PC Yao, Jonathon R Harding, Jigang Zhou, Lucia Zuin, and Yang Shao-Horn. The discharge rate capability of rechargeable li–o 2 batteries. *Energy & Environmental Science*, 4(8):2999–3007, 2011.

[12] G. M. Veith, J. Nanda, L. H. Delmau, and N. J. Dudney. Influence of lithium salts on the discharge chemistry of li-air cells. *Journal of Physical Chemistry Letters*, 3(10):1242–1247, 2012.

[13] Muhammed M Ottakam Thotiyl, Stefan A Freunberger, Zhangquan Peng, and Peter G Bruce. The carbon electrode in nonaqueous li–o2 cells. *Journal of the American Chemical Society*, 135(1):494–500, 2012.

[14] Stefano Meini, Michele Piana, Nikolaos Tsiouvaras, Arnd Garsuch, and Hubert A Gasteiger. The effect of water on the discharge capacity of a non-catalyzed carbon cathode for li-o2 batteries. *Electrochemical and Solid-State Letters*, 15(4):A45–A48, 2012.

[15] Z. Q. Peng, S. A. Freunberger, L. J. Hardwick, Y. H. Chen, V. Giordani, F. Barde, P. Novak, D. Graham, J. M. Tarascon, and P. G. Bruce. Oxygen reactions in a non-aqueous li+ electrolyte. *Angewandte Chemie-International Edition*, 50(28):6351–6355, 2011.

[16] Junbing Yang, Dengyun Zhai, Hsien-Hau Wang, Kah Chun Lau, John A. Schlueter, Peng Du, Deborah J. Myers, Yang-Kook Sun, Larry A. Curtiss, and Khalil Amine. Evidence for lithium superoxide-like species in the discharge product of a li-o2 battery. *Phys. Chem. Chem. Phys.*, 15:3764–3771, 2013.

[17] Lee Johnson, Chunmei Li, Zheng Liu, Yuhui Chen, Stefan A Freunberger, Praveen C Ashok, Bavishna B Praveen, Kishan Dholakia, Jean-Marie Tarascon, and Peter G Bruce. The role of lio2 solubility in o2 reduction in aprotic solvents and its consequences for li–o2 batteries. *Nature chemistry*, 6(12):1091–1099, 2014.

[18] Z. Q. Peng, S. A. Freunberger, Y. H. Chen, and P. G. Bruce. A reversible and higher-rate li-o(2) battery. *Science*, 337(6094):563–566, 2012.

[19] Muhammed M Ottakam Thotiyl, Stefan A Freunberger, Zhangquan Peng, Yuhui Chen, Zheng Liu, and Peter G Bruce. A stable cathode for the aprotic li–o2 battery. *Nature materials*, 12(11):1050–1056, 2013.

[20] Tao Liu, Michal Leskes, Wanjing Yu, Amy J Moore, Lina Zhou, Paul M Bayley, Gunwoo Kim, and Clare P Grey. Cycling li-o2 batteries via lioh formation and decomposition. *Science*, 350(6260):530–533, 2015.

[21] Lucas D Griffith, Alice ES Sleightholme, John F Mansfield, Donald J Siegel, and Charles W Monroe. Correlating li/o2 cell capacity and product morphology with discharge current. *ACS applied materials & interfaces*, 7(14):7670–7678, 2015.

[22] John Newman and Karen E Thomas-Alyea. *Electrochemical systems*. John Wiley & Sons, 2012.

[23] Raymond M Fuoss and Lars Onsager. Conductance of strong electrolytes at finite dilutions. *Proceedings of the National Academy of Sciences*, 41(5):274–283, 1955.

[24] M. Skyllas-Kazacos, M. H. Chakrabarti, S. A. Hajimolana, F. S. Mjalli, and M. Saleem. Progress in flow battery research and development. *Journal of the Electrochemical Society*, 158(8):R55–R79, 2011.

[25] James A Mellentine, Walter J Culver, and Robert F Savinell. Simulation and optimization of a flow battery in an area regulation application. *Journal of Applied Electrochemistry*, 41(10):1167–1174, 2011.

[26] Adam Z Weber, Matthew M Mench, Jeremy P Meyers, Philip N Ross, Jeffrey T Gostick, and Qinghua Liu. Redox flow batteries: a review. *Journal of Applied Electrochemistry*, 41(10):1137–1164, 2011.

[27] C Ponce De Leon, A Frias-Ferrer, José González-García, DA Szánto, and Frank C Walsh. Redox flow cells for energy conversion. *Journal of Power Sources*, 160(1):716–732, 2006.

[28] Maria Skyllas-Kazacos, George Kazacos, Grace Poon, and Hugh Verseema. Recent advances with unsw vanadium-based redox flow batteries. *International Journal of Energy Research*, 34(2):182–189, 2010.

[29] Soowhan Kim, Jingling Yan, Birgit Schwenzer, Jianlu Zhang, Liyu Li, Jun Liu, Zhenguo Gary Yang, and Michael A Hickner. Cycling performance and efficiency of sulfonated poly (sulfone) membranes in vanadium redox flow batteries. *Electrochemistry Communications*, 12(11):1650–1653, 2010.

[30] Dongyang Chen, Soowhan Kim, Liyu Li, Gary Yang, and Michael A Hickner. Stable fluorinated sulfonated poly (arylene ether) membranes for vanadium redox flow batteries. *RSC Advances*, 2(21):8087–8094, 2012.

[31] Dongyang Chen, Soowhan Kim, Vincent Sprenkle, and Michael A Hickner. Composite blend polymer membranes with increased proton selectivity and lifetime for vanadium redox flow batteries. *Journal of Power Sources*, 231:301–306, 2013.

[32] QH Liu, GM Grim, AB Papandrew, A Turhan, Thomas A Zawodzinski, and Matthew M Mench. High performance vanadium redox flow batteries with optimized electrode configuration and membrane selection. *Journal of The Electrochemical Society*, 159(8):A1246–A1252, 2012.

[33] SC Chieng, M Kazacos, and M Skyllas-Kazacos. Preparation and evaluation of composite membrane for vanadium redox battery applications. *Journal of power sources*, 39(1):11–19, 1992.

[34] Chenxi Sun, Jian Chen, Huamin Zhang, Xi Han, and Qingtao Luo. Investigations on transfer of water and vanadium ions across nafion membrane in an operating vanadium redox flow battery. *Journal of Power Sources*, 195(3):890–897, 2010.

[35] Q. T. Luo, H. M. Zhang, J. Chen, P. Qian, and Y. F. Zhai. Modification of nafion membrane using interfacial polymerization for vanadium redox flow battery applications. *Journal of Membrane Science*, 311(1-2):98–103, 2008.

[36] Xuanli Luo, Zhengzhong Lu, Jingyu Xi, Zenghua Wu, Wentao Zhu, Liquan Chen, and Xinping Qiu. Influences of permeation of vanadium ions through pvdf-g-pssa membranes on performances of vanadium redox flow batteries. *The Journal of Physical Chemistry B*, 109(43):20310–20314, 2005.

[37] Theresa Sukkar and Maria Skyllas-Kazacos. Water transfer behaviour across cation exchange membranes in the vanadium redox battery. *Journal of Membrane Science*, 222(1):235–247, 2003.

[38] DS Aaron, Q Liu, Z Tang, GM Grim, AB Papandrew, A Turhan, TA Zawodzinski, and MM Mench. Dramatic performance gains in vanadium redox flow batteries through modified cell architecture. *Journal of Power sources*, 206:450–453, 2012.

[39] E. Wiedemann, A. Heintz, and R. N. Lichtenthaler. Sorption isotherms of vanadium with h3o+ ions in cation exchange membranes. *Journal of Membrane Science*, 141(2):207–213, 1998.

[40] Richard P. Wendt. Studies of isothermal diffusion at 25 in the system water-sodium sulfate-sulfuric acid and tests of the onsager relation1. *The Journal of Physical Chemistry*, 66(7):1279–1288, 1962.

[41] A. Heintz, E. Wiedemann, and J. Ziegler. Ion exchange diffusion in electromembranes and its description using the maxwell-stefan formalism. *Journal of Membrane Science*, 137(1-2):121–132, 1997.

[42] Barnes C. Diffusion through a membrane. *Physics*, 5(1):5, 1934.

[43] Lars Onsager. Theories and problems of liquid diffusion. *Annals of the New York Academy of Sciences*, 46(5):241–265, 1945.

[44] EN Lightfoot, EL Cussler, and RL Rettig. Applicability of the stefan-maxwell equations to multicomponent diffusion in liquids. *AIChE Journal*, 8(5):708–710, 1962.

[45] Eugene Helfand. On inversion of the linear laws of irreversible thermodynamics. *The Journal of Chemical Physics*, 33(2):319–322, 1960.

[46] K. S. Spiegler. Transport processes in ionic membranes. *Transactions of the Faraday Society*, 54(9):1408–1428, 1958.

[47] Charles W Monroe and John Newman. Onsager reciprocal relations for stefan-maxwell diffusion. *Industrial & engineering chemistry research*, 45(15):5361–5367, 2006.

[48] Charles W Monroe and John Newman. Onsager's shortcut to proper forces and fluxes. *Chemical Engineering Science*, 64(22):4804–4809, 2009.

[49] Y. C. Lu, H. A. Gasteiger, M. C. Parent, V. Chiloyan, and Y. Shao-Horn. The influence of catalysts on discharge and charge voltages of rechargeable li-oxygen batteries. *Electrochemical and Solid State Letters*, 13(6):A69–A72, 2010.

[50] B. D. Adams, C. Radtke, R. Black, M. L. Trudeau, K. Zaghib, and L. F. Nazar. Current density dependence of peroxide formation in the li-o-2 battery and its effect on charge. *Energy & Environmental Science*, 6(6):1772–1778, 2013.

[51] Hugh Geaney, John O'Connell, Justin D Holmes, and Colm O'Dwyer. On the use of gas diffusion layers as current collectors in li-o2 battery cathodes. *Journal of The Electrochemical Society*, 161(14):A1964–A1968, 2014.

[52] P. Albertus, G. Girishkumar, B. McCloskey, R. S. Sanchez-Carrera, B. Kozinsky, J. Christensen, and A. C. Luntz. Identifying capacity limitations in the li/oxygen battery using experiments and modeling. *Journal of the Electrochemical Society*, 158(3):A343–A351, 2011.

[53] Petru Andrei, Jim P Zheng, Mary Hendrickson, and EJ Plichta. Modeling of li-air batteries with dual electrolyte. *Journal of The Electrochemical Society*, 159(6):A770–A780, 2012.

[54] Birger Horstmann, Timo Danner, and Wolfgang G Bessler. Precipitation in aqueous lithium–oxygen batteries: a model-based analysis. *Energy & Environmental Science*, 6(4):1299–1314, 2013.

[55] Ukrit Sahapatsombut, Hua Cheng, and Keith Scott. Modelling the micro–macro homogeneous cycling behaviour of a lithium–air battery. *Journal of Power Sources*, 227:243–253, 2013.

[56] Kisoo Yoo, Soumik Banerjee, and Prashanta Dutta. Modeling of volume change phenomena in a li–air battery. *Journal of Power Sources*, 258:340–350, 2014.

[57] D.A. MacInnes. *The Principles of Electrochemistry*. Dover Publications, Inc., New York, New York, 2 edition, 1961.

[58] Charles W Monroe and Charles Delacourt. Continuum transport laws for locally non-neutral concentrated electrolytes. *Electrochimica Acta*, 114:649–657, 2013.

[59] Thomas F Fuller and John Newman. Experimental determination of the transport number of water in nafion 117 membrane. *Journal of The Electrochemical Society*, 139(5):1332–1337, 1992.

[60] Edward Armand Guggenheim. Thermodynamics-an advanced treatment for chemists and physicists. *Amsterdam, North-Holland, 1985, 414 p.*, 1985.

[61] R.A. Robinson and R.H. Stokes. *Electrolyte Solutions*. Butterworth & Co., second revised edition, 1959.

[62] J. Read. Ether-based electrolytes for the lithium/oxygen organic electrolyte battery. *Journal of the Electrochemical Society*, 153(1):A96–A100, 2006.

[63] Dany Brouillette, Gérald Perron, and Jacques E Desnoyers. Apparent molar volume, heat capacity, and conductance of lithium bis (trifluoromethylsulfone) imide in glymes and other aprotic solvents. *Journal of solution chemistry*, 27(2):151–182, 1998.

[64] Pascal Hartmann, Daniel Grübl, Heino Sommer, Jürgen Janek, Wolfgang G. Bessler, and Philipp Adelhelm. Pressure dynamics in metal–oxygen (metal–air) batteries: A case study on sodium superoxide cells. *The Journal of Physical Chemistry C*, 118(3):1461–1471, 2014.

[65] Frederick T. Wagner, Balasubramanian Lakshmanan, and Mark F. Mathias. Electrochemistry and the future of the automobile. *The Journal of Physical Chemistry Letters*, 1(14):2204–2219, 2010.

[66] J. Christensen, P. Albertus, R. S. Sanchez-Carrera, T. Lohmann, B. Kozinsky, R. Liedtke, J. Ahmed, and A. Kojic. A critical review of li/air batteries. *Journal of the Electrochemical Society*, 159(2):R1–R30, 2012.

[67] G. Girishkumar, B. McCloskey, A. C. Luntz, S. Swanson, and W. Wilcke. Lithium - air battery: Promise and challenges. *Journal of Physical Chemistry Letters*, 1(14):2193–2203, 2010.

[68] Y. C. Lu, B. M. Gallant, D. G. Kwabi, J. R. Harding, R. R. Mitchell, M. S. Whittingham, and Y. Shao-Horn. Lithium-oxygen batteries: bridging mechanistic understanding and battery performance. *Energy & Environmental Science*, 6(3):750–768, 2013.

[69] K. M. Abraham and Z. Jiang. A polymer electrolyte-based rechargeable lithium/oxygen battery. *Journal of the Electrochemical Society*, 143(1):1–5, 1996.

[70] B. M. Gallant, D. G. Kwabi, R. R. Mitchell, J. G. Zhou, C. V. Thompson, and Y. Shao-Horn. Influence of li2o2 morphology on oxygen reduction and evolution kinetics in li-o-2 batteries. *Energy & Environmental Science*, 6(8):2518–2528, 2013.

[71] M. Leskes, A. J. Moore, G. R. Goward, and C. P. Grey. Monitoring the electrochemical processes in the lithium-air battery by solid state nmr spectroscopy. *Journal of Physical Chemistry C*, 117(51):26929–26939, 2013.

[72] Robert R. Mitchell, Betar M. Gallant, Carl V. Thompson, and Yang Shao-Horn. All-carbon-nanofiber electrodes for high-energy rechargeable li-o2 batteries. *Energy & Environmental Science*, 4(8):2952–2958, 2011.

[73] D. Xu, Z. L. Wang, J. J. Xu, L. L. Zhang, and X. B. Zhang. Novel dmso-based electrolyte for high performance rechargeable li-o-2 batteries. *Chemical Communications*, 48(55):6948–6950, 2012.

[74] J. J. Xu, Z. L. Wang, D. Xu, L. L. Zhang, and X. B. Zhang. Tailoring deposition and morphology of discharge products towards high-rate and long-life lithium-oxygen batteries. *Nature Communications*, 4, 2013.

[75] Chun Xia, Michael Waletzko, Limei Chen, Klaus Peppler, Peter J Klar, and Jürgen Janek. Evolution of li2o2 growth and its effect on kinetics of li–o2 batteries. *ACS Appl. Mater. Interfaces*, 6(15):12083–12092, 2014.

[76] Maxwell D. Radin and Donald J. Siegel. Charge transport in lithium peroxide: relevance for rechargeable metal-air batteries. *Energy & Environmental Science*, 6(8):2370–2379, 2013.

[77] Feng Tian, Maxwell D. Radin, and Donald J. Siegel. Enhanced charge transport in amorphous li2o2. *Chemistry of Materials*, 26(9):2952–2959, 2014.

[78] Maxwell D. Radin, Jill F. Rodriguez, Feng Tian, and Donald J. Siegel. Lithium peroxide surfaces are metallic, while lithium oxide surfaces are not. *Journal of the American Chemical Society*, 134(2):1093–1103, 2011.

[79] W. T. Geng, B. L. He, and T. Ohno. Grain boundary induced conductivity in li2o2. *The Journal of Physical Chemistry C*, 117(48):25222–25228, 2013.

[80] Eda Yilmaz, Chihiro Yogi, Keisuke Yamanaka, Toshiaki Ohta, and Hye Ryung Byon. Promoting formation of noncrystalline li_2o_2 in the li–o_2 battery with ruo_2 nanoparticles. *Nano Letters*, 13(10):4679–4684, 2013.

[81] J. Adams, M. Karulkar, and V. Anandan. Evaluation and electrochemical analyses of cathodes for lithium-air batteries. *Journal of Power Sources*, 239:132–143, 2013.

[82] United States Advanced Battery Consortium. Usabc goals for advanced batteries for evs.

[83] Hun-Gi Jung, Jusef Hassoun, Jin-Bum Park, Yang-Kook Sun, and Bruno Scrosati. An improved high-performance lithium–air battery. *Nature Chemistry*, 4(7):579–585, 2012.

[84] Peukert. Über die abhängigkeit der kapazität von der entladestromstärke bei bleiakkumulatoren. *Elektrotechnische Zeitschrift, Asgabe A*, 18:20–21, 1897.

[85] Hun-Gi Jung, Hee-Soo Kim, Jin-Bum Park, In-Hwan Oh, Jusef Hassoun, Chong Seung Yoon, Bruno Scrosati, and Yang-Kook Sun. A transmission electron microscopy study of the electrochemical process of lithiumäìoxygen cells. *Nano Letters*, 12(8):4333–4335, 2012.

[86] V. Viswanathan, J. K. Nørskov, A. Speidel, R. Scheffler, S. Gowda, and A. C. Luntz. Li–o2 kinetic overpotentials: Tafel plots from experiment and first-principles theory. *J. Phys. Chem. Lett.*, 4(4):556–560, 2013.

[87] Y. C. Lu, H. A. Gasteiger, and Y. Shao-Horn. Catalytic activity trends of oxygen reduction reaction for nonaqueous li-air batteries. *Journal of the American Chemical Society*, 133(47):19048–19051, 2011.

[88] D. Baert and A. Vervaet. Lead-acid battery model for the derivation of peukert's law. *Electrochimica Acta*, 44(20):3491 – 3504, 1999.

[89] M.I. Gillibrand and G.R. Lomax. The discharge characteristics of lead-acid battery plates. *Electrochimica Acta*, 8(9):693 – 702, 1963.

[90] N. Omar, B. Verbrugge, G. Mulder, P. Van den Bossche, Joeri Van Mierlo, M. Daowd, M. Dhaens, and S. Pauwels. Evaluation of performance characteristics of various lithium-ion batteries for use in bev application. *Vehicle Power and Propulsion Conference (VPPC), 2010 IEEE*, pages 1–6, 2010.

[91] Matthieu Dubarry, Cyril Truchot, Mikaël Cugnet, Bor Yann Liaw, Kevin Gering, Sergiy Sazhin, David Jamison, and Christopher Michelbacher. Evaluation of commercial lithium-ion cells based on composite positive electrode for plug-in hybrid electric vehicle applications. part i: Initial characterizations. *Journal of Power Sources*, 196(23):10328 – 10335, 2011.

[92] William M Haynes. *CRC handbook of chemistry and physics*. CRC press, 2014.

[93] B. D. McCloskey, R. Scheffler, A. Speidel, D. S. Bethune, R. M. Shelby, and A. C. Luntz. On the efficacy of electrocatalysis in nonaqueous li-o-2 batteries. *Journal of the American Chemical Society*, 133(45):18038–18041, 2011.

[94] B. D. McCloskey, R. Scheffler, A. Speidel, G. Girishkumar, and A. C. Luntz. On the mechanism of nonaqueous li-o-2 electrochemistry on c and its kinetic overpotentials: Some implications for li-air batteries. *Journal of Physical Chemistry C*, 116(45):23897–23905, 2012.

[95] J. W. Diggle, A. R. Despic, and J. O'M. Bockris. The mechanism of the dendritic electrocrystallization of zinc. *Journal of the Electrochemical Society*, 116(11):1503–1514, 1969.

[96] Charles Monroe and John Newman. The effect of interfacial deformation on electrodeposition kinetics. *Journal of The Electrochemical Society*, 151(6):A880–A886, 2004.

[97] E Joseph Nemanick and Ryan P Hickey. The effects of o¡ sub¿ 2¡/sub¿ pressure on li–o¡ sub¿ 2¡/sub¿ secondary battery discharge capacity and rate capability. *Journal of Power Sources*, 252:248–251, 2014.

[98] V. Viswanathan, K. S. Thygesen, J. S. Hummelshoj, J. K. Norskov, G. Girishkumar, B. D. McCloskey, and A. C. Luntz. Electrical conductivity in li2o2 and its role in determining capacity limitations in non-aqueous li-o-2 batteries. *Journal of Chemical Physics*, 135(21), 2011.

[99] C. O. Laoire, S. Mukerjee, K. M. Abraham, E. J. Plichta, and M. A. Hendrickson. Influence of nonaqueous solvents on the electrochemistry of oxygen in the rechargeable lithium-air battery. *Journal of Physical Chemistry C*, 114(19):9178–9186, 2010.

[100] W. Xu, K. Xu, V. V. Viswanathan, S. A. Towne, J. S. Hardy, J. Xiao, D. H. Hu, D. Y. Wang, and J. G. Zhang. Reaction mechanisms for the limited reversibility of li-o-2 chemistry in organic carbonate electrolytes. *Journal of Power Sources*, 196(22):9631–9639, 2011.

[101] Yifei Mo, Shyue Ping Ong, and Gerbrand Ceder. First-principles study of the oxygen evolution reaction of lithium peroxide in the lithium-air battery. *Physical Review B*, 84(20):205446, 2011. PRB.

[102] Maxwell D Radin, Feng Tian, and Donald J Siegel. Electronic structure of li2o2 0001 surfaces. *Journal of Materials Science*, 47(21):7564–7570, 2012.

[103] J. L. Barton and J. O. Bockris. Electrolytic growth of dendrites from ionic solutions. *Proceedings of the Royal Society of London Series a-Mathematical and Physical Sciences*, 268(1335):485, 1962.